1986

X-ray diffraction studies of bismuth-doped lead dioxide electrodes, of the radiation-damaged benzene chromium tricarbonyl crystal structure, and of selected organometallic compounds

Sangsoo Kim
Iowa State University

INFORMATION TO USERS

While the most advanced technology has been used to photograph and reproduce this manuscript, the quality of the reproduction is heavily dependent upon the quality of the material submitted. For example:

- Manuscript pages may have indistinct print. In such cases, the best available copy has been filmed.

- Manuscripts may not always be complete. In such cases, a note will indicate that it is not possible to obtain missing pages.

- Copyrighted material may have been removed from the manuscript. In such cases, a note will indicate the deletion.

Oversize materials (e.g., maps, drawings, and charts) are photographed by sectioning the original, beginning at the upper left-hand corner and continuing from left to right in equal sections with small overlaps. Each oversize page is also filmed as one exposure and is available, for an additional charge, as a standard 35mm slide or as a 17"x 23" black and white photographic print.

Most photographs reproduce acceptably on positive microfilm or microfiche but lack the clarity on xerographic copies made from the microfilm. For an additional charge, 35mm slides of 6"x 9" black and white photographic prints are available for any photographs or illustrations that cannot be reproduced satisfactorily by xerography.

Kim, Sangsoo

X-RAY DIFFRACTION STUDIES OF BISMUTH-DOPED LEAD DIOXIDE ELECTRODES, OF THE RADIATION-DAMAGED BENZENE CHROMIUM TRICARBONYL CRYSTAL STRUCTURE, AND OF SELECTED ORGANOMETALLIC COMPOUNDS

Iowa State University Ph.D. 1986

X-ray diffraction studies of bismuth-doped lead dioxide electrodes, of the radiation-damaged benzene chromium tricarbonyl crystal structure, and of selected organometallic compounds

by

Sangsoo Kim

A Dissertation Submitted to the
Graduate Faculty in Partial Fulfillment of the
Requirements for the Degree of
DOCTOR OF PHILOSOPHY

Department: Chemistry
Major: Physical Chemistry

Approved:

Signature was redacted for privacy.

In Charge of Major Work

Signature was redacted for privacy.

For the Major Department

Signature was redacted for privacy.

For the Graduate College

Iowa State University
Ames, Iowa

1986

TABLE OF CONTENTS

	Page
DEDICATION	iv
PREFACE	1
SECTION I	3
AN X-RAY POWDER DIFFRACTION STUDY OF LEAD DIOXIDE ELECTRODES DOPED WITH BISMUTH, ARSENIC, OR THALIUM	
INTRODUCTION	4
EXPERIMENTAL SECTION	19
RESULTS AND DISCUSSION	35
REFERENCES	60
SECTION II	62
A STUDY OF X-RAY RADIATION DAMAGE ON A SINGLE CRYSTAL OF BENZENE CHROMIUM TRICARBONYL	
INTRODUCTION	63
EXPERIMENTAL SECTION	65
RESULTS	70
DISCUSSION	83
REFERENCES	85

SECTION III 86

CRYSTAL AND MOLECULAR STRUCTURES OF SELECTED ORGANOMETALLIC COMPOUNDS CONTAINING SULFUR ATOM

INTRODUCTION 87

EXPERIMENTAL SECTION 90

RESULTS AND DISCUSSION 106

REFERENCES 130

SECTION IV 134

EXPLORATION OF PATTERSON SUPERPOSITION TO TWO INORGANIC CLUSTER COMPOUNDS WITH UNUSUALLY HIGH PSEUDO-SYMMETRY

INTRODUCTION 135

EXPERIMENTAL SECTION 138

RESULTS 142

DISCUSSION 160

REFERENCES 168

SUMMARY 169

ACKNOWLEDGMENTS 172

DEDICATION

To my mother and father

PREFACE

X-ray crystallography has extremely useful applications in many branches of science such as chemistry, physics, biology, metallogy, geology, etc. Its main chemical application is in elucidating crystal structures at the atomic level. Careful analyses of X-ray diffraction patterns lead to fairly detailed information about the bonding geometry and electron density.

In this thesis, various topics of X-ray crystallography are discussed. They include molecular structure determinations, a study of the phase problem, an application of X-ray powder diffraction, and X-ray radiation damage study. Since they cover wide range of topics and each is self-contained, different topics are treated in different sections of this thesis.

The first section deals with X-ray powder diffraction study of Bi-doped β-PbO_2 electrode materials prepared by Dr. Johnson's group. Emphasis is on data collection techniques, a diffraction pattern fitting procedure using the Rietveld method, and structure-property relationships. In the second section, the effect of X-ray radiation damage, especially on a single crystal of benzene chromium tricarbonyl, is discussed with emphases on the variation of the structural parameters. The third section is devoted on a brief discussion of structures of closely related organometallic

compounds, namely $[HB(pz)_3](CO)_2W[\eta^2\text{-}CH(SMe)]\cdot CF_3SO_3$, $[HB(pz)_3](CO)_2W[\eta^2\text{-}CH(SMe)(PPh_2)]$, $[HB(pz)_3](CO)_2(CS)W\text{-}Au(PPh_3)$, and $[HB(pz)_3](CO)_2(CS)W\text{-}Au(PMe_3)$, synthesized by Dr. Angelici's group. In the last section, the most intriguing problem in X-ray crystallography, the phase problem, is closely examined from the view-point of a real-space approach, namely, Patterson superposition, enabling new insight to this old problem to be conveyed.

Each section either has been or will be submitted for journal publication. References apply only to the material contained within that section.

SECTION I

AN X-RAY POWDER DIFFRACTION STUDY OF LEAD DIOXIDE ELECTRODES DOPED WITH BISMUTH, ARSENIC, OR THALIUM

INTRODUCTION

Electrochemical transformations of chemical compounds have very useful commercial applications due to their flexibility in dealing with highly functionalized compounds - the reaction conditions can be controlled merely by setting the voltage.[1] Virtually all organic compounds are predicted, from thermodynamical view point, to be oxidized at potentials accessible with commonly used solid electrode materials (e.g., Pt, Au, and C) in aqueous media by O-transfer reactions from H_2O to the oxidation products.[2] However, these reactions are generally kinetically inhibited because of their complexity.

Lead dioxide has been established as a useful anode for potential electrosyntheses because of its low cost, high electrical conductivity, and high oxygen overpotential.[3] Thermodynamically, lead dioxide is a strong oxidizing agent:

$$PbO_2 + 4H^+ + 2e^- \rightarrow Pb^{2+} + 2H_2O;\ E^o = +1.22V \text{ vs. SCE}$$

A general survey of the anodic response of several compounds at electrodeposited PbO_2 electrodes indicates high reactivity for oxidation of sulfur compounds where at least one pair of non-bonding electrons reside on the sulfur atom. It has been concluded that the O-transfer reactivity of the PbO_2 electrodes results from defects in the surface structure of

the non-stoichiometric oxide. Yeo and Johnson tested this conclusion by altering the surface defect density by doping PbO_2 electrodes with high levels of Group IIIA and VA elements.[4] Plots of the anodic current, i, vs. electrode rotation speed, $\omega^{1/2}$, are shown in Figure 1A for the oxidation of Mn^{2+} at the undoped and doped PbO_2 electrodes. The plots of $1/i$ vs. $1/\omega^{1/2}$ for the same data are shown in Figure 1B. Values of the heterogeneous rate constants (k) calculated from the intercepts according to Levich equation,[5] are given in Table 1. From these data it is apparent that the O-transfer activity of the oxygen-deficient (Group IIIA element-doped) electrodes is less than that of undoped PbO_2, while the activity of the oxygen-rich (Group VA element-doped) electrodes is significantly greater than that of the PbO_2, with the rate being virtually mass-transport limited for the electrode deposited from the solution of the concentration ratio of [Bi]/[Pb] = 1.0. In Figures 2A and 2B, the heterogeneous rate constant for oxidation of Mn^{2+} using Bi-doped PbO_2 electrodes is shown as a function of the concentration of Bi^{3+} in the electrodeposition solution. The greater relative effect of added Bi^{3+} was observed as [Bi]/[Pb] increased, approaching the mass-transport limit at [Bi]/[Pb] = 0.1 for this reaction. The values of the heterogeneous rate constant measured for numerous other O-transfer reactions were also determined to be larger at the Bi-doped electrode compared to PbO_2, as listed in Table 2

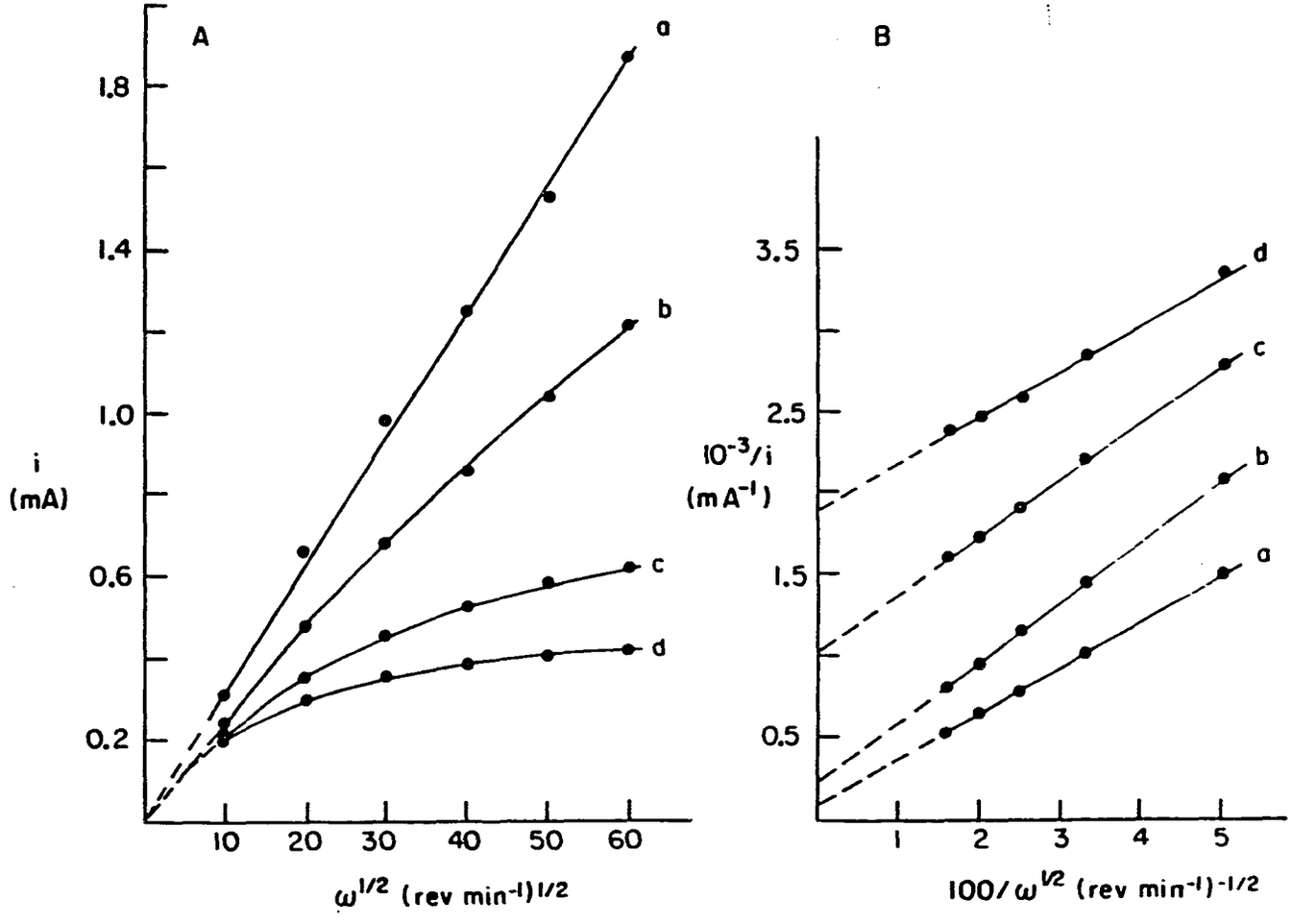

Figure 1. Plots of (A) i vs. $\omega^{1/2}$ and (B) 1/i vs. $1/\omega^{1/2}$ for oxidation of 1.0 mM Mn^{2+}. Curves are for (a) Bi-doped, (b) As-doped, (c) undoped, and (d) Tl-doped electrodes. The concentration of each doping metal was 0.1 mM and 1.0 mM Pb^{2+} in 1.0 M $HClO_4$

Table 1. Rate constants for oxidation of Mn^{2+} at rotated doped PbO_2 disc electrodes

$$Mn^{2+} + 4H_2O \xrightarrow{k} MnO_4^- + 8H^+ + 5e^-$$

Doping ion	Concentration (mM)[a]	k (cm s^{-1})[b]
———	———	4.1×10^{-3}
Tl(III)	0.10	2.3×10^{-3}
In(III)	1.0	3.4×10^{-3}
Ga(III)	1.0	3.5×10^{-3}
As(V)	1.0	5.7×10^{-2}
Bi(III)	1.0	$> 1 \times 10^{-1}$[c]

[a]Electrodes deposited from 1.0 mM Pb(II) / 1.0 M $HClO_4$.

[b]Kinetic measurements in 1.0 mM Mn^{2+} / 1.0 M $HClO_4$.

[c]Effectively mass transport controlled.

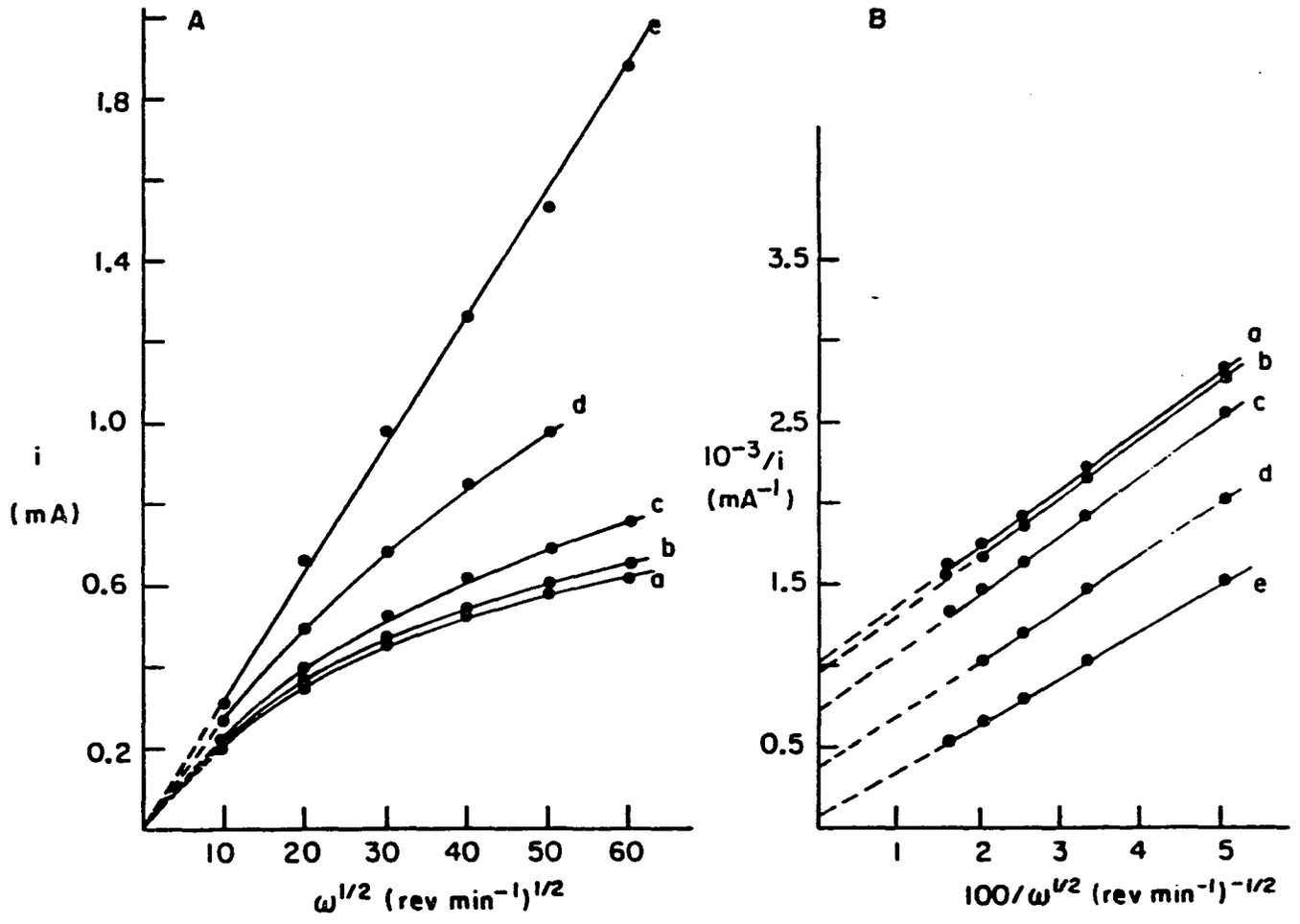

Figure 2. Plots of (A) i vs. $\omega^{1/2}$ and (B) 1/i vs. $1/\omega^{1/2}$ for oxidation of 1.0 mM Mn^{2+} at doped electrodes containing different Bi^{3+} concentration. Electrodes were prepared by electrodeposition using (a) 0.0, (b) 5.0, (c) 10.0, (d) 50.0, and (e) 100.0 μM Bi^{3+} and 1.0 mM Pb^{2+} in 1.0 M $HClO_4$

Table 2. Rate constants for oxidations at rotated undoped and Bi-doped PbO_2 disc electrodes[a]

Compound	$10^3 \cdot k$ (cm s^{-1})[b]	
	undoped	Bi-doped
manganese (II)	4.1(1)	> 100[c]
sulfosalicyclic acid	4.5(9)	11(2)
phenol	no rxn.	> 100[c]
hydroquinone	9.7(4)	29(12)
cystine	9.0(4)	15(4)
thiophenacetic acid	1.4(3)	22(12)

[a]PbO2 deposited from 1.0 mM Pb(II) / 1.0 mM $HClO_4$; Bi-doped PbO_2 deposited from 1.0 mM Pb(II) / 1.0 mM Bi(III) / 1.0 M $HClO_4$.

[b]Uncertainty given for 90% confidence interval. Measurements done for 1.0 mM analyte in 1.0 M $HClO_4$.

[c]Effectively transport limited.

(Notice the oxidation of phenol to benzoquinone, which is barely perceptible at undoped electrodeposited PbO_2 electrodes, but is virtually mass-transport limited for the electrode of [Bi]/[Pb] = 1.0). The increased rate of O-transfer reactions for the Bi-doped PbO_2 electrodes was tentatively attributed to the high density of surface sites corresponding to Bi(V) centers where excess surface oxygen could exist which was not stabilized as much at the surface of the undoped PbO_2 electrodes.

The reactions shown thus far are not sufficiently adequate to compare Bi-doped electrodes with [Bi]/[Pb] $\geq$ 0.1 since these reactions become virtually mass-transport limited. However, water molecules can also be oxidized yielding oxygen gas at the anode, the oxygen overpotentials at constant currents being plotted in Figure 3 as functions of the ratio of [Bi]/[Pb] in the deposition solution. The oxygen was produced at the least potential with the electrode of [Bi]/[Pb] = 0.7. The anodic currents for the oxidation of 2-thiophencarboxylic acid for the PbO_2 electrodes with different Bi-doping levels is plotted as functions of $\omega^{1/2}$ in Figure 4. This result also clearly shows that the electrode of [Bi]/[Pb] = 0.7 has the greatest oxidizing catalytic activity.[4]

Results of linear sweep voltammetry are shown in Figure 5 for undoped and Bi-doped electrodes.[4] Curves a-c correspond to the negative scan of electrode potential to

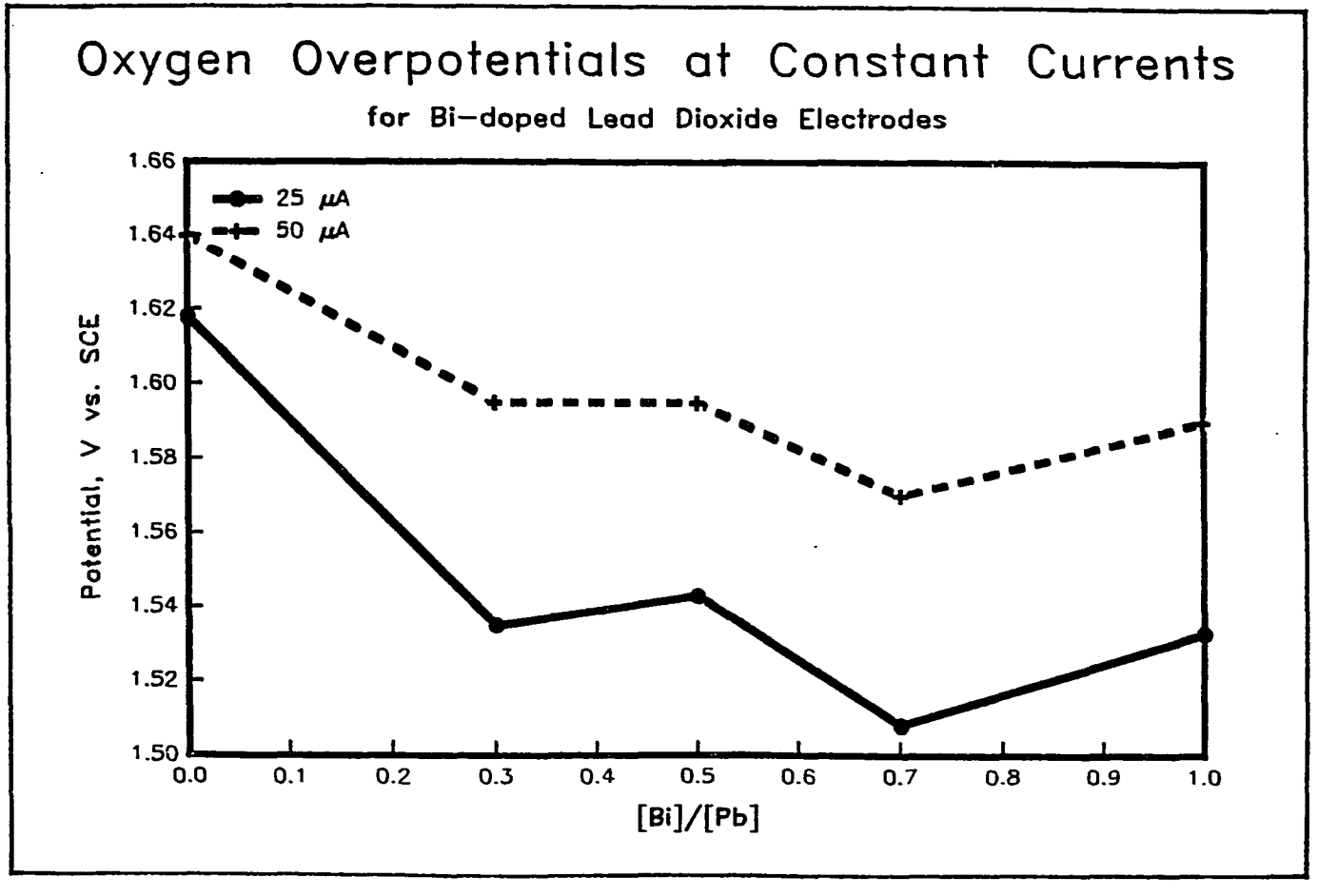

Figure 3. Plots of the oxygen overpotentials vs. concentration ratio of [Bi]/[Pb] in the deposition solution. The potentials were measured at 25 (——) and 50 (---) μA

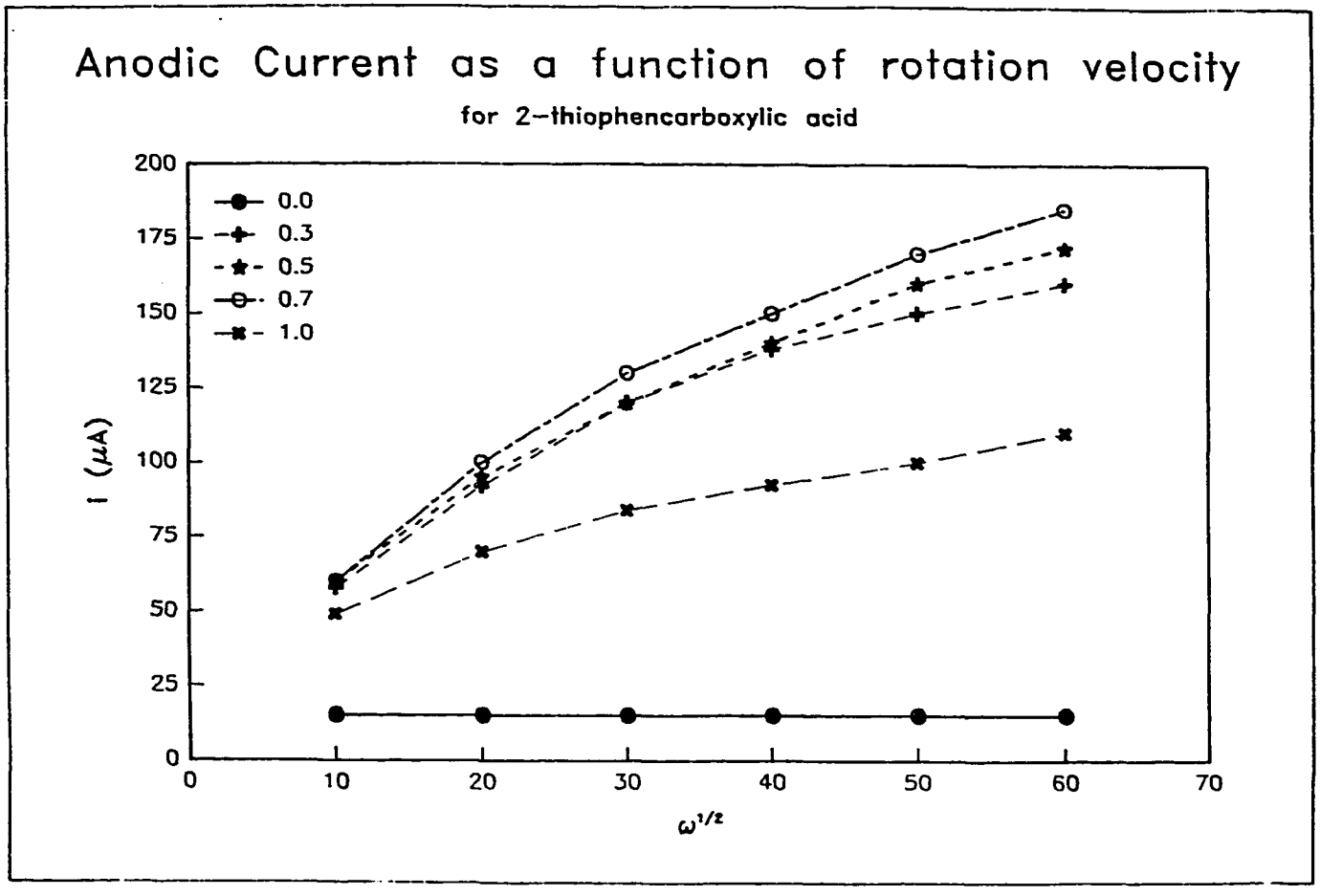

Figure 4. Plots of i vs. $\omega^{1/2}$ for oxidation of 2-thiophencarboxylic acid. Conditions for electrodeposition of the electrodes are 0.0 (·), 0.3 (+), 0.5 (*), 0.7 (o), and 1.0 (x) mM Bi^{3+} and 1.0 mM Pb^{2+} in 1.0 M $HClO_4$

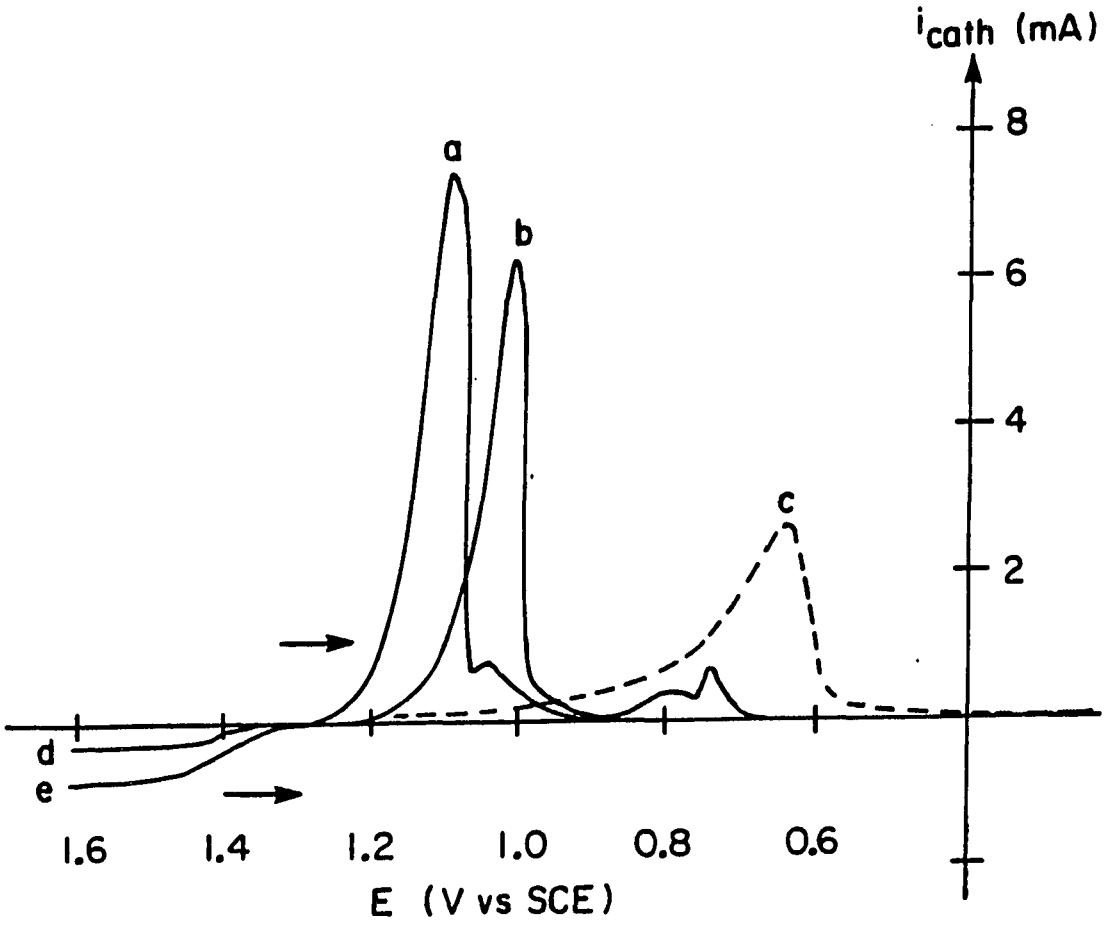

Figure 5. Linear sweep voltammograms obtained for the negative scan along the arrow direction. Electrodes were deposited from (a,d) 1.0 mM Pb^{2+}, (b) 1.0 mM Pb^{2+} and 0.1 mM Bi^{3+}, and (c,e) 1.0 mM Pb^{2+} and 1.0 mM Bi^{3+} in 1.0 M $HClO_4$. The bulk concentration of Mn^{2+} was (a-c) 0.0 mM and (d,e) 1.0 mM, respectively. Deposition was at 1.60 V vs. SCE for 1.0 min at 900 rev min^{-1}

determine the effect of doping on potential at which cathodic dissolution of the oxide occurs. Increasing the level of Bi in the PbO_2 electrodes clearly increases the stability of the electrodes. The voltammetric range is increased for the Bi-doped electrode and the rate of chemical corrosion by chemical reducing agents under open circuit conditions is expected to decrease, representing a significant advantage for these electrodes.

The basic objective of this study is to understand why, from a structural point of view, the Bi-doped electrodes show increased catalytic activity in regards to oxidation and why they might be expected to show anti-corrosion stability. One can expect that the doped oxides either have a structure corresponding to a metal-substituted lead dioxide or belong to some new structural type(s). In the case of metal substitutions, these might be random substitutions, or substitutions which give rise to short-range or long-range ordering. Long-range orderings of Pb and Bi atoms would be very difficult to detect using X-ray diffractions because the X-ray scattering powers of Pb and Bi are very close to each other. Superlattice peaks due to long-range orderings will be more easily detected with As-doped electrodes since As has significantly different scattering powers from Pb and both As-doped and Bi-doped electrodes show enhanced activities. On the other hand, if some new structures were produced through doping, one could expect to characterize them via

powder pattern indexings and subsequent structure determination.

The Rietveld-type full-profile fittings have been used widely for neutron powder diffraction patterns and found extremely useful for analyzing crystal structures.[6] Recently, more and more applications of the method to X-ray powder diffraction patterns have been cited in the literature following the pioneering work by Young.[7] In these methods, intensities as well as positions of powder diffraction peaks are readily checked against the model structures. Prior to the advent of these methods, powder diffraction patterns were used mostly for identifying known phases by comparing with standard patterns, and this is still an extremely useful analytical tool. Now, however, by applying Rietveld methods, one can obtain estimates of atomic parameters (positions and temperature factors) as well as pattern parameters (peak width, cell dimensions, etc). If a series of diffraction patterns for samples with varying preparation conditions have been obtained, the precise variations of those parameters can be easily monitored at the atomic level.

The crystal structures of lead dioxides have been studied extensively via various techniques, primarily due to its use in lead acid storage batteries.[8-12] Two crystal modifications of PbO_2 are known: α- and β-PbO_2. The basic structural building block is a distorted octahedron of oxygen atoms surrounding a lead atom in both forms. In β-PbO_2 (the

"rutile" form), neighboring octahedra form a linear chain by sharing opposite edges, as shown in Figure 6. The chains propagate along the tetragonal c axis and are interconnected together by sharing oxygen atoms with neghboring chains - oxygen atoms in the basal plane of an octahedral chain occupy axial position of the neighboring chain. In α-PbO_2 (the "columbite" or orthorhombic form), the octahedra are arranged in a zig-zag manner by sharing alternate edges,as shown in Figure 7. The connection among the chains in α-PbO_2 is more complicated than in β-PbO_2. So far, no single crystal structure determination of either form has been reported. Chemical analyses of both α- and β-PbO_2 are consistent with a composition of $PbO_{1.80-1.98}(OH)_{0.04-0.26}$;[11] however, recent neutron Rietveld analyses of β-PbO_2 showed small metal deficiency although the departure from stoichiometry was insignificant.

We report here our results on the structural characterization of those doped lead dioxides using X-ray polycrystalline diffraction and subsequent Rietveld analyses. Since the activity depends on the amount of doped Bi relative to Pb, diffraction patterns were obtained over a range of Bi concentrations. Correlations between the patterns and the activities will be discussed.

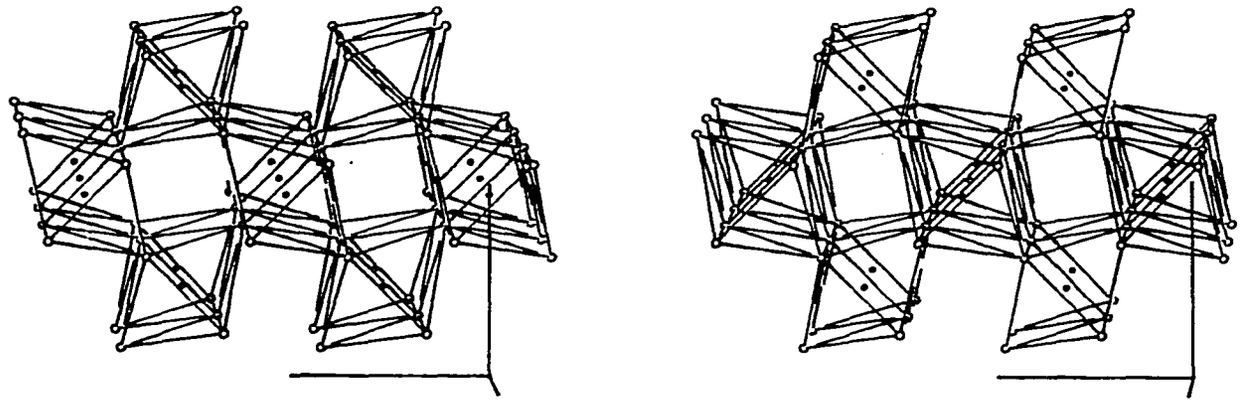

Figure 6. Stereoview of the crystal structure of β-PbO_2 (rutile), viewed down the tetragonal c axis. The solid lines represent edges of the oxygen octahedra. Circles in the middle of the octahedra represent the metal positions

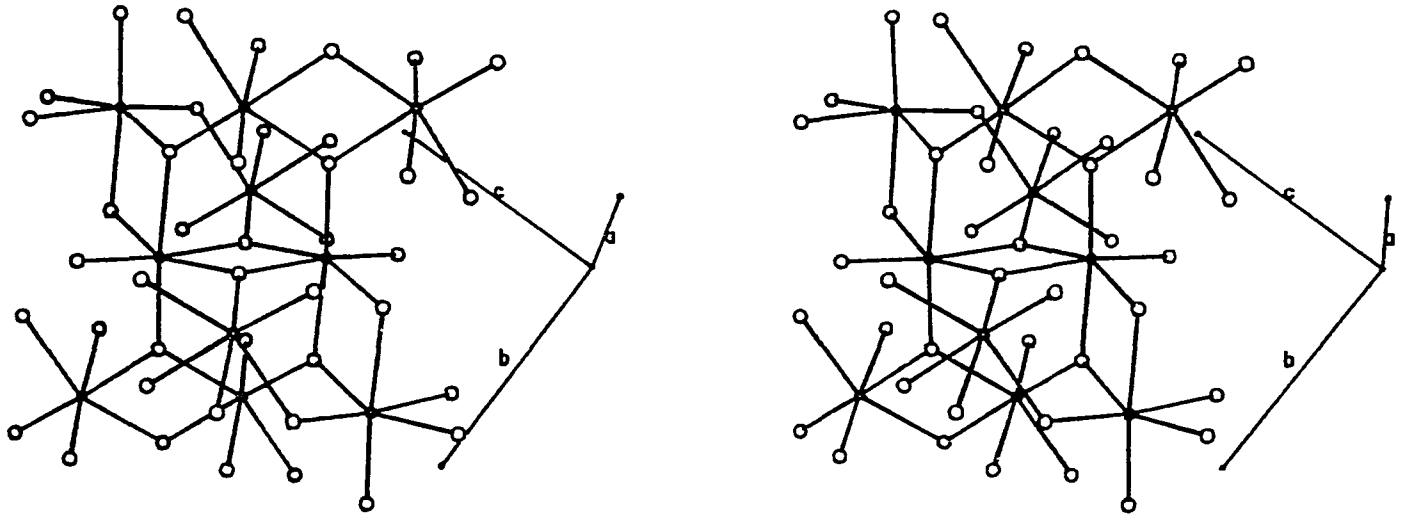

Figure 7. Stereoview of the crystal structure of α-PbO_2 (columbite). The solid lines represent bonds between metal (small) and oxygen (larger circle) atoms

EXPERIMENTAL SECTION

Sample preparation

Lead dioxide electrodes doped with bismuth, arsenic, or thallium were prepared on a gold rotating disc electrode (0.496 cm^2) by electrodeposition at 1.60V (vs. SCE).[4] The concentrations in the deposition solutions were 0, 0.1, 0.2, 0.3, 0.5, 0.7, and 1.0 mM for bismuth, and 0.1 mM for arsenic and thallium, respectively, while the concentration of lead was fixed to 1.0 mM in 1.0 M $HClO_4$ solution. The undoped electrode was prepared as a control. The deposition time was approximately 20 min in each case. These electrodes were taken out of the solution and mounted on a diffractometer in the reflection geometry. In order to monitor the properties of the crystalline particles (e.g., preferred orientation and particle size) as well as atomic parameters, no other treatment on the sample was carried out preliminary to the diffraction experiment. Random powder samples of [Bi]/[Pb] = 0.0 and 1.0 were also prepared by stripping the deposit from the gold electrode surface either mechanically or by applying a reverse potential after the deposition was complete. Pellets of such oxides were dried and ground into fine powder. These powder samples were used to obtain diffraction patterns free from preferred orientation effects so that accurate identification of the sample was possible.

Diffraction data collection

The random powder samples were spread on a Si single crystal of 2.4 cm diameter and mounted on a powder diffractometer. Other electodes were directly transferred to the diffractometer and mounted. The diffractometer used for all these diffraction experiments was an automated Picker unit equipped with a diffracted-beam graphite monochromator. A θ-θ stepscan procedure was employed with 2θ steps of 0.04° over the 4.04 - 50.00° range using MoKα radiation. The step counting time used was 30 sec per step for those of [Bi]/[Pb] = 0.1, 0.2, 0.3, and 1.0, and 10 sec per step for all others.

Diffraction pattern fitting

Full-profile pattern fittings were undertaken using the Rietveld-type program KDBW, a local modification of DBW 3.2.[13] Local modifications included: (i) adoption of several more profile functions than those originally supplied in the DBW 3.2; (ii) sample width correction; (iii) an improved preferred orientation correction; and (iv) employment of the maximum neighborhood method[14] instead of the ordinary Newton-Raphson algorithm for least-squares minimization. The new least-squares approach will be discussed first and other modifications discussed later.

At the j-th step, the expected intensity is calculated as:

$$y_{cj} = \sum_p A_p \sum_k L_k |F_k|^2 \cdot \Phi(2\theta_j - 2\theta_k) P_k + BK_j$$

where A_p is a scale factor for the p-th phase, L_k contains correction factors such as Lorentz, polarization, multiplicity, and absorption factors, F_k is the structure factor for the k-th reflection, Φ_k the reflection profile function, P_k the preferred orientation function, and BK_j the background intensity at the j-th step. The summations are over all the phases and reflections. The normal equation, $\underline{\underline{A}}\underline{\delta} = \underline{g}$, is solved for the parameter shifts, $\underline{\delta}$, where the matrix elements for $\underline{\underline{A}}$ and $\underline{g}$ are calculated from:

$$a_{jj'} = \sum \omega \frac{\partial y_c}{\partial p_j} \cdot \frac{\partial y_c}{\partial p_{j'}}, \qquad g_j = \sum \omega (y_o - y_c) \frac{\partial y_c}{\partial p_j}$$

However, in the maximum neighborhood method, the equation is first appropriately scaled as:

$$\underline{\underline{A}}^* = \left(\frac{a_{jj'}}{\sqrt{a_{jj}}\sqrt{a_{j'j'}}} \right), \quad \underline{g}^* = \left(\frac{g_j}{\sqrt{a_{jj}}} \right), \quad \underline{\delta} = \left(\frac{\delta_j^*}{\sqrt{a_{jj}}} \right)$$

The actual matrix equation solved is:

$$(\underline{\underline{A}}^* + \lambda \underline{\underline{I}})\ \underline{\delta}^* = \underline{g}^*$$

where λ is a constant needed to be optimized for each cycle of least-squares; one of the optimization strategies involved is shown in Figure 8. The constant ν is greater than 1, typically 10. As an initial λ, one may start with 0.01. R° is the residual from previous cycle or that obtained from the initial parameters prior to any least-squares cycles. $R(\lambda)$ represents the residual calculated using parameters already corrected by solving the normal equation involving λ. The strategy is: (i) calculate y_c and $R(\lambda/\nu)$, and compare with R°; (ii) if it is smaller than R°, decrease λ by successive division by ν until $R(\lambda) \leq R^\circ$; (iii) if $R(\lambda/\nu)$ in the step (i) is greater than R°, increase λ by successive multiplication by ν until $R(\lambda) \leq R^\circ$; in either case, once the condition is met, proceed to a new cycle at (iv) after storing λ and setting R° to $R(\lambda)$. A flexible control of the minimization process can be achieved by adjusting λ in this way. Ordinary least-squares results can be obtained when $\lambda = 0$ and steepest-descent results when $\lambda = \infty$, and it was shown in general that the larger λ is, the closer the solution is to the steepest-descent result. Thus, it is the optimum interpolation of the Newton-Raphson which is fast but susceptible to correlations and the steepest gradient method which is slow but less susceptible to correlation problems. The new approach eliminates the use of damping factors in cases of potential overshfts in parameters. Its power is most appreciated when high correlations among parameters

Flow diagram for the optimization of "λ"

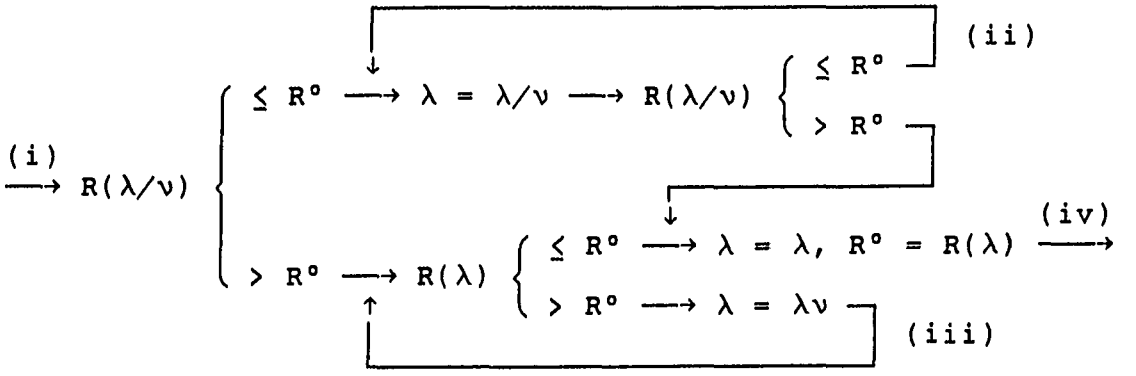

Figure 8. A flow diagram for the optimization of λ, where $R = \Sigma\omega(y_o - y_c)^2$. See the text for detail

prevent the ordinary method from converging. The only drawback of the method is that it can require more computing time than ordinary methods.

All the difraction patterns were readily identified as that of β-PbO_2 by simple inspection of the peak positions and by the subsequent successful Rietveld analyses of the patterns. The samples of $0 < [Bi]/[Pb] \leq 0.3$ contained additional small peaks which were identified as those of the α-PbO_2 phase. Since the samples deposited on Au electrodes were not thick enough to inhibit scattering by the substrate using MoKα radiation, the diffraction patterns included the elemental gold phases as well. Since the current version of the program only allows up to two phases to be included, parameters of only β-PbO_2 and Au phases were included in the refinements. For those patterns containing α-PbO_2 phase in addition, separate refinements of the α-PbO_2 phase were applied to the difference patterns after the contributions from the other two phases had been taken out. Parameters refined for each phase were the scale factor, peak width parameters (U, V, and W in $FWHM^2 = U \cdot \tan^2\theta + V \cdot \tan\theta + W$), unit cell parameters, an asymmetry parameter, preferred orientation parameters, and atomic parameters (e.g., x of the oxygen atom and isotropic B). The following parameters were treated as global encompassing both phases: $2\theta_o$, the profile shape parameter, and the sample width parameter.

Pearson VII functions were used to describe peak shapes for all the pattern since these peak shapes were typically between Gaussian and Lorentzian. The profile function is defined as

$$\Phi(x) = [1+4(2^{1/\gamma}-1)x^2]^{-\gamma} \qquad (1)$$

where $x = (2\theta-2\theta_{Bragg})/FWHM$ and γ is the refinable parameter. If γ is 1, the profile is Lorentzian, and if γ is ∞, it is Gaussian. By applying correct derivatives we can overcome the problem in refining γ noted by others.

One of the advantages of the reflection geometry with flat samples is that it eliminates the need for an absorption correction providing that the sample face is long enough to cover the incident beam throughout the angular range. This condition will be satisfied if $t \cdot \sin\theta \geq w$ for the lowest angle reflection (see Figure 9 for the definition of t and w). For the electrode samples, the sample surface diameter is ca. 0.7 cm and the incident beam is ca. 0.2 cm, and therefore reflections below 33° 2θ require intensity correction. If one assumes that flux density of the incident beam across the beam is uniform, the correction factor for the reflections below the limit noted above is simply $t \cdot \sin\theta/w$. Since the factor should be 1 for a reflection beyond the limit, a compact form of the correction factor is

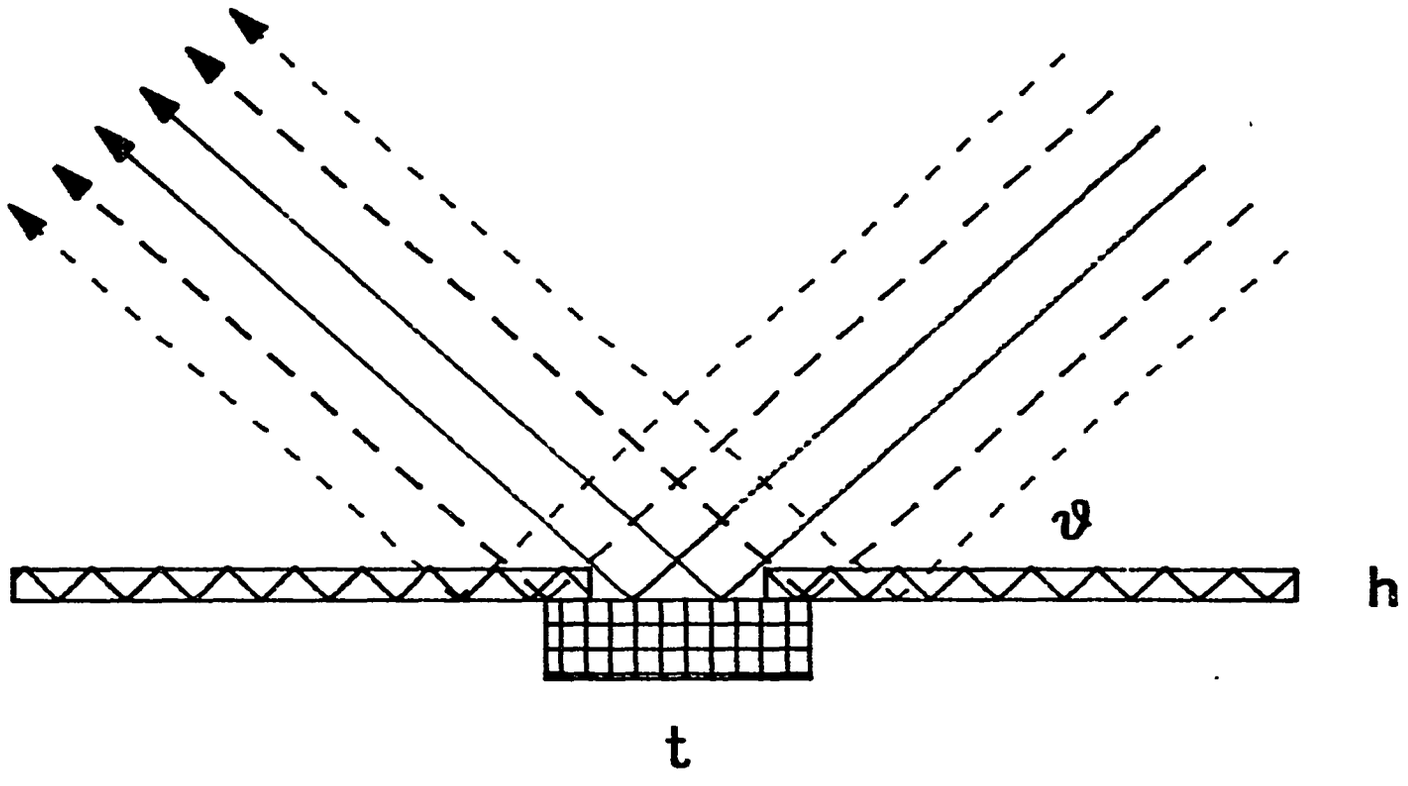

Figure 9. Diagram of reflection geometry showing relationships between sample size (t) and beam width (w). The outermost beam path (dashed) is for an ideal sample of an extended face, the middle path (broken) for a sample of a finite size (t), and the innermost path (solid) for a sample with covers of height (h)

given by

$$\min (\tau \cdot \sin\theta, 1) \qquad (2)$$

where τ is the longitudinal width ratio equal to t/w. This expression was confirmed by comparing intensities of reflections over a wide 2θ range from samples possessing varying coverages. In particular, CeO_2 standard powder sample from NBS was mounted on a 5 cm long Al holder. The lowest 16 reflections ranging in 2θ from 13.3 to 40.3°, were step-scanned with a sample of widths varying from 0.2 - 2.0 cm in steps of 0.2 cm and a width 5.0 cm, using two thin lead metal pieces to cover the sample surface. Since the thin lead cover created shadows at both sides of the beam path, as shown in Figure 9, the actual factor used was

$$\min \left(\frac{t \cdot \sin\theta - h \cdot \cos\theta}{w}, 1 \right)$$

Via a non-linear least-squares method, the best h and w were determined as 0.6001 and 1.924 mm, respectively. The fitting result, as shown in Figure 10, was excellent (Rw = 7.74%). The incident beam slit size was 1 mm. Allowing some divergence of the beam, this result is physically meaningful. For actual electrode samples, the refined τ was 3.3(1) - 4.2(2).

The atomic multiplicity ratio of Pb and O was kept at the ideal value of 0.5 since the refinement of O occupancy

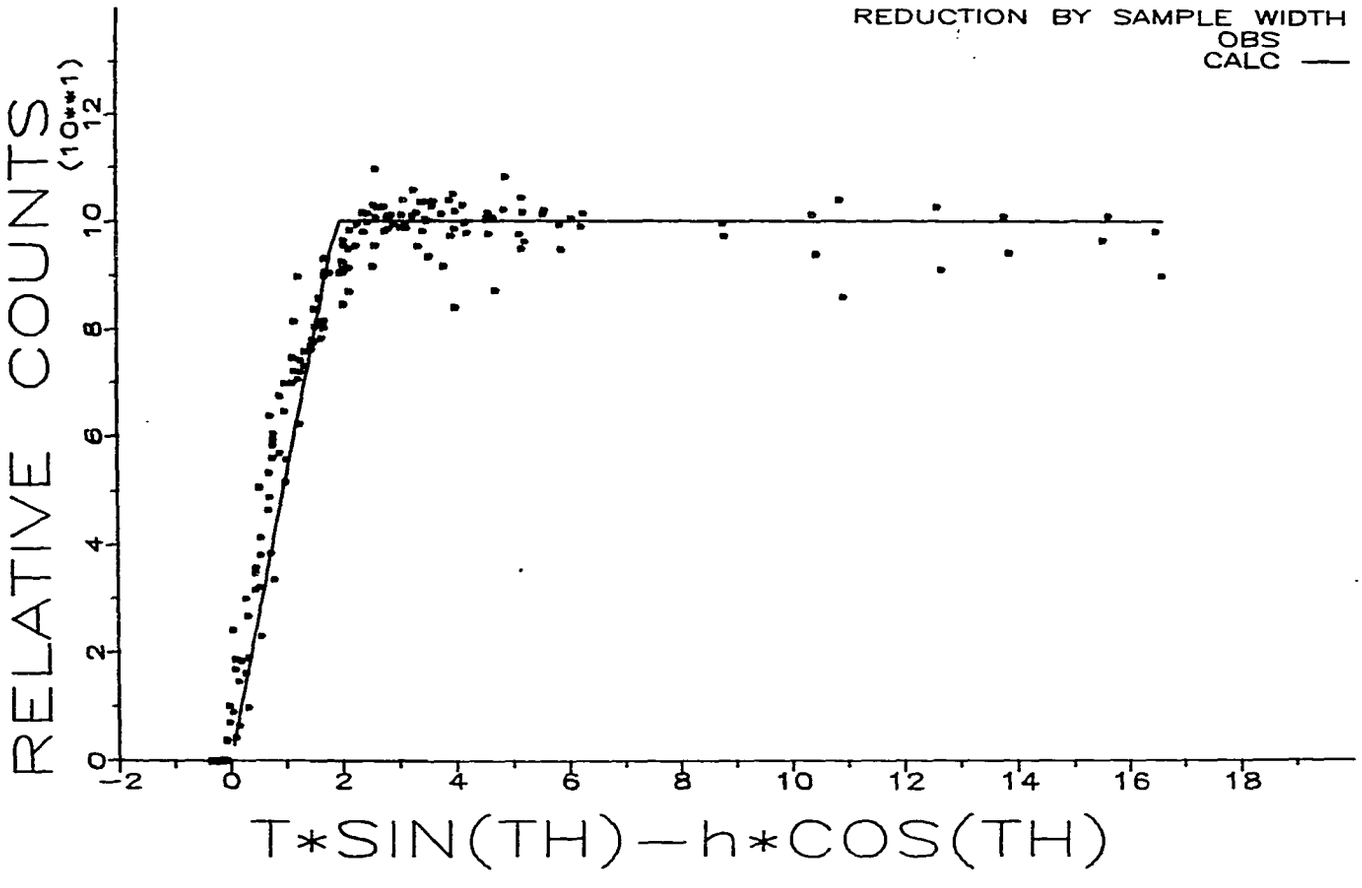

Figure 10. Plots of normalized intensity vs. t·sinθ-h·cosθ for NBS standard CeO_2, showing intensity reduction due to small sample size. Observed data (*) and calculated line are shown

produced a result not significantly different from the ideal value. Since the Bi scattering power is very close to that of Pb and there are uncertainties associated with the charge on the metal atom, we used the neutral Pb scattering power on the metal site of the β-PbO_2 for all the data sets.

The preferred orientation characteristic of two-dimensional crystallites on flat sample holder were noticed and corrected using the Gaussian model.[15] Since at least two directions of preferred orientation were noticed, we used the following slightly modified formula:

$$PO = 1-b_1-b_2+b_1\sqrt{\pi a_1}\exp(-a_1\cdot\alpha_1^2)+b_2\sqrt{\pi a_2}\exp(-a_2\cdot\alpha_2^2) \quad (3)$$

where a_i and b_i are refinable parameters and α_i is the angle between the diffraction vector and the i-th preferred orientation direction. The preexponential factors, $\sqrt{\pi a_i}$, relieve the correlation problem existing otherwise among the scale factor and these parameters, and also ensure the normalization of the correction factor, for at least large a_i, such that:

$$\Sigma\ (PO) \simeq \frac{2}{\pi}\cdot\int_0^{\pi/2} d\alpha\cdot(PO) \simeq 1$$

where the sum is over the all diffraction vectors.

Refined lattice parameters, preferred orientation parameters, and profile shape parameters are given in

Tables 3, 4, and 5, respectively, while scale factor, atomic parameters, and sample size parameter are given in Table 6 along with the weighted pattern residual index.

Table 3. Variations of lattice parameters of β-PbO_2 as functions of the ratio of Bi/Pb concentrations in the solution

x	a	c	V	y[a]
0[b]	4.9542(7)	3.3846(6)	83.07(3)	——
0	4.9561(11)	3.3789(12)	83.00(5)	——
0.1	4.9478(14)	3.3819(17)	82.79(6)	1.02
0.2	4.9633(7)	3.3951(8)	83.64(3)	0.86
0.3	4.9632(7)	3.3978(7)	83.70(3)	0.89
0.5	4.9719(6)	3.4070(6)	84.22(3)	0.89
0.7	4.9798(4)	3.4165(4)	84.72(2)	0.88
1.0	4.9855(3)	3.4249(4)	85.13(1)	0.87
1.0[b]	4.9882(5)	3.4251(4)	85.22(2)	0.86
0.1[c]	4.9618(58)	3.3671(39)	82.90(22)	——
0.1[d]	4.9377(20)	3.3397(24)	81.42(9)	——

[a] $y = [Bi^{5+}]/([Bi^{5+}]+[Bi^{3+}])$.
[b] Powder samples.
[c] PbO_2 electrode sample doped with Tl^{3+}.
[d] PbO_2 electrode sample doped with As^{5+}.

Table 4. Preferred orientation parameters for undoped and doped β-PbO_2 electrode samples

x	(020)		(121)	
	a_1	b_1	a_2	b_2
0	6.67(95)	0.169(14)	5.02(46)	0.706(43)
0.1	6.00(102)	0.083(9)	7.37(32)	0.916(14)
0.2	3.21(61)	0.036(7)	9.08(28)	0.890(8)
0.3	6.99(68)	0.114(6)	6.21(21)	0.856(14)
0.5	7.95(34)	0.334(7)	4.83(28)	0.590(25)
0.7	5.82(21)	0.796(5)	4.79(36)[a]	0.154(11)
1.0	5.34(12)	0.529(10)	4.38(40)	0.360(30)
0.1[b]			1.93(124)[a]	0.913(258)
0.1[c]	10.54(78)	0.693(17)	2.34(19)	0.307

[a]Parameter values for (011) direction. Preferred orientation direction was detected along (011), not (121) direction.

[b]PbO_2 electrode sample doped with Tl^{3+}. No preferred orientation along (020) direction was detected.

[c]PbO_2 electrode sample doped with As^{5+}. b_2 was constrained to be $1-b_1$.

Table 5. Peak profile parameters as functions of the concentration ratio of [Bi]/[Pb] in the solution

x[a]	U[b]	V	W	γ[c]	P[d]
0	2.41(66)	-1.34(27)	0.091(10)	1.80(7)	0.156(35)
0.1	13.85(120)	-5.08(44)	0.497(41)	1.86(13)	0.462(94)
0.2	1.28(21)	-0.45(9)	0.070(9)	1.07(2)	-.204(31)
0.3	2.25(18)	-1.27(9)	0.202(11)	1.44(4)	0.511(32)
0.5	0.43(11)	-0.20(5)	0.058(6)	2.28(13)	0.941(127)
0.7	0.25(7)	-0.11(3)	0.025(3)	1.44(4)	0.769(85)
1.0	0.50(5)	-0.34(2)	0.074(3)	2.03(5)	1.584(58)
0.1[e]	5.68(917)	-1.98(344)	0.587(306)	1.81(6)	0.055(28)
0.1[f]	87.81(769)	-28.32(257)	2.393(213)	2.24(18)	0.143(29)

[a] x = [Bi]/[Pb].

[b] $FWHM^2 = U \cdot \tan^2\theta + V \cdot \tan\theta + W$.

[c] The exponent used for Pearson VII function.

[d] The asymmetry correction parameter. The asymmetry correction factor defined as $Z(2\theta_j - 2\theta_k) = 1 - P \cdot (2\theta_j - 2\theta_k) \cdot |2\theta_j - 2\theta_k| / \tan\theta_k$ is applied to low angle reflections (usually below 25° 2θ).

[e] PbO2 electrode sample doped with Tl^{3+}.

[f] PbO2 electrode sample doped with As^{5+}.

Table 6. Other refinement results

x[a]	Scale[b]	B(Pb)	x(O)	B(O)	τ[c]	Rw[d]
0[e]	0.108(2)	1.20(7)	0.302(4)	6.40(104)	5.96(10)	7.19
0	0.164(11)	3.33(19)	0.323(5)	0.29(79)	4.05(18)	9.78
0.1	0.325(29)	2.31(15)	0.298(6)	-.74(61)	3.20(20)	17.84
0.2	0.290(13)	1.76(8)	0.316(5)	0.64(51)	3.20(10)	17.58
0.3	0.247(11)	2.31(12)	0.332(3)	-.13(42)	4.06(13)	15.87
0.5	0.201(9)	1.27(11)	0.300(3)	-.37(41)	3.91(13)	16.26
0.7	0.367(19)	3.05(12)	0.307(4)	5.19(97)	3.36(11)	10.78
1.0	0.324(13)	3.27(7)	0.326(3)	6.20(70)	3.45(8)	14.08
1.0[e]	0.0439(5)	0.96(6)	0.304(3)	2.17(71)	9.92(26)	6.84
0.1[f]	0.088(7)	4.48(36)	0.32(2)	0.3(20)	2.21	13.32
0.1[g]	0.689(72)	2.88(26)	0.286(8)	4.7(25)	3.49(24)	12.16

[a] $x = [Bi]/[Pb]$.

[b] Scale $\times 10^4$ for 10 sec counts.

[c] The longitudinal width ratio of the sample to the incident beam.

[d] $Rw = [\Sigma\omega(y_o-y_c)^2/\Sigma\omega y_o^2]^{1/2}\%$, where $\omega = 1/y_o$.

[e] Powered samples.

[f] PbO_2 electrode sample doped with Tl^{3+}.

[g] PbO_2 electrode sample doped with As^{5+}.

RESULTS and DISCUSSION

The observed and calculated profiles of all the diffraction patterns are shown in Figure 11A-K. Doping bismuth into the β-PbO_2 lattice can result in substitution of Pb by Bi in the metal position and/or insertion of Bi in the interstitial positions. Our X-ray diffraction patterns do not contain any new lines other than those of the α/β-PbO_2 and Au phases, and the powder diffraction profile of the Bi-doped electrode of [Bi]/[Pb] = 1.0 resembles that of the undoped electrode. This excludes the latter as a possible model of the structure. In fact, this conclusion is strongly supported by the successful fitting of the Bi-doped patterns with β-PbO_2 structural models. Since the X-ray scattering powers of Pb and Bi, either in neutral or ionic states, are very close to each other, long-range orders, if any, are very difficult to detect, at least with X-ray diffraction equipment. However, there are several observables which are sensitive to the substitution of Pb by Bi.

Lattice parameters

Table 3 shows an increase in the unit cell volume as the Bi concentration increases. It is known that lead and bismuth have different ionic radii (Pb^{4+} = 0.775, Bi^{5+} = 0.76, Bi^{3+} = 1.03 A).[16] If all the Bi in the lattice are

Figure 11. The observed (|) and calculated (solid line) X-ray diffraction profiles plotted vs. 2θ. The solid line connecting the bottom of the peaks represents the background function used. Difference between y_o and y_c is plotted under the profile. The faint tick marks represent peak positions for β-PbO_2, while the thicker ones represent Au peak positions. Conditions are (A) undoped PbO_2 powder, (B) Bi-doped PbO_2 powder of [Bi]/[Pb] = 1.0, and electrodes with the ratio [Bi]/[Pb] of (C) 0.0, (D) 0.1, (E) 0.2, (F) 0.3, (G) 0.5, (H) 0.7, and (I) 1.0, (J) As-doped electrode with [As]/[Pb] = 0.1, and (K) Tl-doped electrode with [Tl]/[Pb] = 0.1 in the deposition solution

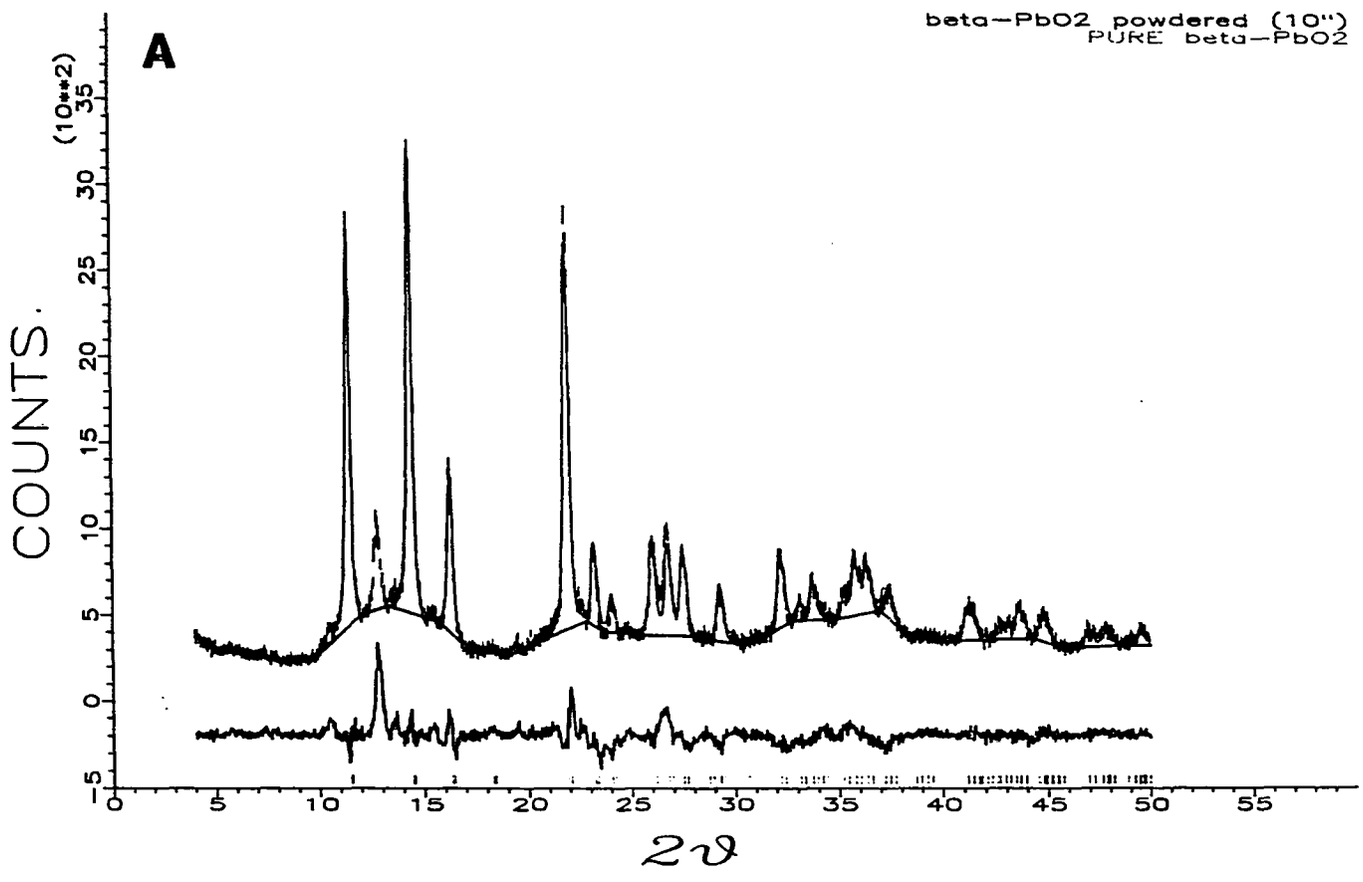
A
beta—PbO2 powdered (10")
PURE beta—PbO2
COUNTS.
(10**2)
35
30
25
20
15
10
5
0
-5
0
5
10
15
20
25
30
35
40
45
50
55
2θ

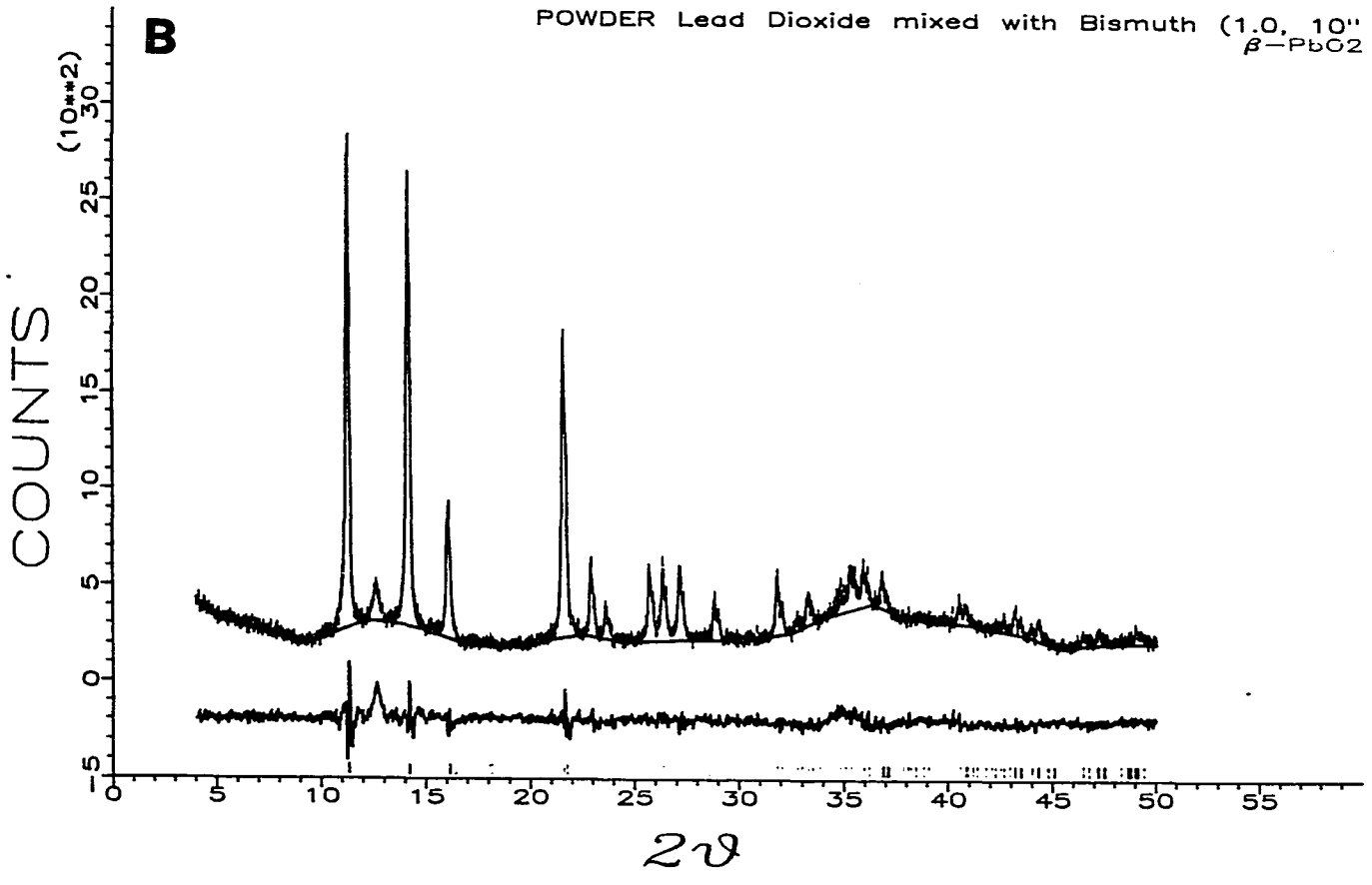

Figure 11 (Continued)

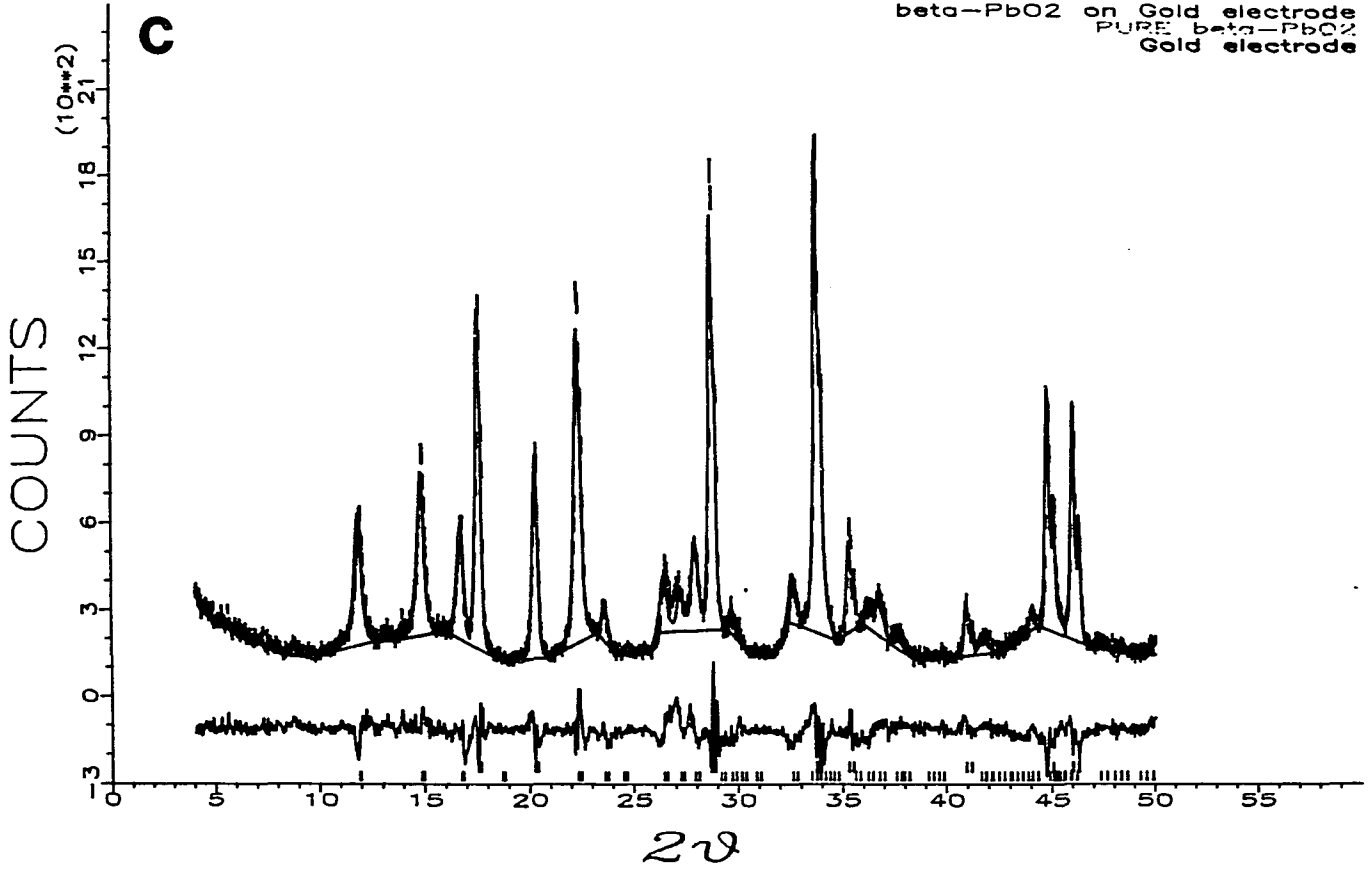

Figure 11 (Continued)

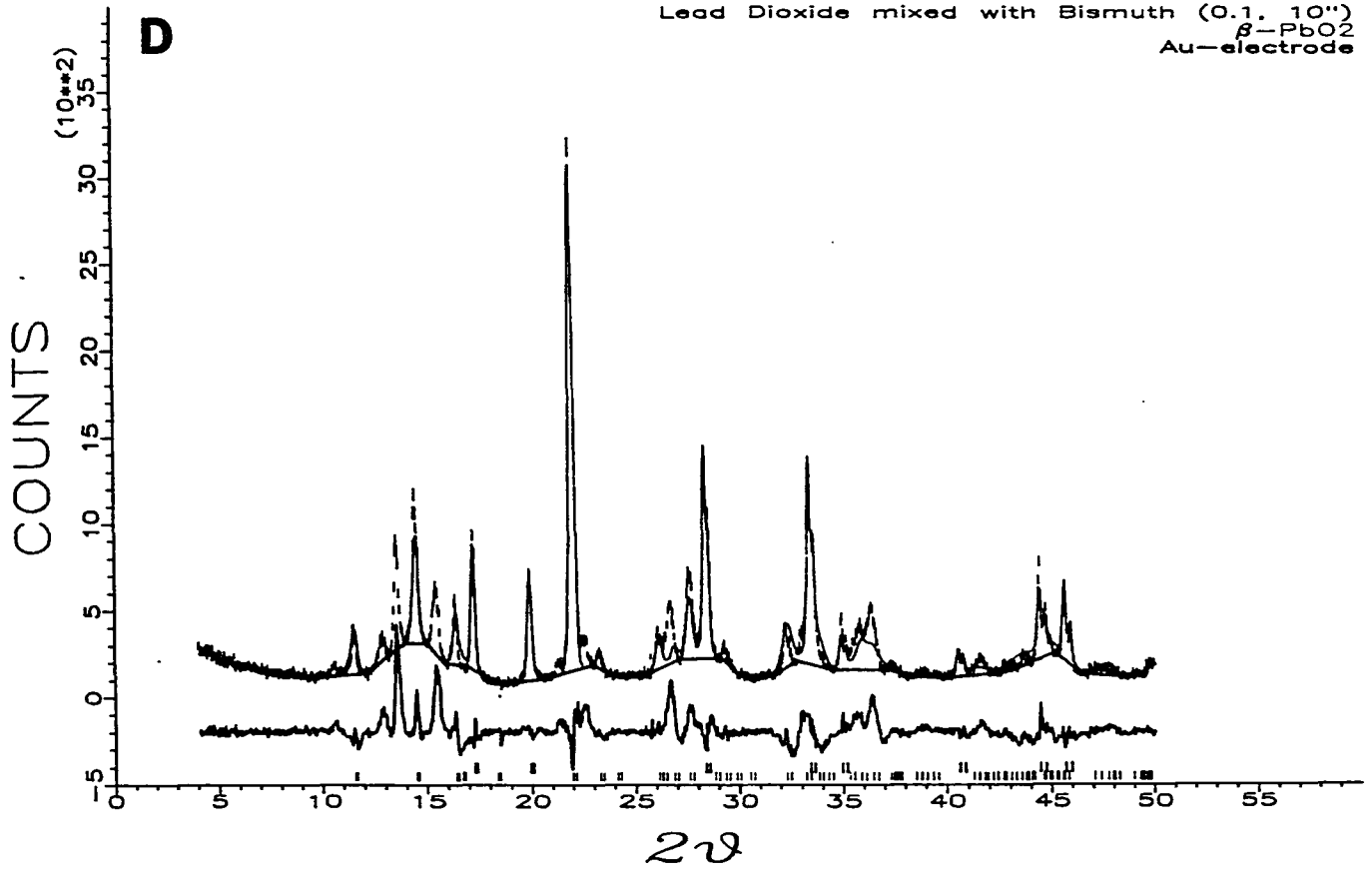

Figure 11 (Continued)

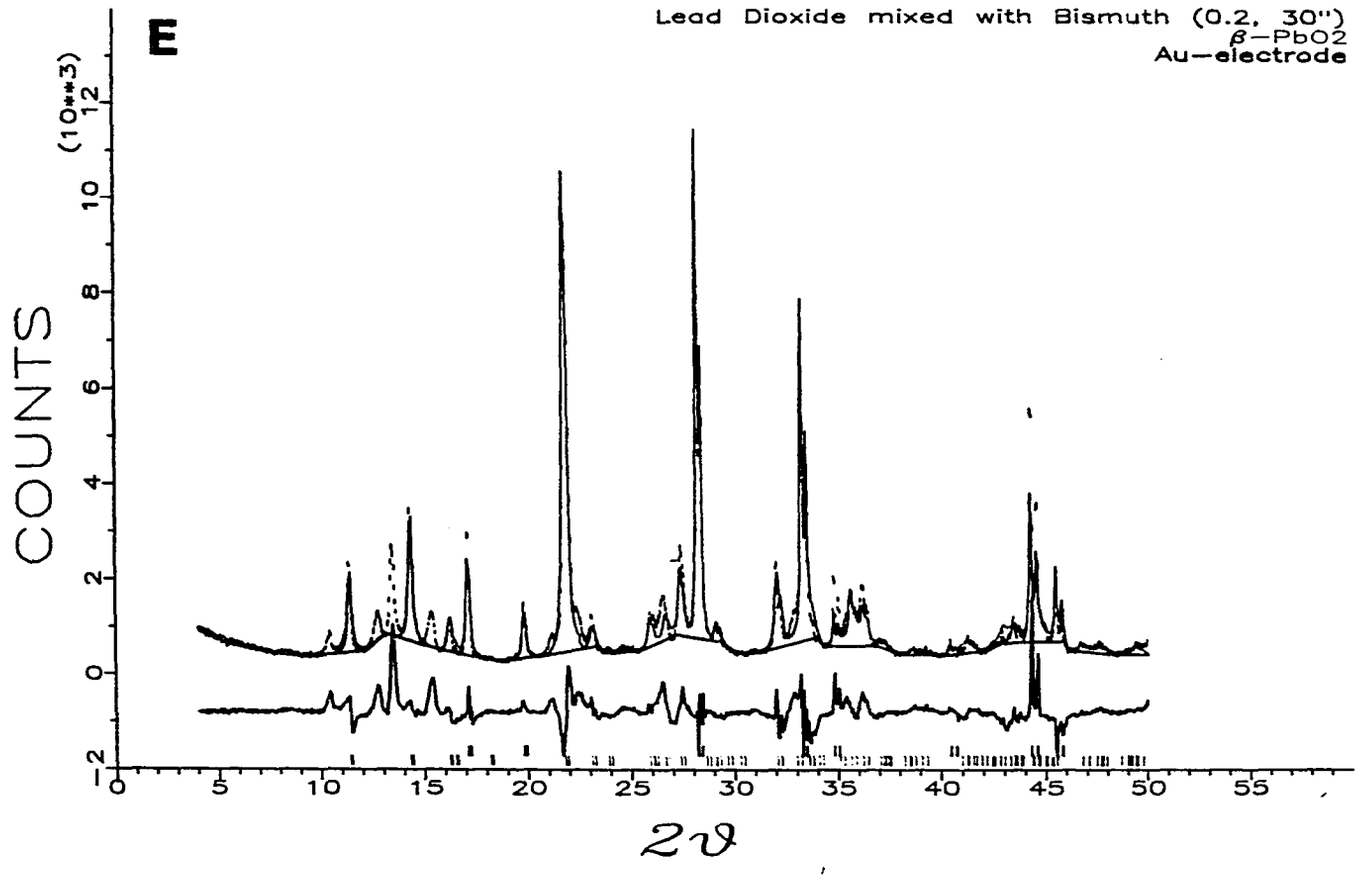

Figure 11 (Continued)

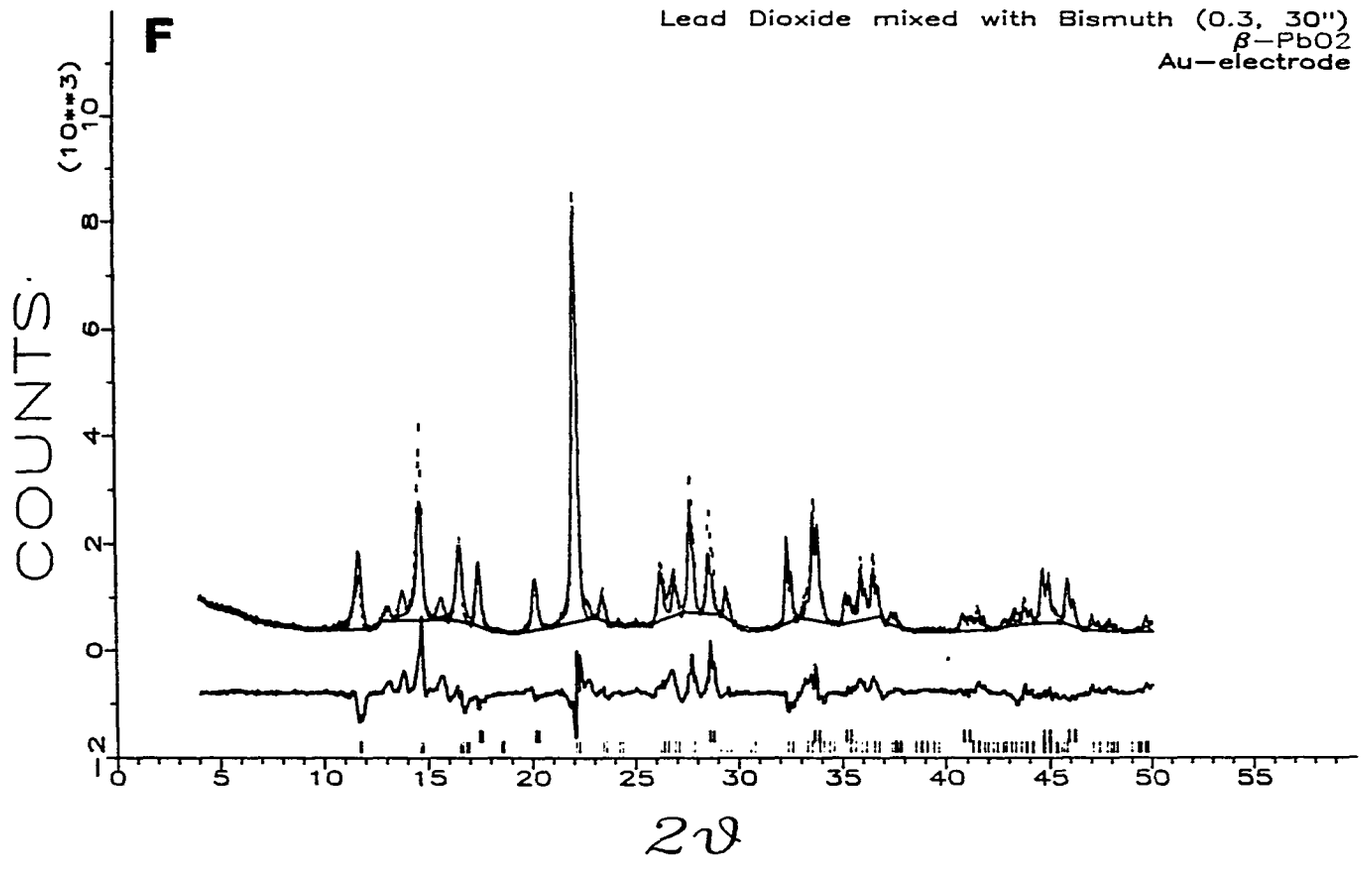

Figure 11 (Continued)

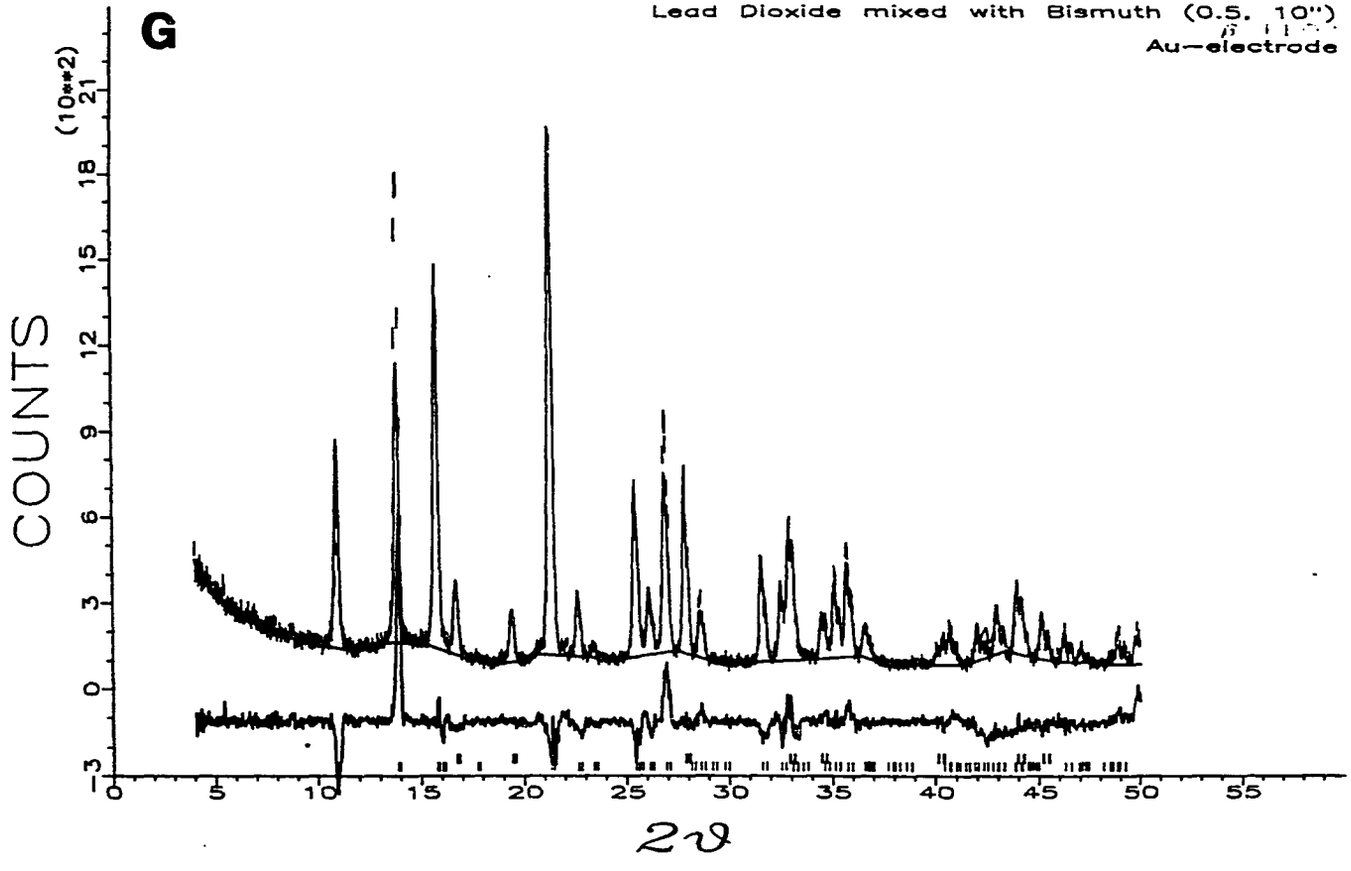

Figure 11 (Continued)

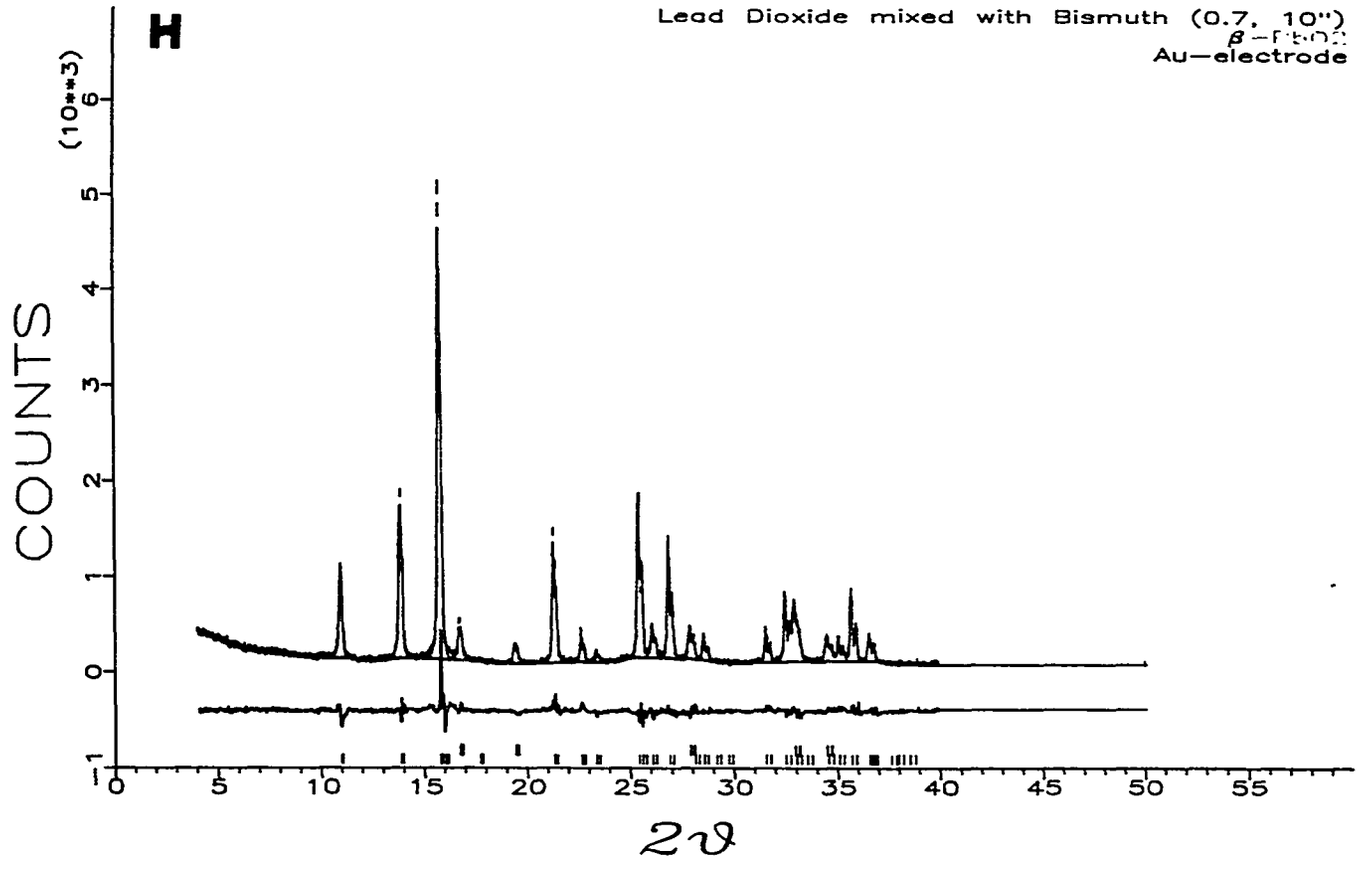

Figure 11 (Continued)

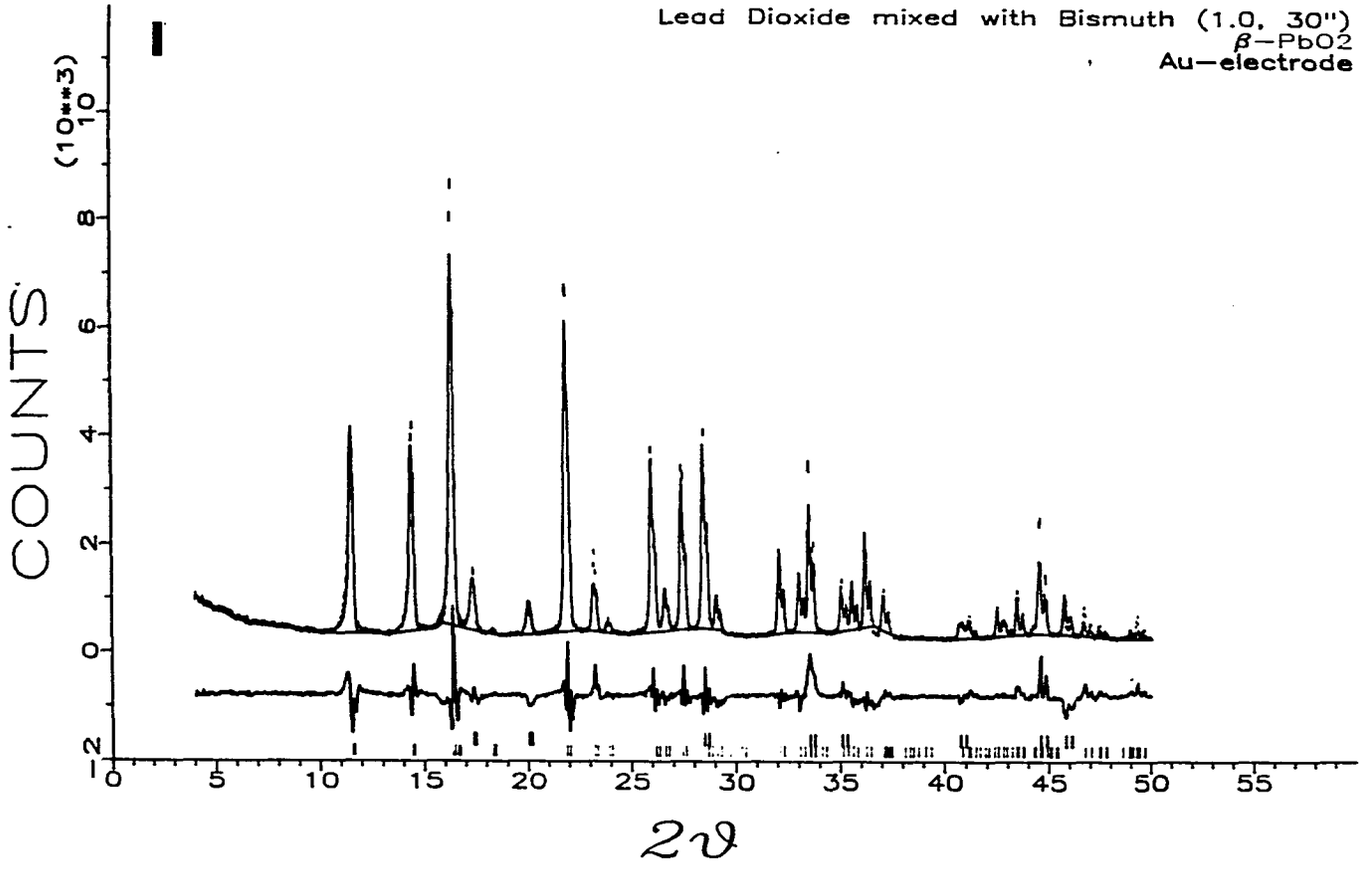

Figure 11 (Continued)

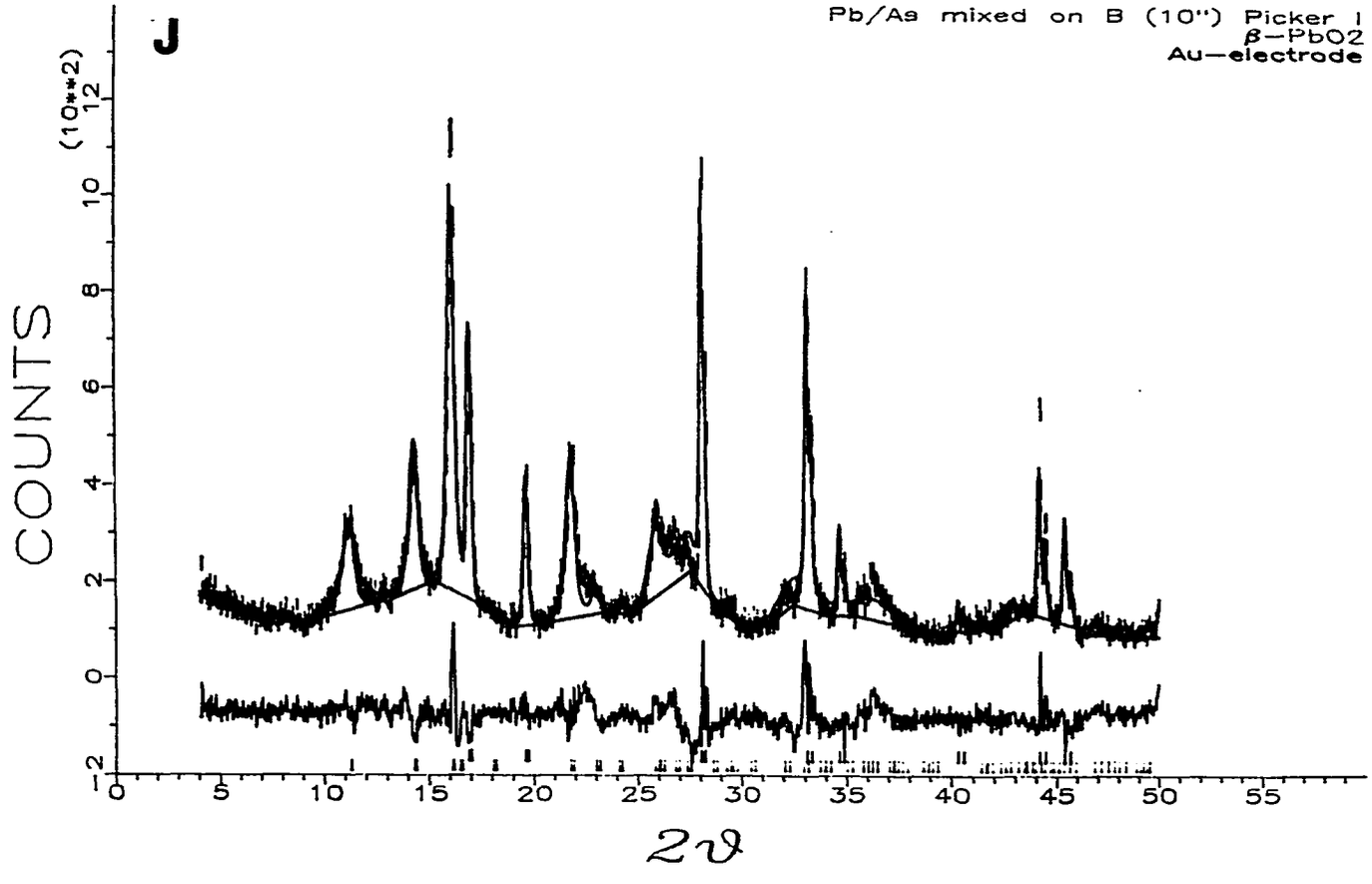

Figure 11 (Continued)

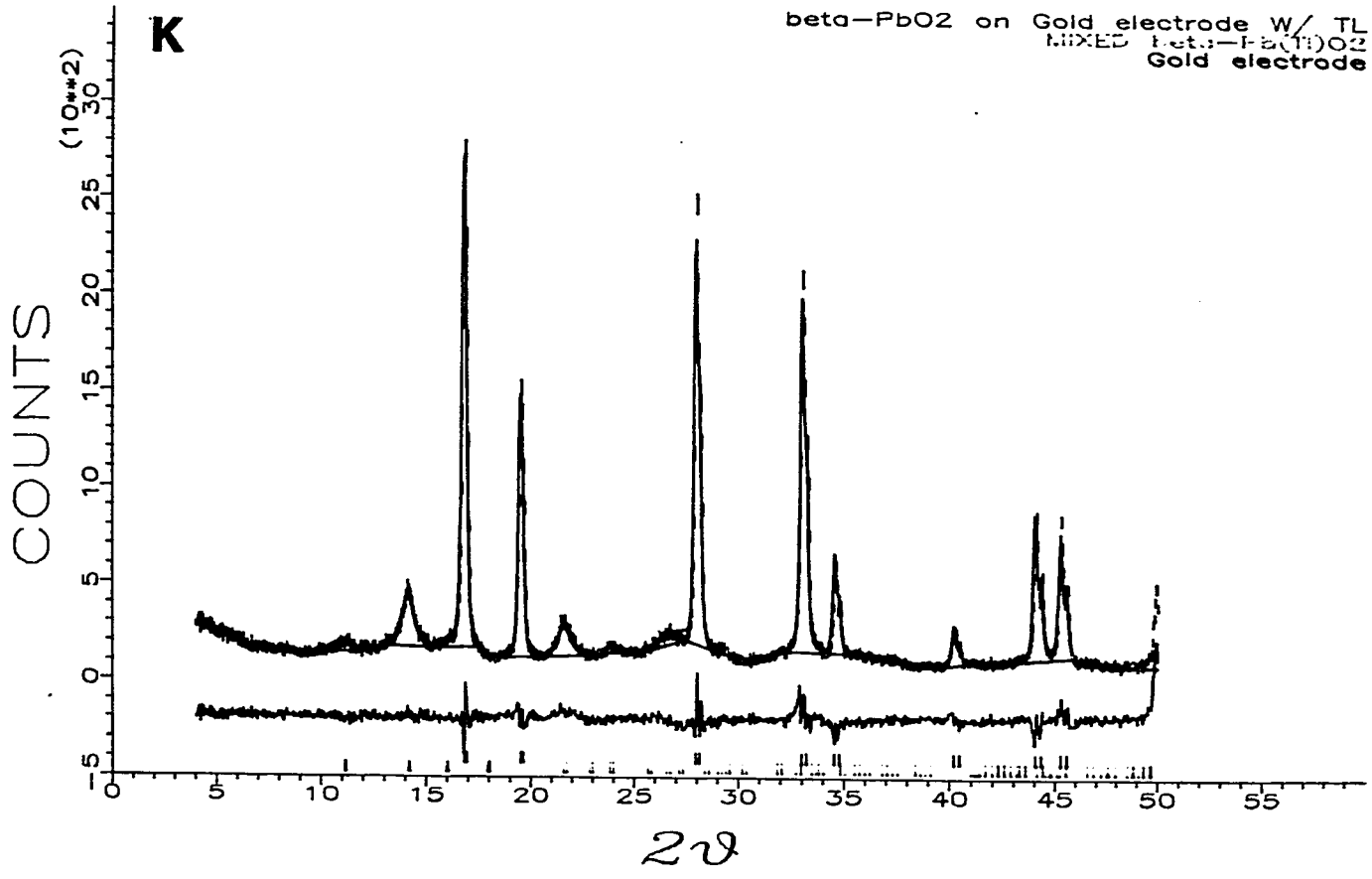

Figure 11 (Continued)

pentavalent, the volume must decrease as Bi concentration increases. Since this is not the case, some fraction of the Bi in the lattice must be in trivalent state. For rutile structures, an empirical relationship between unit cell volume, V, and the cationic radius, r, holds, normally:

$$V = 41.8987 + 88.2806 \cdot r^3$$

This r is an average cationic radius and can be decomposed as follows:

$$r^3 = (1-x) \cdot r_{Pb}{}^{4+3} + x \cdot [(1-y) \cdot r_{Bi}{}^{3+3} + y \cdot r_{Bi}{}^{5+3}]$$

where x is the total Bi concentration in the electrode and y is the mole fraction of Bi in 5+ form defined by $y = [Bi^{5+}]/([Bi^{5+}]+[Bi^{3+}])$. Since the former can be estimated from X-ray fluorescence analyses on the electrodes (Figure 12), the latter can be easily calculated via:

$$y = \frac{r_{Bi}{}^{3+3} - [r^3 - (1-x) \cdot r_{Pb}{}^{4+3}]/x}{r_{Bi}{}^{3+3} - r_{Bi}{}^{5+3}}$$

The result is shown in the last column of Table 3. Interestingly, y values are within 0.86 - 0.89 for most of the samples except for the electrode of [Bi]/[Pb] = 0.1 (At this concentration, the calculation seems to indicate

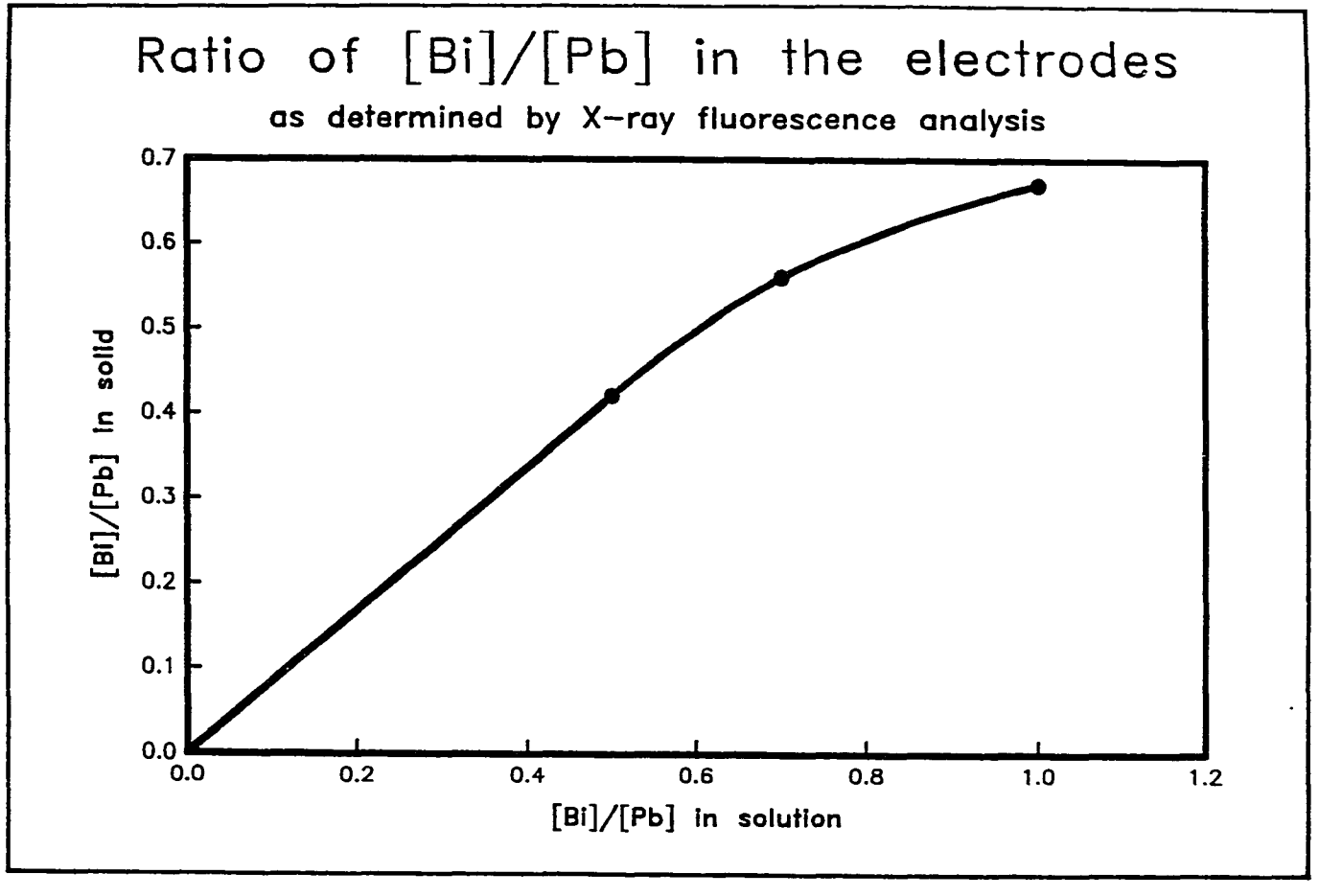

Figure 12. Plots of the ratio [Bi]/[Pb] in the electrodes vs. that in the deposition solution. The three circles were determined by X-ray fluorescence analyses and the result was extended to the origin

virtually no Bi^{3+} present in the electrode. If this is true, it give rise to the radius for Bi^{5+} ion as 0.75 A.).

Similar results were obtained by electrochemical measurements. Amperometric studies indicated that Bi^{3+} was oxidized with n = ca. 1.5 ± 0.2 simultaneously with electrodeposition in the doped oxide.[4] This number translates into 75% of total Bi being oxidized to Bi^{5+}. It should be noted that the interpretation of the X-ray results is subject to the definition of the cationic radii. Although the actual values do not agree, both X-ray analyses and electrochemical measurements indicated the presence of smaller amounts of Bi^{3+} compared to Bi^{5+} in the lattice.

Preferred orientation

One of the distinct features in the diffraction patterns of the electrode samples compared to those of the powder samples is that the former exhibit relative intensities among reflections different from those of the latter. For example, the 110 (10.5° 2θ) and 011 (14.5 2θ) reflections are the strongest in the powder samples (Figures 11A and 11B), while they are relatively weaker than other peaks such as the 121 (22.3° 2θ) reflection in Figure 11C and the 020 (15.8° 2θ) reflection in Figure 11H. This intensity variation is interpreted in terms of preferred orientation of the crystalline particles along several low index lattice

directions. The most prominent preferred orientation directions are the (121) direction for the electrode samples with zero or low [Bi]/[Pb], and the (020) direction for those with high [Bi]/[Pb]. However, both directions were included in the calculation using Eq. (3), and their associated preferred orientation parameters were determined as listed in Table 4. The relative abundance of these two directions is measured by b_1 and b_2. The value of b_1 increases as x increases, reaching a maximum at x = 0.7 and decreasing after that. On the other hand, the value of b_2 decreases as x increses. At x = 0.7, there is virtually no preferred orientation along the (121) direction. Instead, the secondary direction was chosen as (011) in this case.

Another way of depicting this preferred orientation effect is to represent the intensity of each reflection of the electrode samples in units of its intensity of the randomly oriented powder. Although directly measuring integrated intensity for each reflection is not feasible due to the overlap with neighboring reflections, its indirect estimation is easily accomplished using the Rietveld program. By using this integrated intensity, not the peak height, in the comparison, one can eliminate potential problems associated with the peak overlap and variations in both sample size (Eq. 2) and peak width. Figure 13 shows the variation in the integrated intensities of 110, 011, 020, 121 reflections, corrected for the temperature factor, as

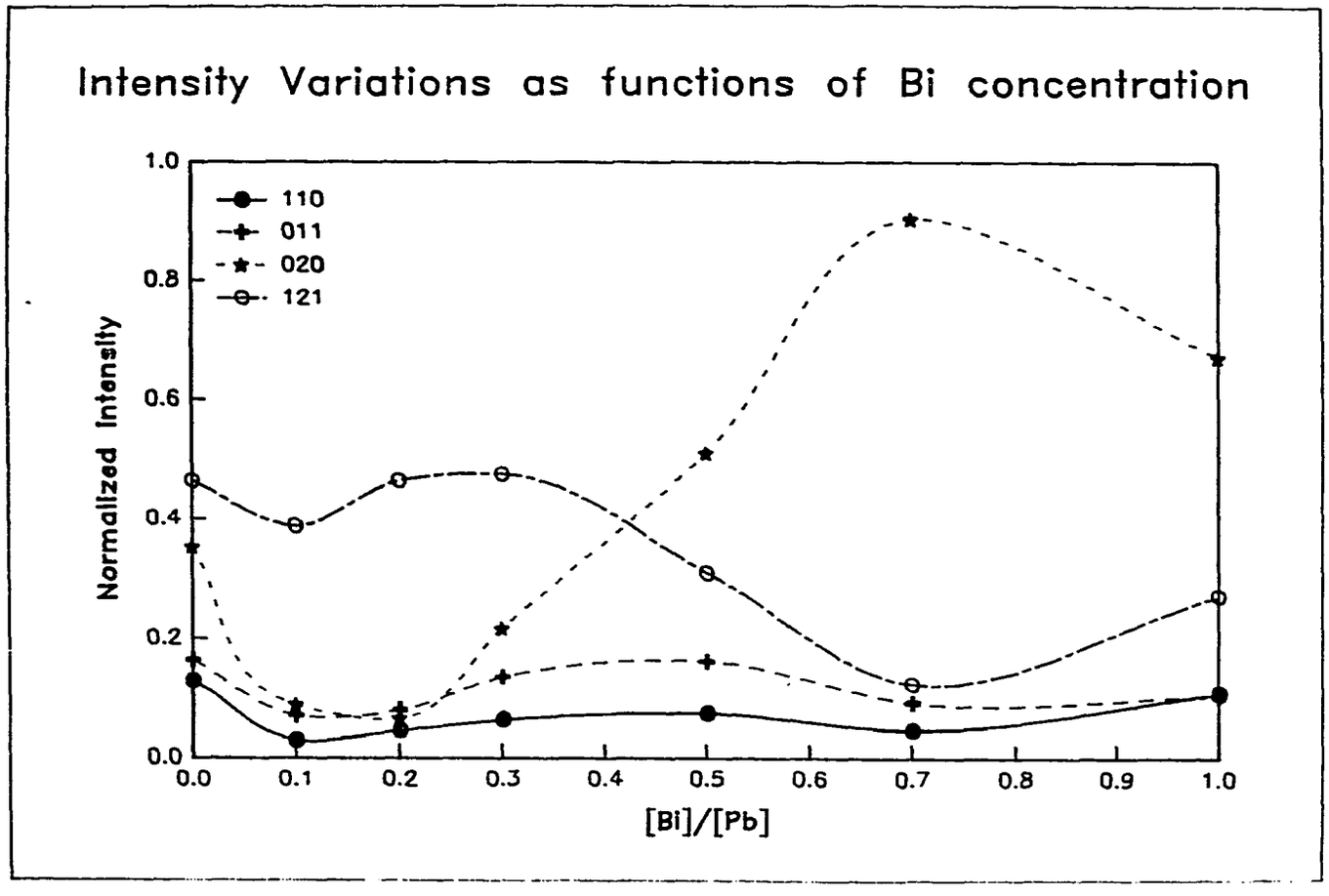

Figure 13. Plots of integrated intensities of low angle reflections vs. [Bi]/[Pb]. The intensities are scaled with respect to the expected intensities of the random powder sample. The legends represent the reflection indices

functions of the [Bi]/[Pb] concentration ratio. Clearly, the preferred orientation along (020) direction is maximal when [Bi]/[Pb] = 0.7, whereas it is minimal along (121).

It should be noted, however, that our model does not fully explain the complexity of the preferred orientation occurring in these Bi/Pb mixed oxides, as indicated by relatively large residuals of the pattern fitting. The real orientation function is too complicated to be represented by a sum of two Gaussians as in our model.

Peak width

There are two factors affecting diffraction peak widths: one is due to small particle size and the other is of an instrumental nature. When the size of the indivisual crystals is less than about 0.1 μm (1000 A), the peak width is inversely proportional to the particle size, as given by the Scherrer formula:[17]

$$B = \frac{0.9\lambda}{t \cdot \cos\theta} , \qquad (4)$$

where B is the breadth in radians, λ the wavelength, t the particle size, and θ the Bragg angle. The instrumental broadening is due to such causes as the divergence of the incident beam and the monochromator mosaicity. This broadening exists even when the crystallite size exceeds 1000

A, while the particle size broadening essentially becomes zero beyond this limit. The total breadth, B_T, can be expressed in terms of the particle size broadening, B_P, and the instrumental broadening, B_I:

$$B_T^n = B_P^n + B_I^n$$

where n is 1 and 2 for Lorentzian and Gaussian profiles, respectively. By calibrating the instrument using a standard sample with a large particle size (> 1000 A), one can, in principle, extract B_P and thus evaluate the particle size using Eq. 4.

Although the instrumental broadening term has not been subtracted out, the variation of the particle size of undoped and Bi-doped PbO_2 electrodes can still be discussed, at least qualitatively, since the instrumental contribution is independent of concentration. The peak widths (FWHM) for various concentrations are calculated from the refined U, V, and W parameters, and plotted in Figure 14 as functions of 2θ. It should be noted that the accuracy of the peak widths plotted in Figure 14 depends on the quality of the fitting. For example, the diffraction peak above 30° 2θ are either generally weaker or more likely contaminated by the strong reflections from the Au subtrate than the low angle reflections. The width decreases as [Bi]/[Pb] increases, with minimum at [Bi]/[Pb] = 0.7. Scanning electron

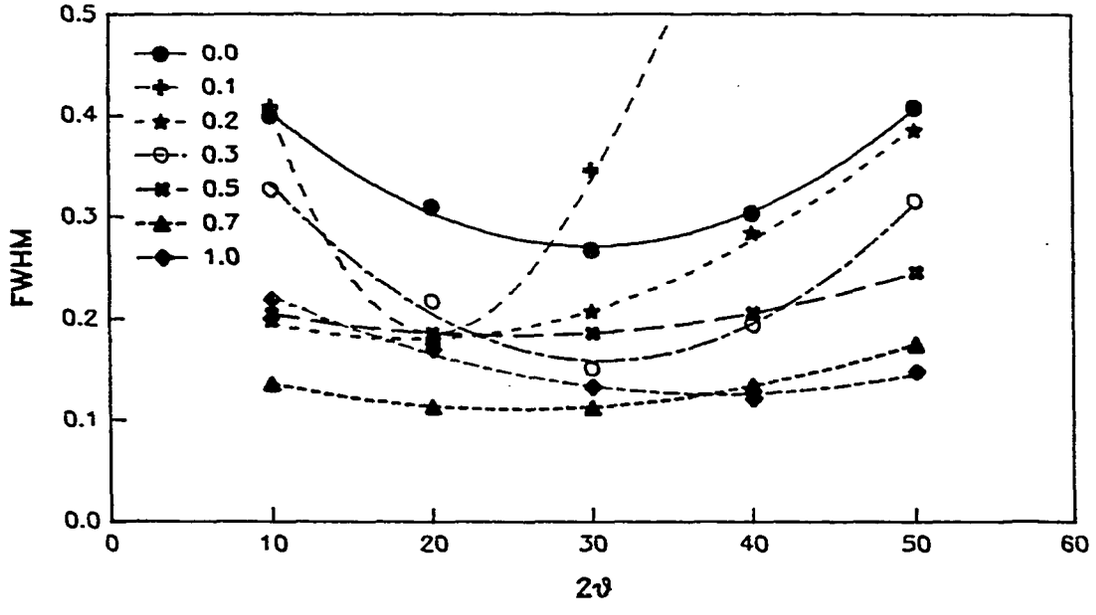

Figure 14. Plots of full-width-at-half-maxima (FWHM) vs. 2θ for the β-PbO_2 phase in the electrode samples. The [Bi]/[Pb] values are given as legend

micrographs (SEM) are shown in Figure 15 for an undoped electrode and a Bi-doped electrodes of [Bi]/[Pb] = 1.0.[4] Clearly, the doped electrode shows larger particle size. It can be argued that the crystalline particle size increases until [Bi]/[Pb] reaches 0.7, and then starts to decreases as more Bi is doped.

We believe there is a correlation between this particle size and the preferred orientation discussed above. We do not know exactly why this is so. However, some speculation is possible. If one assumes the β-PbO_2 lattice is distorted due to some type of lattice defect (e.g., metal or oxygen deficiency), doping metals of different sizes into the lattice will ease the distortion, causing the growth of larger particle sizes, and thus enhancing preferred orientation. Of the two different types of Bi, namely Bi^{3+} and Bi^{5+}, probably the smaller one, Bi^{5+}, plays the prominent role in relieving this distortion. When larger Tl^{3+} (0.885 A) is used as dopant, the material is more difficult to deposit, the peaks are broader, and the preferred orientation is now along (011). On the other hand, if the smaller As^{5+} (0.46 A) is used as dopant, the preferred orientation is again along (020). The particle size, however, is smaller in this case, probably because As^{5+} is too small compared to Pb^{4+}.

Examination of the diffraction backgrounds leads to similar conclusions. In general, wiggles in diffraction

Figure 15. The scanning electron micrographs of undoped (left) and Bi-doped electrodes with [Bi]/[Pb] = 1.0 (right). The upper pictures have lower magnification than the lower ones


PB02BI02.5
5UM


PB02BI02.5
2UM

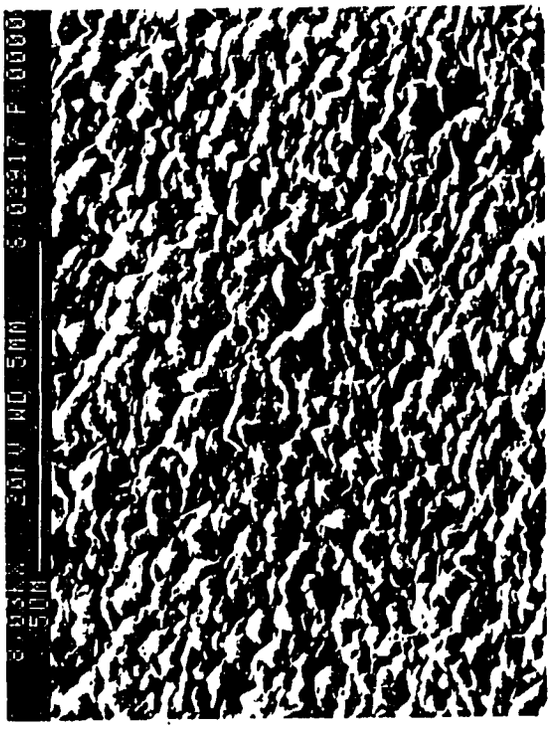

backgrounds are due to scattering from statistical fluctuation of atomic positions around the equilibrium positions. Thermal vibration of atoms and lattice, short range ordering in solid solution and lattice distortion are responsible for these fluctuations. Various techniques[18-20] have been suggested for separation of these effects, but only for rather simple systems. For the undoped and doped PbO_2 eletrodes, the thermal diffuse scattering effect is not expected to vary significantly, since all the data were taken at the room temperature. Typically, the lattice distortion effect gives rise to a slowly varying oscillatory function, whereas the short range order effect cause small distinct peaks at corresponding superlattice peak positions. As shown in Figure 11, the shape of the diffraction patterns for those of with no and low concentration of Bi have backgrounds which have much more pronounced wiggles than for those of Bi/Pb = 0.7 and 1.0. Hence it might be argued that as Bi concentration increases, the existing distortion relieves, particle size grows, and preferred orientation increases along a favorable direction, namely (020).

REFERENCES

1. Jansson, R. Chem. & Eng. News, 1984, 62(47), 43.

2. Johnson, D. C.; Polta, J. A.; Polta, T. Z.; Neuburger, G. G.; Johnson, J.; Tang, A. P-C.; Yeo, I-H.; Baur, J. J. Chem. Soc., Faraday Trans. 1 1986, 82, 1081.

3. Tang, A. P-C.; Johnson, D. C. J. Electrochem. Soc., submitted.

4. Yeo I-H.; Johnson, D. C. J. Electrochem. Soc., submitted.

5. Levich, V. G. "Physicochemical Hydrodynamics"; Prentice Hall: Englewood Cliffs, NJ, 1962; p 75.

6. Hewat, A. W. In "Proceedings of a Symposium on Accuracy in Powder Diffraction"; Block S. and Hubbard, C. R., Ed.; National Bureau of Standards Special Publication 567: Washington, D.C., 1980; p 111, references therein.

7. Young, R. A. In "Proceedings of a Symposium on Accuracy in Powder Diffraction"; Block S. and Hubbard, C. R., Ed.; National Bureau of Standards Special Publication 567: Washington, D.C., 1980; p 143, references therein.

8. D'Antonio P.; Santoro, A. Acta Crystallogr. 1980, B36, 2394.

9. Hill, R. J. Mat. Res. Bull. 1982, 17, 769.

10. Santoro, A.; D'Antonio, P.; Caulder, S. M. J. Electrochem. Soc. 1983, 130(7), 1451.

11. Hill R. J.; Madsen, I. C. J. Electrochem. Soc. 1984, 131(7), 1486.

12. Thanos J. C. G.; Wabner, D. W. J. Electroanal. Chem. 1985, 182, 25.

13. Wiles D. B.; Young, R. A. J. Appl. Crystallogr. 1981, 14, 149.

14. Marquardt, D. W. J. Soc. Indust. Appl. Math. 1963, 11(2), 431.

15. Uda, M.; Sada, Y. J. Solid State Chem. 1983, 46, 121.

16. Shannon, R. D. Acta Crystallogr. 1976, A32, 751.

17. Cullity, B. D. "Elements of X-ray Diffraction", 2nd ed.; Addison-Wesley Publishing Co.: Reading, MA, 1978; p 102.

18. Warren, B. E.; Averbach, B. L.; Roberts, B. W. J. Appl. Phys. 1951, 22(12), 1493.

19. Borie, B. Acta Crystallogr. 1961, 14, 472.

20. Moss, S. C. J. Appl. Phys. 1964, 35(12), 3547.

SECTION II

A STUDY OF X-RAY RADIATION DAMAGE ON A SINGLE CRYSTAL OF BEZENE CHROMIUM TRICARBONYL

INTRODUCTION

Radiation damage effects on materials caused by X-rays, neutrons, electrons, and other particles have been extensively studied especially in conjunction with designing materials sufficiently resistant to the effect of radiations encountered in nulclear reactors. A rich set of studies on this subject of understanding the effect primarily on inorganic solids were reviewed by Gittus.[1] As the laboratory-scale X-ray radiations often induce damages on molecular crystals and thus affect accurate intensity data measurements, systematic studies of the effects on crystallographic parameters are highly desirable.

One of the first systematic studies in this area was by Alemany, Mendiola, Jimenez, and Maurer.[2] They monitored intensity changes in 8 reflections, ranging from strong to weak, of triglycine sulphate as functions of irradiation time. Using an exponential decay model incorporating a parameter relating to the mosaic-block diameter, they were able to model the secondary extinction factor, and subsequently the intensity variations of those reflections.

Murata, Fryer, Baird, and Murata[3] studied radiation damage on crystals of copper hexadecachlorophthalocyanine caused by electron beams. They found such damage to be directional dependent and correlated this with weakening of intermolecular packing interactions.

Another interesting result arose from a recent study by Seiler and Dunitz[4] involving the diffraction study of crystals of 4,5,10,11-tetraoxa-1,2,7,8-tetraazatricyclo[6.4.1.$1^{2,7}$]. They demonstrated that there are some remarkable resemblences between the results of a thermal expansion of and a radiation damage on their crystals. They also noticed that the reduction in intensity was more pronounced for higher angle reflections. However, the damage occurred throughout the data collection period and the intensities were measured shell by shell beginning at the outside of reflection sphere and working inwards, so that reflections belonging to the same angular shell were measured at the same stage of damge.

Here we report results of radiation damage studies on benzene chromium tricarbonyl (BCT), a compound whose structure has been well characterized at both low and room temperatures and by both X-ray[5] and neutron diffractions.[6] The BCT crystals are known to diffract very well and are hard to damage by irradiation. By using a much higher flux of X-ray radiation, we were able to damage the BCT crystals, and yet, since the BCT crystal exhibits essentially no decay during ordinary intensity data collections, complete sets of data could be collected free from crystal decay effects internal to the sets. Via separate refinements, we were able to monitor changes in various structural variables as functions of irradiation dosage.

EXPERIMENTAL SECTION

Pale yellow crystals were grown by sublimation under vacuum and then sealed in a Lindeman glass capillary. A single crystal of BCT was irradiated with Mo radiation from a GE high flux tube operated at 40 kV and 15 mA for nine different periods of 2 days to 2 weeks each. A much higher X-ray flux was obtained than would be experienced under conditions of normal data collection by using unfiltered beams, a wider beam opening (ca. 3 mm), and a short crystal to tube distance (ca. 10 cm). After each irradiation, intensity data were collected using a ω-stepscan (scan range 1.2°, 0.5 sec counting per 0.01° step, 5 sec stationary background measurement at each end of the scan range) over a 2 days period using Mo Kα radiation (λ = 0.70966 A) from a Nonius tube operated at 55 kV and 25 mA. As a general check of conditions, the peak height of a standard reflection was monitored every 50 reflections; no deviation from the initial value greater than 6σ was detected. The diffractometer (DATEX) was equipped with a diffracted-beam graphite monochromator and controlled by a LSI-11 computer which in turn communicated with VAX-11/730. A semi-empirical absortion correction was applied based on an azimuthal scan data (ratios of min/max transmission were 0.81-0.88). After Lorentz and polarization corrections of each data set, the calculations of the structure factors and their associated

standard deviations and the averaging of the redundant data were done in the usual manner. The details of crystallographic data are summarized in Table 1. The unit cell parameters were determined via a least-squares fit to 30 carefully centered high angle reflections; the same reflections were used after each period. After the tenth data collection, the crystal still diffracted now so weakly that not enough reflections could be obtained to ensure meaningful refinement results. (As one can see from Table 1, the number of observed reflections dropped rapidly as irradiation continued.) Each data set was then analyzed via least-squares refinement procedures employing the usual parameters: the scale factor, isotropic secondary extinction coefficient, positional, anisotropic thermal parameters of nonhydrogen atoms, and isotropic thermal parameters of hydrogen atoms, minimizing $\Sigma\omega(|F_o|-|F_c|)^2$, where ω was initially $1/\sigma_F^2$ but at later stages readjusted to reduce systematic variations of $\langle\omega(|F_o|-|F_c|)^2\rangle$ as a function of $\sin\theta$ and of $|F_o|$. The structure and numbering scheme is shown in Figure 1.

Table 1. Summary of crystallographic data

(a) Variation of cell constants

time[a]	a(A)	b(A)	c(A)	β(°)	V(A^3)
0	6.149(1)	11.035(2)	6.570(2)	101.49(2)	436.9(2)
5	6.161(1)	11.048(2)	6.573(2)	101.61(3)	438.3(2)
7	6.160(1)	11.051(2)	6.574(2)	101.57(2)	438.4(2)
15	6.170(2)	11.058(3)	6.581(2)	101.61(3)	439.8(2)
21	6.167(2)	11.059(3)	6.579(2)	101.54(4)	439.6(2)
26	6.171(2)	11.067(3)	6.581(2)	101.58(4)	440.3(2)
33	6.181(2)	11.067(3)	6.576(3)	101.69(4)	440.5(2)
48	6.189(2)	11.079(3)	6.587(2)	101.73(3)	442.2(2)
58	6.193(2)	11.094(3)	6.592(2)	101.82(3)	443.3(2)
69	6.197(3)	11.090(4)	6.613(4)	101.88(6)	444.7(3)

[a]The time is in accumulated irradiation days.

Table 1 (Continued)

(b) Statistics of data reduction and refinement

time	N_{tot}[b]	N_{obs}[c]	N_{ind}[d]	R_{ave}[e]	R_F[f]	R_w[g]	R_I[h]
0	1964	1585	679	0.016	0.028	0.028	0.048
5	1985	1522	658	0.024	0.030	0.035	0.039
7	2010	1521	662	0.023	0.030	0.032	0.037
15	1999	1359	615	0.027	0.034	0.034	0.037
21	1987	1380	608	0.028	0.035	0.037	0.043
26	1997	1300	584	0.028	0.035	0.038	0.042
33	2001	1344	585	0.017	0.031	0.035	0.042
48	1983	1090	496	0.024	0.036	0.033	0.064
58	1949	871	377	0.018	0.044	0.038	0.073
69	1164	735	328	0.021	0.045	0.048	0.079

[b]Number of reflections with preliminary counts above backgrounds.

[c]Number of reflections with $F \geq 3\sigma_F$.

[d]Number of unique reflections.

[e]$R_{ave} \equiv \Sigma|I-\langle I\rangle|/\Sigma I$, where sum is over the observed reflections.

[f]$R_F \equiv \Sigma||F_o|-|F_c||/\Sigma|F_o|$.

[g]$R_w \equiv (\Sigma\omega(|F_o|-|F_c|)^2/\Sigma\omega|F_o|^2)^{1/2}$.

[h]$R_I \equiv \Sigma||F_o|^2-|F_c|^2|/\Sigma|F_o|^2$.

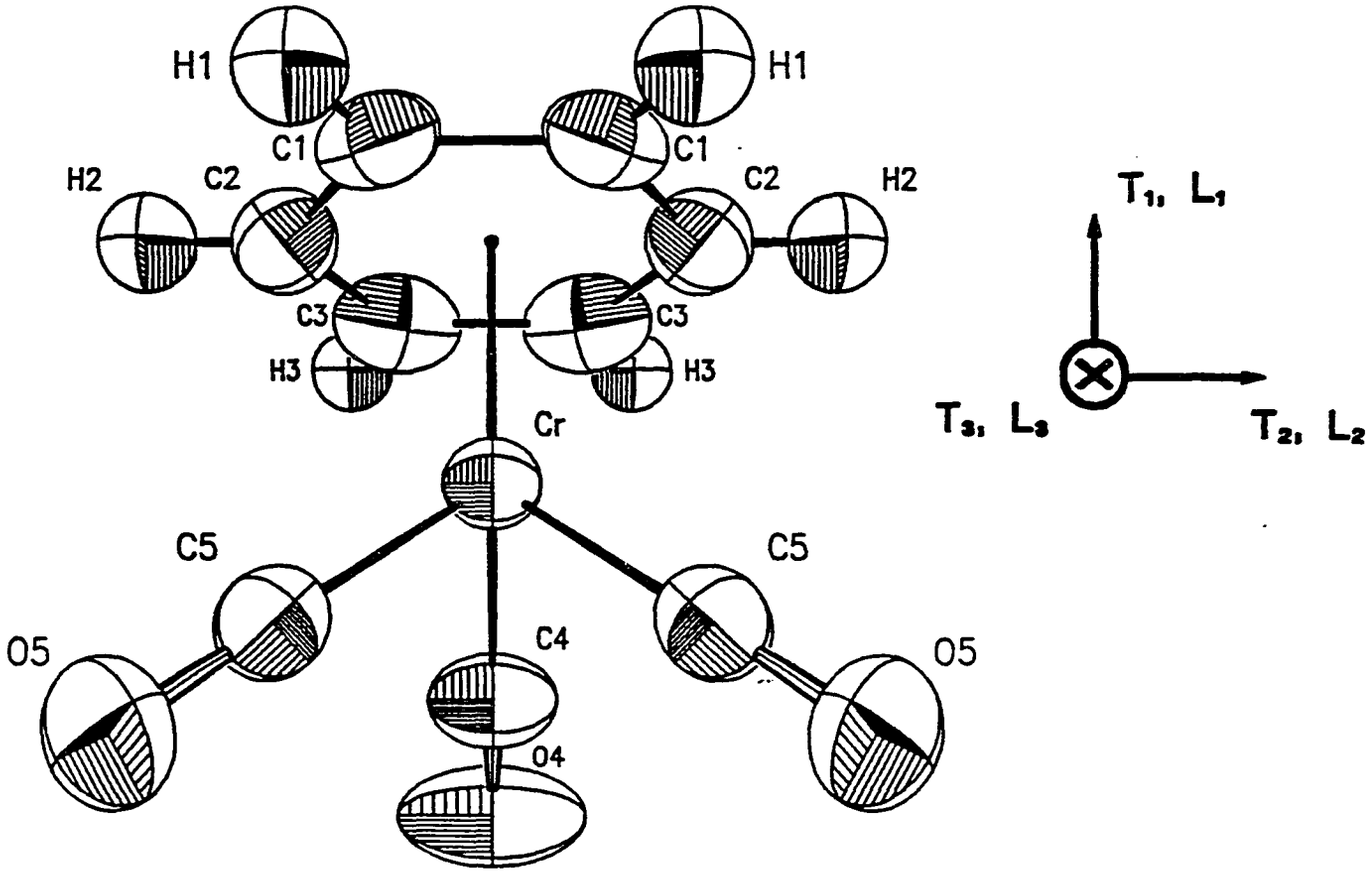

Figure 1. An ORTEP drawing of benzene chromium tricarbonyl, BCT. The monoclinic b axis is parallel to the horizontal direction of the picture. The orthogonal axes used in the TLS analysis are shown on the right

RESULTS

Changes in the various structural parameters were observed. Those of the unit cell parameters are shown in Figure 2, and the scale factor and isotropic secondary extinction coefficient are in Figure 3. The positional parameters are listed in Table 2.

The unit cell parameters increased as irradiation continued. Similar results were obtained by Seiler and Dunitz.[4] Unlike theirs, out results appear to indicate "anisotropic" variation of a, b, and c, especially below 33 days. After that it undergoes a rather isotropic expansion. The last data point has large deviations from the rest of the data primarily because of the much larger errors associated with tuning already too weak reflections.

Decreases in the scale factor, as one might expect, and the secondary extinction coefficient were noticed as irradiation continued. Decreases in the secondary extinction effect have been observed by Alemany, Mendiola, Jimenez, and Maurer.[2] Notice that after 33 days, the secondary extinction effect has essentially disappeared, while the other parameters keep varying.

The atomic positional parameters appeared to change slightly without significant change in the intramolecular geometry. Selected bond distances are listed in Table 3. Some intermolecular distances increased systematically,

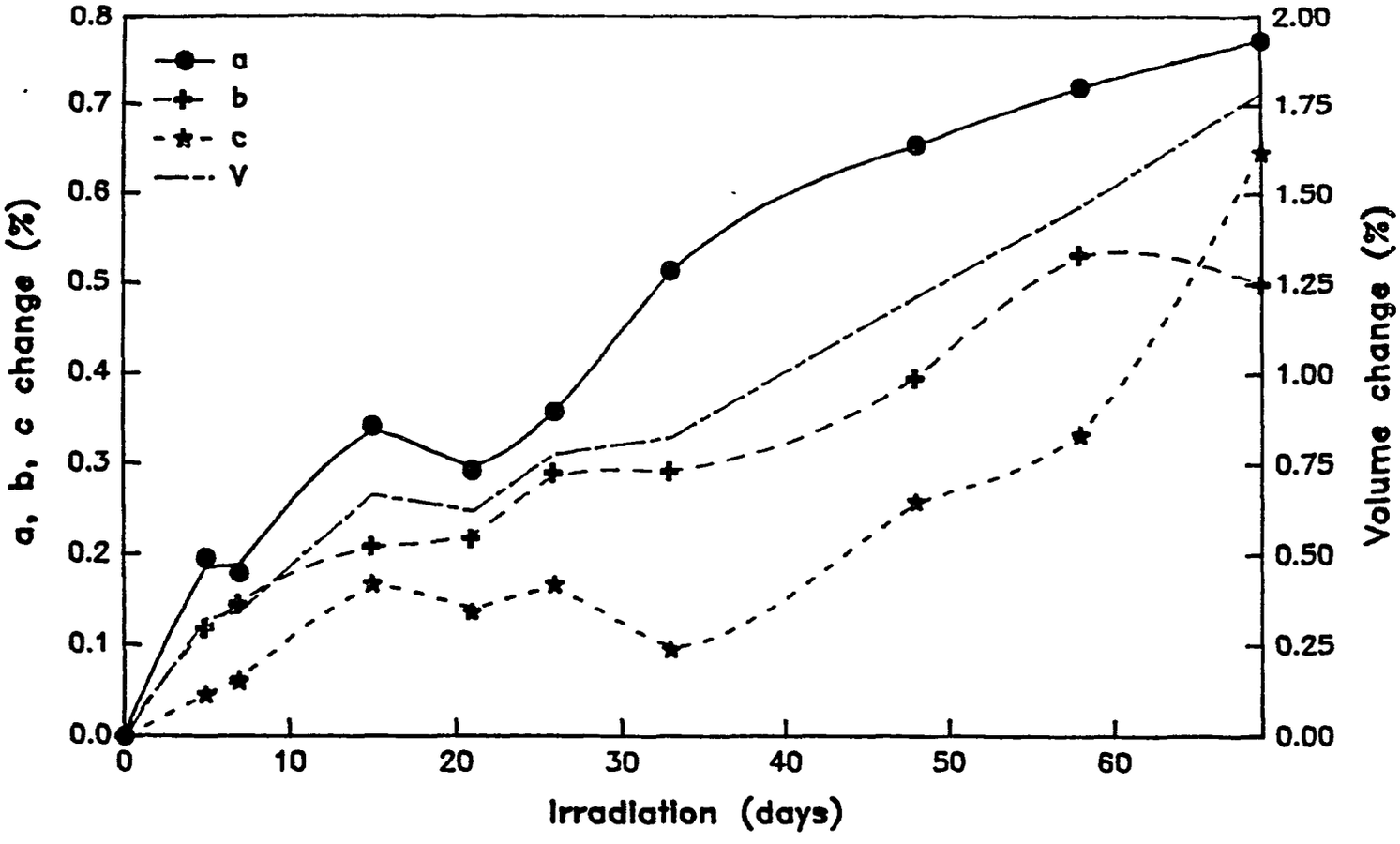

Figure 2. Relative variations of lattice parameters as functions of irradiation time. a (°), b (+), and c (*) refer to the left axis, while V refers to the right axis

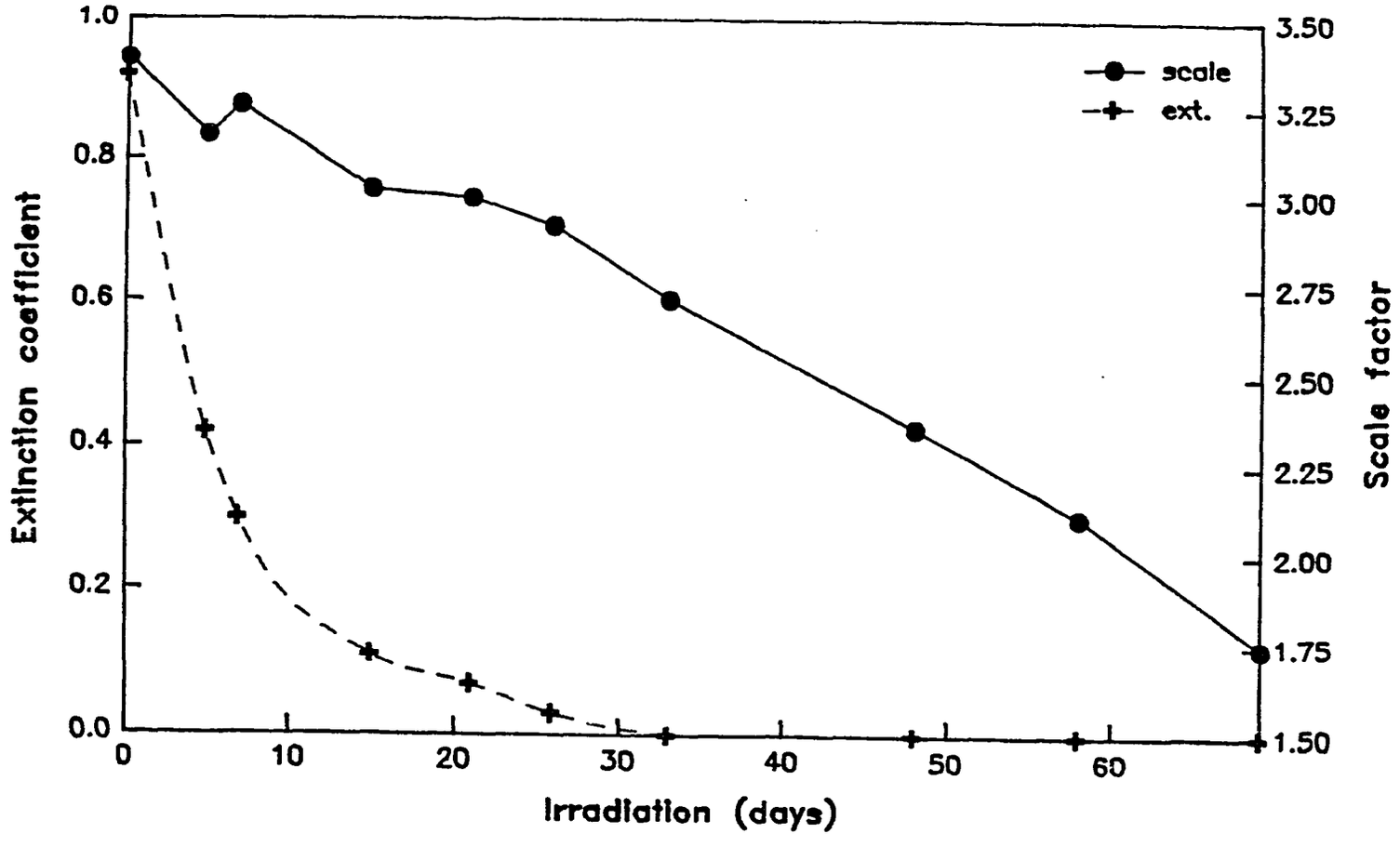

Figure 3. Relative variations of the scale parameter (°, right axis) and the isotropic secondary extinction coefficient (+, left axis) as functions of irradiation time

Table 2. Positional parameters[a] of BCT

time	Cr			Cl		
	x	y	z	x	y	z
0	33178(9)	25000	2245(7)	1806(4)	3125(3)	-2968(3)
5	33143(10)	25000	2247(10)	1808(5)	3121(3)	-2956(5)
7	33135(10)	25000	2246(10)	1816(5)	3117(3)	-2951(4)
15	33080(12)	25000	2234(11)	1803(7)	3118(3)	-2954(5)
21	33088(13)	25000	2232(12)	1803(7)	3116(4)	-2948(6)
26	33080(14)	25000	2239(13)	1800(7)	3120(4)	-2954(6)
33	33060(13)	25000	2219(12)	1798(6)	3118(3)	-2949(5)
48	33054(17)	25000	2180(17)	1791(8)	3111(5)	-2951(7)
58	33026(23)	25000	2133(24)	1794(11)	3117(7)	-2958(10)
69	33012(26)	25000	2179(28)	1788(17)	3112(8)	-2940(15)

[a]Cr positions are multiplied by 10^5, whereas others are by 10^4.

Table 2 (Continued)

time	C2			C3		
	x	y	z	x	y	z
0	3786(5)	3758(3)	-2271(4)	5744(5)	3135(3)	-1593(4)
5	3786(7)	3748(4)	-2268(5)	5733(6)	3128(4)	-1596(5)
7	3778(6)	3747(3)	-2270(5)	5730(6)	3132(4)	-1595(5)
15	3763(8)	3745(4)	-2272(6)	5718(7)	3134(4)	-1594(6)
21	3766(8)	3749(4)	-2271(6)	5721(7)	3133(4)	-1595(7)
26	3760(8)	3750(4)	-2274(6)	5713(7)	3134(5)	-1601(7)
33	3760(7)	3756(4)	-2270(6)	5716(6)	3132(4)	-1591(6)
48	3758(10)	3739(7)	-2274(9)	5685(11)	3117(6)	-1604(8)
58	3756(13)	3735(8)	-2282(12)	5704(12)	3111(7)	-1601(11)
69	3750(16)	3749(10)	-2263(14)	5686(15)	3114(8)	-1591(15)

Table 2 (Continued)

time	C4			C5		
	x	y	z	x	y	z
0	5508(6)	2500	2559(5)	1834(4)	3636(2)	1452(3)
5	5497(7)	2500	2556(7)	1841(5)	3633(3)	1448(5)
7	5495(7)	2500	2549(7)	1836(5)	3634(3)	1442(5)
15	5483(8)	2500	2540(8)	1838(6)	3633(3)	1443(5)
21	5483(9)	2500	2532(9)	1842(6)	3630(4)	1442(6)
26	5487(9)	2500	2544(9)	1846(7)	3635(4)	1448(6)
33	5490(8)	2500	2540(8)	1842(6)	3628(3)	1444(5)
48	5494(11)	2500	2552(11)	1837(8)	3630(5)	1437(8)
58	5504(13)	2500	2514(16)	1814(11)	3619(6)	1437(10)
69	5511(18)	2500	2530(21)	1829(14)	3620(8)	1429(13)

Table 2 (Continued)

time	O4			O5		
	x	y	z	x	y	z
0	6918(6)	2500	3994(5)	898(5)	4334(2)	2256(3)
5	6914(6)	2500	3998(6)	902(5)	4331(3)	2253(4)
7	6906(6)	2500	3998(5)	902(5)	4329(2)	2252(4)
15	6888(7)	2500	3987(6)	908(5)	4330(3)	2247(4)
21	6893(7)	2500	3986(7)	910(5)	4327(3)	2244(5)
26	6890(7)	2500	3986(7)	909(6)	4330(3)	2247(5)
33	6892(7)	2500	3980(6)	909(5)	4329(3)	2245(4)
48	6891(9)	2500	3972(9)	911(7)	4333(4)	2246(6)
58	6887(12)	2500	3969(12)	923(9)	4326(5)	2249(8)
69	6881(14)	2500	3959(16)	940(11)	4319(6)	2244(10)

Table 3. Nonhydrogen bond distances (A)

(a) Cr-C bond distances

time	Cr-C1	Cr-C2	Cr-C3	Cr-C4	Cr-C5
0	2.228(2)	2.210(3)	2.203(3)	1.829(3)	1.830(2)
5	2.218(3)	2.205(4)	2.203(4)	1.824(3)	1.825(3)
7	2.214(3)	2.204(3)	2.202(3)	1.821(3)	1.825(3)
15	2.218(4)	2.204(4)	2.202(4)	1.817(4)	1.824(3)
21	2.215(4)	2.206(4)	2.202(4)	1.814(4)	1.821(4)
26	2.220(4)	2.208(5)	2.203(4)	1.821(4)	1.825(4)
33	2.213(4)	2.210(4)	2.202(4)	1.820(4)	1.821(3)
48	2.213(5)	2.201(6)	2.190(6)	1.831(5)	1.826(5)
58	2.216(7)	2.203(8)	2.198(7)	1.820(7)	1.829(6)
69	2.213(9)	2.208(10)	2.192(9)	1.831(9)	1.821(8)

Table 3 (Continued)

(b) C-C or C-O bond distances[a]

time	C1-C1′	C1-C2	C2-C3	C3-C3′	C4-O4	C5-O5
0	1.379(3)	1.399(4)	1.381(4)	1.401(4)	1.147(4)	1.150(3)
5	1.371(4)	1.396(5)	1.375(5)	1.387(5)	1.152(4)	1.155(4)
7	1.364(4)	1.389(5)	1.375(5)	1.396(5)	1.154(4)	1.152(4)
15	1.367(5)	1.388(5)	1.376(6)	1.403(6)	1.152(5)	1.152(4)
21	1.363(5)	1.392(6)	1.379(6)	1.400(6)	1.157(5)	1.150(5)
26	1.372(6)	1.390(6)	1.378(6)	1.404(6)	1.149(5)	1.151(5)
33	1.369(5)	1.396(5)	1.385(6)	1.399(6)	1.147(5)	1.155(4)
48	1.354(7)	1.394(8)	1.370(9)	1.368(8)	1.137(7)	1.159(6)
58	1.370(9)	1.387(10)	1.384(10)	1.355(10)	1.148(9)	1.153(8)
69	1.357(13)	1.398(13)	1.383(13)	1.361(13)	1.133(12)	1.148(10)

[a]The primed ones are related to the unprimed by (x,1/2-y,z).

primarily in accord with the cell volume expansion. The chromium-chromium intermolecular distances are listed in Table 4.

The temperature factors also showed systematic increases. Since there are 42 parameters describing the anisotropic thermal motions of the non-hydrogen atoms of this structure, a rigid-body thermal motion analysis (TLS) was attempted as described by Schomaker and Trueblood.[7] The result is listed in Table 5 and shown in Figure 4. The directions of the principal axes of the translational (T_1, T_2, and T_3) and librational (L_1, L_2, and L_3) motions were not significantly different from one period to another. However, their magnitudes generally increased as the irradiation continued. Interestingly, while the magnitude of the libration increases slowly, the translational motions perpendicular to the benzene ring (T_1) and the crystallographic mirror plane (T_2), exhibited the most rapid increase. As one can see from Figures 2 and 4, there are remarkably similar features in the variations of the lattice parameters and of the thermal motions. The variations of T_1 and T_2, just as the lattice parameters, were irregular before the 33 day mark, and became smoothly increasing functions after that point.

Table 4. Cr-Cr intermolecular distances[a] (A)

time	Cr-Cr'	Cr-Cr"
0	6.834(1)	5.921(1)
5	6.841(1)	5.930(1)
7	6.841(1)	5.931(1)
15	6.844(1)	5.938(1)
21	6.844(1)	5.938(1)
26	6.848(1)	5.943(1)
33	6.850(1)	5.945(1)
48	6.858(1)	5.951(1)
58	6.864(2)	5.959(2)
69	6.861(2)	5.959(2)

[a]Cr' and Cr" are related to Cr at (x,y,z) by (-x,1-y,-z) and (1-x,1-y,-z), respectively.

Table 5. Rigid-body thermal motion analysis result. Eigenvalues[a] of the translational motions (T_j) and librational motions (L_j).

time	T_1	T_2	T_3	L_1	L_2	L_3	ΔU_{RMS}
0	.04783	.0473	.02062	.01505	.00348	.00336	.0049
5	.06519	.05544	.02324	.01534	.00363	.00319	.0052
7	.06517	.05734	.02554	.01580	.00357	.00330	.0051
15	.06528	.06301	.03130	.01614	.00358	.00288	.0048
21	.07337	.06082	.03073	.01547	.00362	.00296	.0047
26	.07826	.06242	.02612	.01641	.00339	.00323	.0045
33	.06684	.05623	.02696	.01644	.00349	.00302	.0050
48	.07649	.06162	.02973	.01723	.00357	.00289	.0052
58	.09294	.06968	.03092	.01783	.00255	.00381	.0052
69	.10527	.07718	.02979	.01703	.00223	.00427	.0059

[a]The directions of the eigenvectors corresponding to T_1 and L_1 are almost along the molecular 3-fold axis, T_2 and L_2 along $\underline{b}$ axis, and T_3 and L_3 along the remaining third direction.

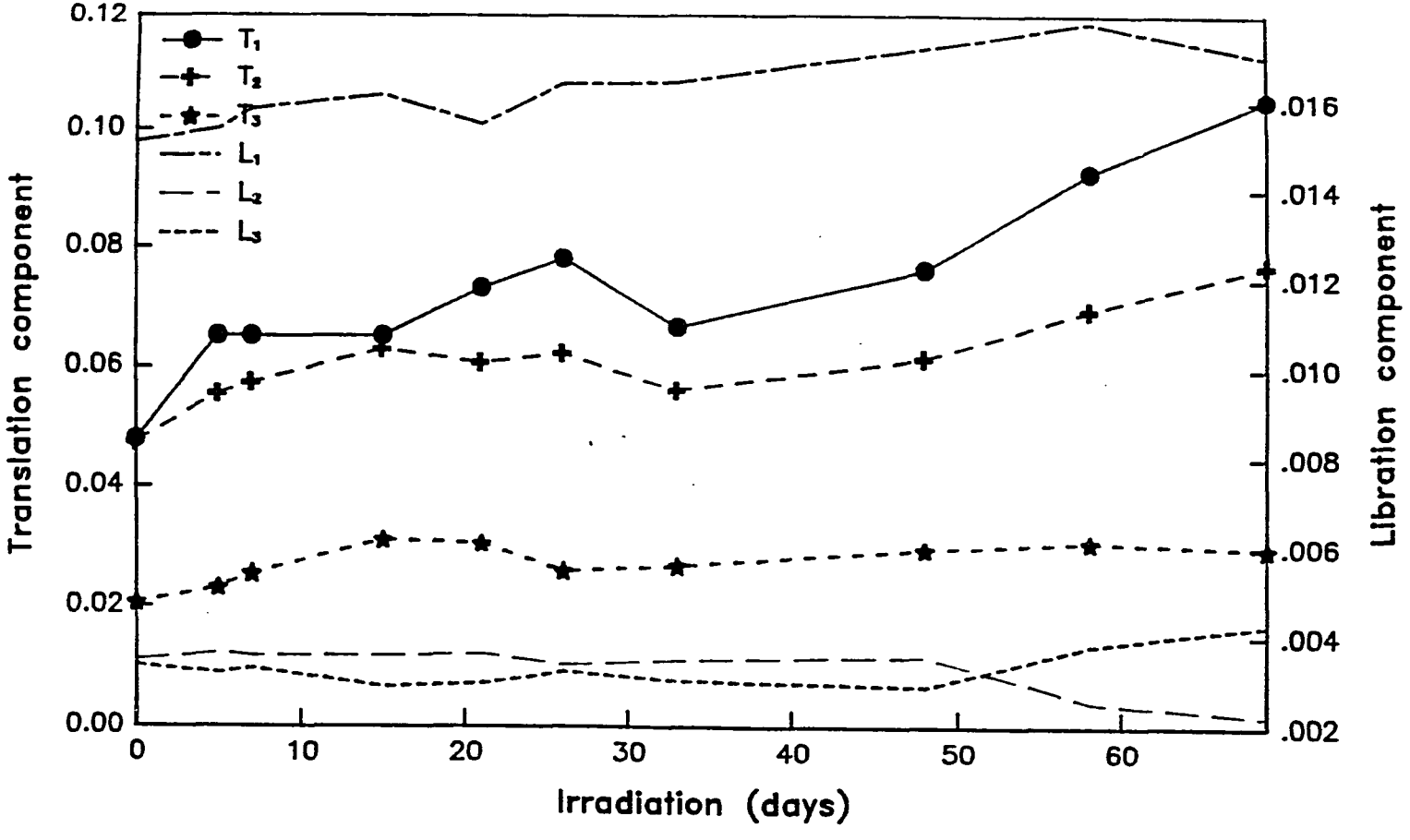

Figure 4. Variations of eigenvalues of T (left axis) and L (right axis) tensors as functions of irradiation time. The eigenvalues refer to the directions of eigenvectors shown in Figure 1

DISCUSSION

The similarities in the variations of the lattice dimensions and the thermal motions may be understood by drawing an analogy between the thermal expansion and the lattice expansion by irradiaiton. For the thermal expansion, the quasi-harmonic theory predicts the lattice expansion rate to be related to the increase of the temperature factors.[8] The theory is based on the argument that the lattice expansion caused by the thermal energy weakens the interatomic forces and thereby increases the thermal motions. One can easily adapt the theory of the thermal expansions of crystals to the case of lattice expansion by irradiation. The systematic changes in the intermolecular distances indeed suggest the weakening of the packing interactions with increased irradiation, and thus the increases in the rigid-body thermal motions. While the increase in T_1 along the molecular axis may be responsible for the loss of crystalline character along that direction, that of T_2 may be responsible for similar effect along the b axis and possibly the breakage of the monoclinic mirror symmetry.

Our radiation damage experiments were performed while the crystal structure maintained its integrity. Interestingly, during the experiment the crystal turned from pale yellow to dark red. Although color centers in inorganic

solids are well known, the cause of the color change in the BCT crystal is not clear.

REFERENCES

1. Gittus, J. "Irradiation Effects in Crystalline Solids"; Applied Science Publishers, Ltd: Essex, England, 1978.

2. Alemany, C.; Mendiola, J.; Jimenez, B.; Maurer, E. Acta Crystallogr. 1973, A29, 423.

3. Murata, Y.; Fryer, J. R.; Baird, T.; Murata, H. Acta Crystallogr. 1977, A33, 198.

4. Seiler, P.; Dunitz, J. D. Aust. J. Phys. 1985, 38, 405.

5. Bailey, M. F.; Dahl, L. F. Inorg. Chem. 1965, 4, 1314.

6. Rees, B.; Coppens, P. Acta Crystallogr. 1973, B29, 2515.

7. Schomaker, V.; Trueblood, K. N. Acta Crystallogr. 1968, B24, 63.

8. Willis, B. T. M.; Pryor, A. W. "Thermal Vibrations in Crystallography"; Cambridge University Press: London, England, 1975.

SECTION III

CRYSTAL AND MOLECULAR STRUCTURES OF SELECTED ORGANOMETALLIC COMPOUNDS CONTAINING SULFUR ATOM

INTRODUCTION

One of the most important developments in organometallic chemistry has been the discovery of carbene and carbyne complexes. The growth of carbene and carbyne chemistry has been partially sparked by interest in olefin and acetylene metatheses and Fischer-Tropsch synthesis in which metal carbenes and carbynes are postulated as key intermediates. Another field of interest in orgnometallic chemistry is that of thiocarbonyls; the similarity of carbon monosulfide (CS) to CO has stimulated much interest in the synthesis and reactivity of CS complexes.

The following is a reaction scheme undertaken by Dr. Angelici's group at Iowa State University.[1]

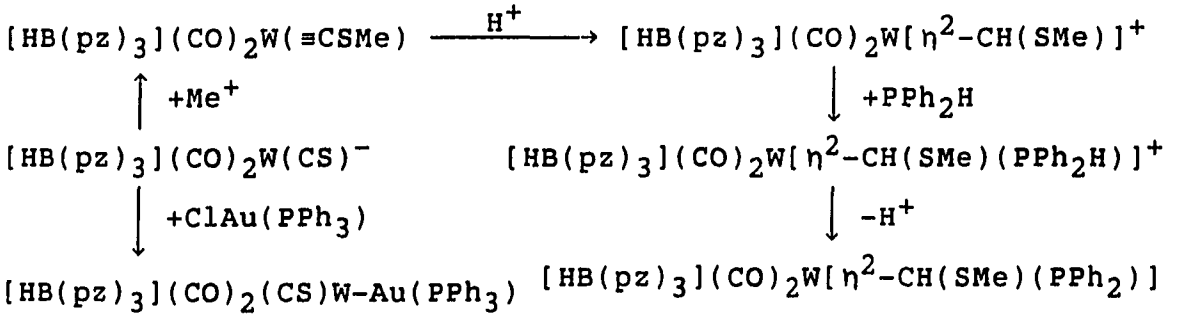

Methylation of a thiocarbonyl compound, $[HB(pz)_3]W(CO)_2(CS)^-$, where pz represent pyrazolyl ring, yields a thiocarbyne compound, $[HB(pz)_3]W(CO)_2(\equiv CSMe)$. Upon protonation, the

thiocarbyne complex transformed into a η^2-thiocarbene complex, $[HB(pz)_3](CO)_2W[\eta^2\text{-}CH(SMe)]^+$, in which the carbene ligands is bonded to the metal through both the C and S atoms. The C(carbene) atom in transition-metal carbene complexes is frequently the site of attack by a variety of nucleophiles. Phosphines are among the nucleophiles which react in this manner. $[HB(pz)_3](CO)_2W[\eta^2\text{-}CH(SMe)]^+$ reacts at room temperature with phosphorus donors to give the adducts $[HB(pz)_3](CO)_2W[\eta^2\text{-}CH(SMe)L]^+$, where L = PPh_3, PEt_3, $P(OMe)_3$, and PPh_2H. Deprotonation of $[HB(pz)_3](CO)_2W[\eta^2\text{-}CH(SMe)(PPh_2H)^+$ gave a neutral species, $[HB(pz)_3](CO)_2W[\eta^2\text{-}CH(SMe)(PPh_2)]$.

Terminal CS groups in electron-rich complexes form adducts at the S with Lewis acids, e.g., $(diphos)_2(CO)W(CSHgCl_2)$,[2] and are also alkylated at the CS sulfur atom, e.g., $[HB(pz)_3](CO)_2W(\equiv CSR)$.[3] On the other hand, certain electrophiles add to the metal center as in the reactions of $CpW(CO)_2(CS)^-$ with HgI_2, $ClSnPh_3$, and $ClPbPh_3$.[4] In the reactions of $[HB(pz)_3](CO)_2W(CS)^-$ and $ClAu(PR_3)$, the $Au(PR_3)$ moiety adds to the W, as is found in other heterobimetallic Au complexes, e.g., $Cp(CO)_3W\text{-}Au(PPh_3)$,[5] $(CO)_4[P(OPh)_3]Mn\text{-}Au(PPh_3)$,[6] $(CO)_4Co\text{-}Au(PPh_3)$,[7] $(\eta^3\text{-}C_3H_5)(CO)_3FeAu(PPh_3)$.[8] The thiocarbonyl and one of the two carbonyl groups have semibridging interactions with the W and Au - the first examples of semibridging CS ligand.

This research involved X-ray structure determinations of several key compounds in the diagram above, and was critical to understanding the chemistry of the complexes. The crystal and molecular structure determinations were undertaken on the $CF_3SO_3^-$ salt of $[HB(pz)_3](CO)_2W[\eta^2\text{-}CH(SMe)]^+$ to confirm the presence of the η^2-thiocarbene ligand, and on $[HB(pz)_3](CO)_2W[\eta^2\text{-}CH(SMe)(PPh_2)]$ to ensure that the ligand $[CH(SMe)(PPh_2)]$ is bonded to the tungsten through both the C and S atoms, and to establish the stereochemistry within the ligand. Similarly, the structure determinations of $[HB(pz)_3](CO)_2(CS)W\text{-}Au(PPh_3)$ and $[HB(pz)_3](CO)_2(CS)W\text{-}Au(PMe_3)$ were undertaken to confirm that the W and Au are bonded together and that the CO and CS groups are semibridging.

EXPERIMENTAL SECTION

Crystals of the compounds of suitable sizes for diffraction work were kindly provided by Dr. Angelici's group. Indexing of the crystals involved rotation (Syntex $P2_1$) and oscillation (DATEX) photography, subsequent tuning of 10 to 15 strong reflections whose approximate positions were inferred from the pictures, and reduced cell calculation via an auto-indexing routine. The higher symmetry cells obtained by transforming the reduced cells, were confirmed by examining the axial photographs. Inspection of the axial photographs of the $[HB(pz)_3](CO)_2W[\eta^2\text{-}CH(SMe)(PPh_2)]$ crystal indicated that the crystal was an aggregate of at least three slightly misoriented grains of various sizes. Other crystals of the same compound tried earlier also showed a similar tendency, even to a greater extent. In this case, the orientation matrix for the data collection was determined by centering the strongest in each cluster of reflections, i.e., focusing only the largest grain.

The general procedures for data reduction have been published elsewhere. Details of the data processing and relevant crystallographic data are given in Table 1. Computer programs used in these studies are summarized in reference 9. The atomic scattering factors were those from reference 10, modified for the anomalous dispersions.

Table 1. Crystallographic data and statistics for $[HB(pz)_3](CO)_2W[\eta^2$-$CH(SMe)]\cdot CF_3SO_3$, 1, $[HB(pz)_3](CO)_2W[\eta^2$-$CH(SMe)(PPh_2)]$, 2, $[HB(pz)_3](CO)_2(CS)W$-$Au(PPh_3)$, 3, and $[HB(pz)_3](CO)_2(CS)W$-$Au(PMe_3)$, 4

	1	2	3	4
Formula unit	$C_{14}H_{14}BF_3N_6O_5S_2W$	$C_{25}H_{24}BN_6O_2PSW$	$C_{30}H_{25}AuBN_6O_2PSW$	$C_{15}H_{19}AUBN_6O_2PSW$
M. W.	661.72	698.20	956.23	770.02
Space group	$P2_1/c$	$P\bar{1}$	$P2_1/n$	Pbca
a, A	9.841(2)[a]	11.548(14)	15.062(4)	16.956(3)
b, A	11.379(3)	16.148(7)	18.103(3)	17.173(3)
c, A	21.304(5)	7.682(5)	11.887(2)	15.053(2)
α, °	90	101.67(6)	90	90
β, °	109.16(2)	99.06(7)	103.53(2)	90
γ, °	90	70.49(5)	90	90
V, A^3	2171.1(9)	1316.1(18)	3151.2(12)	4383.4(14)
Z	4	2	4	8
ρ_{calc}, g/cm^3	2.025	1.761	2.015	2.333
crystal size, mm	0.15x0.2x0.2	0.2x0.2x0.15	0.5x0.5x0.45	0.2x0.2x0.2
Diffractometer	Syntex $P2_1$	DATEX	DATEX	Syntex $P2_1$
λ, A	0.71069	0.70966	0.70966	0.71069
μ, cm^{-1}	58.9	48.09	85.12	122.09
T_{min}/T_{max}	0.749	0.701	0.544	0.433

ω scan mode	3°/min	0.5 sec/0.01°	0.5 sec/0.01°	1°/min
scan width	1°	1.2°	1.2°	1.0°
$2\theta_{max}$, °	45	45	50	45
Octants measd.	2	4	2	1
Reflection measd.	3931	4125	5392	3443
Unique observed	2111	2015	3900	1905
Min of I/σ_I	1.5	3	3	3
R, %	7.2	8.8	3.1	5.2
Rw, %	5.0	10.8	3.8	6.2
Extinction coef.	——	——	$0.259(22)\times10^4$	$0.070(19)\times10^4$

[a]For $[HB(pz)_3](CO)_2W[\eta^2\text{-}CH(SMe)]\cdot CF_3SO_3$, data collection was done at -40°C to reduce X-ray radiation damages; for others, it was done at room temperature.

The structures were determined using Patterson and electron density function calculations. The positional and anisotropic thermal parameters of most of the non-hydrogen atoms were refined. A few of the non-hydrogen atoms were refined isotropically: C(12), O(A-E), and F(A-F) of $[HB(pz)_3](CO)_2W[\eta^2\text{-}CH(SMe)]\cdot CF_3SO_3$, and C(1-4), C(53), and N(21) of $[HB(pz)_3](CO)_2W[\eta^2\text{-}CH(SMe)(PPh_2)]$, because of difficulties in assigning physically meaningful anisotropic temperature factors. The function minimized was $\Sigma\omega(|F_o|-|F_c|)^2$, where $\omega = 1/\sigma_F{}^2$. Hydrogen atoms were included in the structure factor calculations at their geometrically ideal positions with isotropic temperature factors but not refined. The anion, $CF_3SO_3^-$, of $[HB(pz)_3](CO)_2W[\eta^2\text{-}CH(SMe)]\cdot CF_3SO_3$ exhibited disorder of two-fold variety around the C(S)-S axis, in the O and F positions. The multiplicity factors of these atoms were refined. In the last stage of the refinement of $[HB(pz)_3](CO)_2W[\eta^2\text{-}CH(SMe)(PPh_2)]$, 15 reflections were noticed to have somewhat larger $|F_o|$ than $|F_c|$, due apparently to the poor crystal quality, and were excluded.

The final atomic positional parameters are listed in Tables 2 - 5, whereas the anisotropic thermal parameters are listed in Tables 6 - 9.

Table 2. The positional parameters[a] ($\times 10^4$) and U_{iso}[b] ($\times 10^3$) for $[HB(pz)_3](CO)_2W[\eta^2\text{-}CH(SMe)]\cdot CF_3SO_3$

atom	x	y	z	U_{iso}
W	6649(1)	5696(1)	3250(0)	29(0)
S(1)	5114(7)	7450(5)	3277(3)	52(2)
C(1)	5701(22)	5628(24)	2244(11)	44(9)
O(1)	5107(16)	5577(16)	1687(7)	60(6)
C(2)	8705(27)	6018(18)	3137(12)	44(10)
O(2)	9817(18)	6136(15)	3089(7)	62(7)
C(3)	6850(24)	7378(17)	3181(12)	47(9)
C(4)	5464(26)	7950(23)	4137(12)	72(11)
N(1)	7593(18)	5486(16)	4339(8)	33(7)
C(11)	8519(20)	6184(19)	4838(11)	40(9)
C(12)	8806(19)	5639(23)	5444(10)	36(5)
C(13)	8082(21)	4599(18)	5315(9)	34(9)
N(11)	7350(17)	4510(15)	4648(8)	33(6)
N(2)	7501(16)	3892(14)	3247(8)	29(6)
C(21)	8245(20)	3335(21)	2899(10)	30(9)
C(22)	8673(22)	2203(21)	3140(12)	36(9)
C(23)	8111(23)	2092(20)	3678(11)	40(9)
N(21)	7447(17)	3119(16)	3748(9)	37(7)
N(3)	4753(16)	4711(12)	3369(8)	23(6)
C(31)	3248(21)	4736(21)	2995(10)	43(9)
C(32)	2539(24)	3804(21)	3227(11)	49(9)
C(33)	3643(22)	3261(19)	3712(11)	40(9)
N(31)	4955(17)	3783(14)	3815(9)	30(7)
B	6563(27)	3415(22)	4233(12)	35(10)
S(2)	-878(7)	3961(6)	1167(3)	68(3)
O(1A)	-228(34)	3228(29)	759(16)	100(10)
O(1B)	-1933(23)	3102(20)	1208(10)	98(7)
O(1C)	180(32)	4436(31)	1687(15)	71(9)
O(2C)	665(49)	4178(46)	1229(21)	123(14)
O(3C)	-951(39)	4735(35)	1755(21)	92(13)

[a]The estimated standard deviations in the parentheses are for the last significant digits.

[b]For anisotropically refined atoms, $U_{iso} \equiv 1/3\ \Sigma U_{ij}\vec{a}_i^*\cdot\vec{a}_j^* a_i a_j$, where the temperature factors are defined as $\exp(-2\pi^2 \Sigma h_i h_j a_i^* a_j^* U_{ij})$.

Table 2 (Continued)

Atom	x	y	z	U_{iso}
C(1S)	-1851(23)	5015(22)	594(13)	56(11)
F(1)	-1195(22)	5985(20)	503(10)	98(7)
F(2)	-2969(25)	4636(21)	72(12)	83(8)
F(3)	-3355(32)	5153(26)	529(15)	83(9)
F(4)	-2485(39)	5759(45)	951(19)	116(13)
F(5)	-1990(37)	4697(31)	-63(18)	101(12)
F(6)[a]	-1045	5580	231	75

[a]Parameters were kept fixed at the final cycle.

Table 3. The positional parameters[a] ($\times 10^4$) and U_{iso}[b] ($\times 10^3$) for $[HB(pz)_3](CO)_2W[\eta^2\text{-}CH(SMe)(PPh_2)]$

atom	x	y	z	U_{iso}
W	913(1)	2732(1)	3737(2)	39(0)
S	-885(7)	3828(5)	5056(11)	43(3)
P	-2185(8)	3256(5)	1617(11)	43(3)
B	3328(30)	1611(25)	6351(48)	42(14)
C(1)	929(25)	3644(19)	2538(37)	30(7)
O(1)	876(24)	4258(16)	1854(33)	64(11)
C(2)	623(24)	2354(18)	1291(36)	29(6)
O(2)	475(22)	2075(18)	-326(32)	76(11)
C(3)	-1082(26)	2882(19)	3476(37)	35(7)
C(4)	-1018(36)	3530(27)	7162(54)	70(11)
N(1)	1129(23)	1591(18)	5258(33)	50(10)
C(11)	415(29)	1126(20)	5511(45)	46(13)
C(12)	983(31)	510(19)	6574(48)	50(14)
C(13)	2177(28)	555(22)	7028(36)	44(13)
N(11)	2214(22)	1280(16)	6265(32)	42(10)
N(2)	2718(20)	1905(17)	3104(36)	42(10)
C(21)	3377(31)	1636(24)	1591(38)	50(15)
C(22)	4569(31)	1065(27)	1850(45)	58(16)
C(23)	4641(37)	996(30)	3607(47)	70(19)
N(21)	3614(23)	1444(16)	4349(33)	41(6)
N(3)	2022(23)	3180(17)	6156(29)	39(10)
C(31)	1854(35)	4006(20)	7025(49)	56(15)
C(32)	2833(37)	3878(25)	8468(45)	55(17)
C(33)	3469(29)	3034(25)	8420(42)	48(14)
N(31)	2947(23)	2592(19)	7043(33)	45(11)
C(41)	-3702(29)	3620(19)	2528(44)	46(13)
C(42)	-4030(33)	3031(24)	3314(59)	67(17)
C(43)	-5179(41)	3324(32)	3993(66)	88(23)
C(44)	-6021(27)	4204(32)	3709(63)	80(20)
C(45)	-5715(41)	4732(26)	2875(76)	91(23)
C(46)	-4543(33)	4396(26)	2294(56)	74(17)

[a]The estimated standard deviations in the parentheses are for the last significant digits.

[b]For anisotropically refined atoms, $U_{iso} \equiv 1/3\ \Sigma U_{ij}\vec{a}_i^*\cdot\vec{a}_j^* a_i a_j$, where the temperature factors are defined as $\exp(-2\pi^2\Sigma h_i h_j a_i^* a_j^* U_{ij})$.

Table 3 (Continued)

Atom	x	y	z	U_{iso}
C(51)	-2268(33)	2219(26)	251(42)	57(16)
C(52)	-2856(29)	2238(29)	-1403(39)	54(17)
C(53)	-2972(47)	1549(36)	-2753(70)	95(15)
C(54)	-2434(43)	654(34)	-2159(46)	85(23)
C(55)	-1703(48)	570(23)	-533(52)	83(21)
C(56)	-1732(39)	1381(22)	633(45)	69(16)

Table 4. The positional parameters[a] ($\times 10^4$) and U_{iso}[b] ($\times 10^3$) for $[HB(pz)_3](CO)_2(CS)W\text{-}Au(PPh_3)$

Atom	x	y	z	U_{iso}
W	3150(0)	1715(0)	4407(0)	34(0)
Au	3411(0)	2197(0)	6722(0)	44(0)
P	3390(2)	2068(1)	8616(2)	42(0)
S	3684(2)	3546(1)	5299(2)	53(0)
C(1)	3897(6)	1025(5)	5566(8)	47(3)
O(1)	4335(5)	583(4)	6149(7)	77(3)
C(2)	4291(6)	1939(5)	3962(8)	50(3)
O(2)	4949(6)	2067(5)	3683(8)	91(3)
C(3)	3419(5)	2677(4)	5060(7)	39(2)
N(1)	2224(5)	2265(3)	2910(6)	41(2)
C(11)	2189(7)	2967(5)	2557(8)	52(3)
C(12)	1430(7)	3086(5)	1652(9)	56(3)
C(13)	999(6)	2407(6)	1476(8)	54(3)
N(11)	1484(5)	1920(4)	2232(6)	43(2)
N(2)	2951(5)	811(4)	3120(6)	45(2)
C(21)	3560(7)	344(5)	2860(9)	56(3)
C(22)	3127(8)	-106(5)	1947(9)	63(4)
C(23)	2243(8)	100(5)	1685(9)	64(4)
N(21)	2145(5)	668(4)	2394(6)	47(2)
N(3)	1794(4)	1303(4)	4615(6)	42(2)
C(31)	1449(6)	1216(5)	5535(8)	52(3)
C(32)	587(7)	935(6)	5204(11)	67(4)
C(33)	413(6)	843(5)	4050(10)	59(3)
N(31)	1142(5)	1074(4)	3691(7)	47(2)
C(41)	2474(6)	1444(4)	8733(7)	41(2)
C(42)	2537(7)	717(5)	8393(9)	57(3)
C(43)	1809(7)	219(5)	8339(10)	61(3)
C(44)	1028(7)	472(6)	8649(9)	61(3)
C(45)	973(7)	1203(6)	8986(10)	64(4)
C(46)	1690(7)	1671(5)	9035(10)	57(3)
C(51)	4421(6)	1685(5)	9497(7)	47(3)
C(52)	4425(7)	1173(7)	10374(9)	74(4)
C(53)	5237(9)	916(8)	11041(11)	91(5)

[a]The estimated standard deviations in the parentheses are for the last significant digits.

[b]$U_{iso} \equiv 1/3\ \Sigma U_{ij} \vec{a}_i^* \cdot \vec{a}_j^* a_i a_j$, where the temperature factors are defined as $\exp(-2\pi^2 \Sigma h_i h_j a_i^* a_j^* U_{ij})$.

Table 4 (Continued)

Atom	x	y	z	U_{iso}
C(54)	6047(8)	1143(7)	10803(11)	81(4)
C(55)	6055(8)	1623(6)	9943(11)	72(4)
C(56)	5258(7)	1900(5)	9284(10)	62(3)
C(61)	3197(6)	2920(5)	9313(8)	50(3)
C(62)	3604(8)	3063(7)	10447(10)	73(4)
C(63)	3428(10)	3782(9)	10895(14)	105(7)
C(64)	2855(13)	4254(7)	10247(19)	110(8)
C(65)	2443(14)	4094(7)	9140(15)	125(8)
C(66)	2596(11)	3425(6)	8650(11)	96(6)
B	1279(7)	1124(6)	2455(9)	49(3)

Table 5. The positional parameters[a] ($\times 10^4$) and U_{iso}[b] ($\times 10^3$) for $[HB(pz)_3](CO)_2(CS)W\text{-}Au(PMe_3)$

Atom	x	y	z	U_{iso}
W	4107(1)	1135(1)	2154(1)	40(0)
Au	5141(1)	1454(1)	730(1)	51(0)
S	3522(5)	1350(6)	-72(5)	77(3)
P	6364(4)	1684(5)	176(5)	50(2)
C(1)	5155(18)	1597(14)	2413(19)	54(9)
O(1)	5728(11)	1887(11)	2697(15)	64(7)
C(2)	3609(16)	2168(17)	2210(23)	59(10)
O(2)	3304(14)	2756(13)	2231(19)	92(10)
C(3)	3901(13)	1247(15)	917(15)	46(8)
C(4)	6761(22)	930(26)	-492(29)	115(18)
C(5)	7098(16)	1799(24)	1077(25)	93(15)
C(6)	6445(21)	2571(26)	-410(30)	118(18)
N(1)	2956(12)	531(11)	2296(14)	45(7)
C(11)	2281(15)	643(17)	1860(17)	52(9)
C(12)	1716(16)	142(17)	2133(18)	55(9)
C(13)	2082(18)	-314(18)	2748(20)	64(11)
N(11)	2858(12)	-112(13)	2803(15)	50(7)
N(2)	4062(13)	982(11)	3666(14)	51(7)
C(21)	4245(16)	1466(20)	4313(17)	67(11)
C(22)	4143(19)	1102(22)	5091(16)	71(11)
C(23)	3873(19)	341(22)	4911(18)	75(13)
N(21)	3799(15)	291(13)	3989(16)	64(9)
N(3)	4528(12)	-102(11)	2204(14)	44(6)
C(31)	5050(15)	-477(13)	1749(16)	43(8)
C(32)	5109(15)	-1246(14)	2015(19)	52(9)
C(33)	4582(18)	-1307(14)	2696(19)	59(10)
N(31)	4204(13)	-619(10)	2821(15)	49(6)
B	3523(22)	-356(16)	3391(19)	51(11)

[a]The estimated standard deviations in the parentheses are for the last significant digits.

[b]$U_{iso} \equiv 1/3\ \Sigma U_{ij}\vec{a}_i^*\cdot\vec{a}_j^* a_i a_j$, where the temperature factors are defined as $\exp(-2\pi^2 \Sigma h_i h_j a_i^* a_j^* U_{ij})$.

Table 6. Anisotropic thermal parameters[a] ($\times 10^3$) for $[HB(pz)_3](CO)_2W[\eta^2\text{-}CH(SMe)]\cdot CF_3SO_3$

Atom	U_{11}	U_{22}	U_{33}	U_{23}	U_{13}	U_{12}
W	32(0)	27(0)	27(0)	3(1)	6(0)	-2(1)
S(1)	53(4)	31(4)	59(4)	2(3)	1(3)	9(3)
C(1)	45(14)	39(14)	41(15)	1(16)	3(12)	-14(15)
O(1)	65(10)	62(12)	34(10)	11(12)	-9(8)	-8(11)
C(2)	34(14)	15(15)	64(17)	-9(11)	-11(13)	0(11)
O(2)	39(9)	93(15)	56(11)	4(9)	18(9)	-26(10)
C(3)	40(15)	20(12)	70(16)	-7(13)	2(12)	13(12)
C(4)	55(16)	76(19)	63(18)	-9(16)	-8(14)	43(15)
N(1)	44(11)	29(14)	31(11)	-14(10)	18(9)	2(10)
C(11)	18(11)	46(15)	51(16)	-22(13)	5(11)	6(10)
C(13)	48(13)	47(17)	16(12)	5(11)	21(10)	11(11)
N(11)	42(10)	32(12)	25(10)	-1(10)	12(8)	2(9)
N(2)	21(9)	45(13)	20(10)	10(9)	4(8)	4(8)
C(21)	13(11)	51(17)	28(14)	-6(12)	11(10)	-13(11)
C(22)	38(14)	37(16)	38(15)	-18(12)	19(12)	-1(12)
C(23)	46(14)	33(14)	34(15)	15(12)	5(12)	-6(12)
N(21)	31(10)	34(12)	39(12)	1(10)	4(9)	3(9)
N(3)	31(10)	10(9)	26(10)	2(8)	9(8)	4(7)
C(31)	17(12)	81(20)	32(14)	-7(12)	8(10)	5(12)
C(32)	36(14)	56(16)	42(15)	9(13)	-3(12)	-8(12)
C(33)	28(12)	52(15)	50(15)	-11(13)	26(11)	-21(12)
N(31)	18(10)	20(10)	50(13)	6(10)	10(9)	11(8)
B	37(15)	43(17)	25(15)	-4(13)	11(12)	8(14)
S(2)	51(4)	89(6)	51(4)	19(4)	1(3)	14(4)
C(1S)	40(14)	66(17)	76(20)	-45(15)	37(14)	-1(13)

[a]The estimated standard deviations in the parentheses are for the least significant digits. The anisotropic temperature factors are defined as $\exp(-2\pi^2 \Sigma h_i h_j a_i^* a_j^* U_{ij})$.

Table 7. Anisotropic thermal parameters[a] ($\times 10^3$) for $[HB(pz)_3](CO)_2W[\eta^2\text{-}CH(SMe)(PPh_2)]$

Atom	U_{11}	U_{22}	U_{33}	U_{23}	U_{13}	U_{12}
W	46(1)	35(1)	35(1)	12(0)	7(0)	-9(1)
S	44(5)	38(4)	43(5)	11(4)	7(4)	-3(4)
P	45(5)	36(5)	46(5)	14(4)	2(4)	-8(4)
B	29(19)	48(23)	47(22)	12(17)	4(15)	-6(16)
O(1)	90(19)	51(15)	64(16)	24(13)	1(14)	-34(14)
O(2)	52(15)	80(19)	51(15)	1(13)	1(11)	30(13)
N(1)	40(16)	46(16)	34(15)	-3(12)	-22(12)	7(13)
C(11)	48(19)	32(18)	69(22)	4(16)	-5(16)	-34(16)
C(12)	62(22)	19(16)	76(24)	21(16)	14(18)	-13(15)
C(13)	51(20)	61(21)	17(15)	2(14)	2(13)	-15(16)
N(11)	49(16)	43(15)	43(15)	16(12)	12(12)	-18(12)
N(2)	17(12)	41(16)	67(18)	27(13)	-7(12)	-3(11)
C(21)	60(23)	80(25)	23(16)	1(15)	23(15)	-36(20)
C(22)	41(21)	90(28)	51(22)	8(19)	6(15)	-31(20)
C(23)	69(26)	96(32)	43(23)	24(21)	-8(19)	-25(24)
N(3)	52(16)	50(17)	19(12)	-2(12)	-11(11)	-31(13)
C(31)	79(26)	25(18)	64(24)	-8(16)	25(20)	-17(17)
C(32)	76(27)	53(26)	47(22)	-8(17)	18(19)	-38(22)
C(33)	41(19)	62(25)	40(20)	-6(16)	7(15)	-22(18)
N(31)	46(16)	64(19)	36(15)	21(14)	-6(12)	-28(15)
C(41)	49(20)	26(17)	61(22)	-4(15)	19(16)	-9(15)
C(42)	59(24)	39(20)	109(32)	4(19)	31(22)	-18(18)
C(43)	75(30)	91(34)	120(40)	11(28)	37(28)	-47(28)
C(44)	5(15)	100(34)	124(37)	-4(28)	17(18)	-8(18)
C(45)	79(32)	41(23)	160(48)	21(26)	29(31)	-19(22)
C(46)	41(21)	61(26)	85(28)	16(21)	11(19)	34(19)
C(51)	63(23)	85(28)	27(19)	15(17)	5(16)	-22(20)
C(52)	34(19)	117(34)	19(17)	8(19)	-6(14)	-40(21)
C(54)	119(35)	132(41)	23(19)	-30(22)	29(20)	-80(33)
C(55)	159(44)	26(19)	61(26)	-1(16)	1(26)	-32(23)
C(56)	103(30)	38(21)	41(20)	14(16)	17(19)	22(19)

[a]The estimated standard deviations in the parentheses are for the least significant digits. The anisotropic temperature factors are defined as $\exp(-2\pi^2 \Sigma h_i h_j a_i^* a_j^* U_{ij})$.

Table 8. Anisotropic thermal parameters[a] ($\times 10^3$) for $[HB(pz)_3](CO)_2(CS)W\text{-}Au(PPh_3)$

Atom	U_{11}	U_{22}	U_{33}	U_{23}	U_{13}	U_{12}
W	33(0)	32(0)	36(0)	-3(0)	6(0)	-2(0)
AU	46(0)	49(0)	37(0)	-1(0)	11(0)	-6(0)
P	47(1)	41(1)	40(1)	-4(1)	13(1)	-5(1)
S	60(1)	35(1)	60(2)	-1(1)	4(1)	-4(1)
O(1)	79(5)	55(4)	83(6)	13(4)	-8(4)	28(4)
C(1)	44(5)	42(5)	50(5)	-6(4)	0(4)	2(4)
O(2)	74(5)	123(7)	92(6)	-40(5)	48(5)	-44(5)
C(2)	37(5)	68(6)	44(5)	-22(5)	11(4)	-12(4)
C(3)	36(4)	37(4)	41(5)	3(4)	6(4)	-2(3)
N(11)	48(4)	36(4)	40(4)	-3(3)	0(3)	-4(3)
N(1)	42(4)	36(4)	38(4)	2(3)	0(3)	-6(3)
C(11)	59(6)	46(5)	43(5)	6(4)	-6(5)	-8(4)
C(12)	70(7)	44(5)	48(6)	11(4)	-1(5)	1(5)
C(13)	50(5)	69(6)	39(5)	2(5)	1(4)	-4(5)
N(21)	59(5)	36(4)	41(4)	-1(3)	4(4)	-7(3)
N(2)	51(4)	38(4)	45(4)	-8(3)	9(4)	-4(3)
C(21)	69(6)	35(5)	70(7)	-5(5)	31(6)	7(4)
C(22)	91(8)	43(5)	62(7)	-8(5)	28(6)	10(5)
C(23)	104(9)	37(5)	51(6)	-15(4)	19(6)	-12(5)
N(3)	33(4)	45(4)	47(4)	-2(3)	8(3)	-4(3)
C(31)	43(5)	60(6)	56(6)	-5(5)	21(5)	-6(4)
C(32)	49(6)	70(7)	84(8)	0(6)	23(6)	-10(5)
C(33)	42(5)	52(6)	83(8)	5(5)	14(5)	-10(4)
N(31)	34(4)	43(4)	56(5)	4(4)	-3(4)	-9(3)
C(41)	49(5)	41(4)	31(4)	4(4)	3(4)	3(4)
C(42)	55(6)	50(5)	66(7)	-1(5)	15(5)	6(5)
C(43)	63(6)	47(5)	78(7)	1(5)	24(6)	-10(5)
C(44)	57(6)	69(7)	53(6)	2(5)	6(5)	-21(5)
C(45)	47(6)	67(6)	83(8)	-13(6)	23(6)	-6(5)
C(46)	56(6)	47(5)	76(7)	-12(5)	27(5)	-5(5)
C(51)	49(5)	53(5)	38(5)	-3(4)	8(4)	-3(4)
C(52)	47(6)	109(9)	61(7)	42(7)	4(5)	2(6)
C(53)	79(9)	105(10)	79(9)	32(8)	-2(7)	10(7)
C(54)	60(7)	80(8)	88(9)	1(7)	-9(7)	12(6)
C(55)	55(7)	72(7)	91(9)	0(7)	23(6)	-2(6)
C(56)	54(6)	59(6)	76(7)	7(6)	19(6)	-11(5)

[a]The estimated standard deviations in the parentheses are for the least significant digits. The anisotropic temperature factors are defined as $\exp(-2\pi^2 \Sigma h_i h_j a_i^* a_j^* U_{ij})$.

Table 8 (Continued)

Atom	U_{11}	U_{22}	U_{33}	U_{23}	U_{13}	U_{12}
C(61)	53(6)	53(5)	49(6)	-9(5)	19(5)	-16(4)
C(62)	65(7)	94(8)	67(8)	-32(6)	30(6)	-24(6)
C(63)	87(10)	132(13)	110(12)	-86(11)	53(9)	-49(9)
C(64)	144(15)	50(7)	172(18)	-32(9)	109(15)	-16(8)
C(65)	221(20)	53(7)	111(12)	2(8)	61(14)	49(10)
C(66)	167(14)	47(6)	75(9)	2(6)	28(9)	31(8)
B	50(6)	42(5)	46(6)	-2(5)	-8(5)	-11(5)

Table 9. Anisotropic thermal parameters[a] ($\times 10^3$) for $[HB(pz)_3](CO)_2(CS)W\text{-}Au(PMe_3)$

Atom	U_{11}	U_{22}	U_{33}	U_{23}	U_{13}	U_{12}
W	40(1)	40(1)	39(1)	-2(0)	1(1)	-2(1)
AU	43(1)	57(1)	53(1)	7(1)	5(1)	-7(1)
S	68(5)	117(8)	46(4)	8(4)	-5(4)	1(5)
P	34(3)	68(5)	48(4)	8(4)	1(3)	-3(3)
C(1)	65(18)	28(13)	71(18)	7(13)	-3(17)	-11(14)
O(1)	44(11)	60(12)	88(15)	-4(11)	-11(11)	-16(10)
C(2)	44(16)	48(17)	85(22)	-6(17)	2(17)	-12(14)
O(2)	100(18)	55(14)	121(22)	-2(15)	-10(17)	24(13)
C(3)	35(13)	63(18)	39(14)	11(12)	-4(11)	-12(13)
C(4)	78(24)	131(37)	136(35)	-71(29)	34(25)	-3(25)
C(5)	32(16)	132(33)	117(30)	34(25)	-6(18)	-19(19)
C(6)	73(23)	124(33)	156(40)	104(30)	-44(25)	-36(24)
N(3)	51(13)	36(11)	45(12)	-3(10)	-26(11)	10(11)
C(31)	39(14)	37(14)	52(14)	-25(12)	-16(13)	25(12)
C(32)	49(15)	38(15)	70(18)	7(13)	17(15)	9(13)
C(33)	82(21)	38(15)	58(17)	11(12)	9(17)	-2(15)
N(31)	61(14)	30(10)	57(12)	0(11)	5(13)	-10(11)
N(1)	48(13)	39(11)	47(13)	-14(10)	-14(11)	2(10)
C(11)	38(15)	73(20)	45(15)	-2(13)	-14(13)	-1(15)
C(12)	59(18)	73(19)	34(13)	-17(16)	3(15)	-41(16)
C(13)	71(21)	74(21)	48(18)	-2(16)	28(17)	-40(17)
N(11)	46(13)	55(14)	50(13)	17(12)	4(12)	-11(11)
N(2)	65(14)	35(12)	54(13)	5(10)	-16(13)	-3(12)
C(21)	60(17)	118(26)	23(13)	-24(15)	-10(14)	24(19)
C(22)	74(19)	117(26)	22(13)	-27(16)	-12(14)	32(22)
C(23)	74(23)	119(30)	32(15)	-9(17)	8(16)	38(22)
N(21)	74(17)	49(14)	69(16)	2(12)	45(14)	22(13)
B	81(25)	32(16)	39(16)	4(13)	-4(18)	-32(17)

[a]The estimated standard deviations in the parentheses are for the least significant digits. The anisotropic temperature factors are defined as $\exp(-2\pi^2 \Sigma h_i h_j a_i^* a_j^* U_{ij})$.

RESULTS AND DISCUSSION

Structure of $[HB(pz)_3](CO)_2W[\eta^2\text{-}CH(SMe)]\cdot CF_3SO_3$

An X-ray structure determination of a deep violet single crystal of $[HB(pz)_3](CO)_2W[\eta^2\text{-}CH(SMe)]\cdot CF_3SO_3$ revealed that the η^2-carbene ligand is bonded to the tungsten through both the C and S atoms as shown in Figure 1 (left). Comparisons of common bond distances and angles in $[HB(pz)_3](CO)_2W[\eta^2\text{-}CH(SMe)]\cdot CF_3SO_3$ and $[HB(pz)_3](CO)_2W[\eta^2\text{-}CH(SMe)(PPh_2)]$ are given in Table 10 and 12, respectively, while the remaining bond distances and angles are given in Table 11 and 13, respectively. The W-C(3) bond distance (1.93(2)A) is between the W-C(sp^2) single bond distance (2.32(2)A) in $Cp(CO)_3W\text{-}Ph$[11] and the W≡C triple bond distances (1.81-1.82A) in $Cp(CO)_2W{\equiv}C(p\text{-tolyl})$,[12] $Cp(CO)_2W{\equiv}CSiPh_3$,[13] and $Cp(CO)(Ph_3P)W{\equiv}CSPh$;[14] however, the W-C(3) distance is closer to the W=C distances in the carbene complexes, $Cp(CO)_2W{=}C(CF_3)C(CF_3)(COSMe)$, 1.962(8)A, and $Cp_2W{=}CHPh$, 2.05A.[15] This suggests that the W=C(3) bond is best represented as a carbene-like interaction. The W-S(1) distance (2.481(6)A) is very similar to that (2.440(2)A) in $Cp(CO)_2W[C(CO_2Me){=}C(CO_2Me)C(O)SMe]$.[16] The C(3)-S(1) distance (1.72(2)A), considerably shorter than C(4)-S(1) of 1.85(2)A, appears to be shorter than an S-C(sp^2) distance as in $C(S\text{-}Ph)_4$, 1.776A average;[17] however, the magnitude of the standard deviation does not permit a definite conclusion. While no

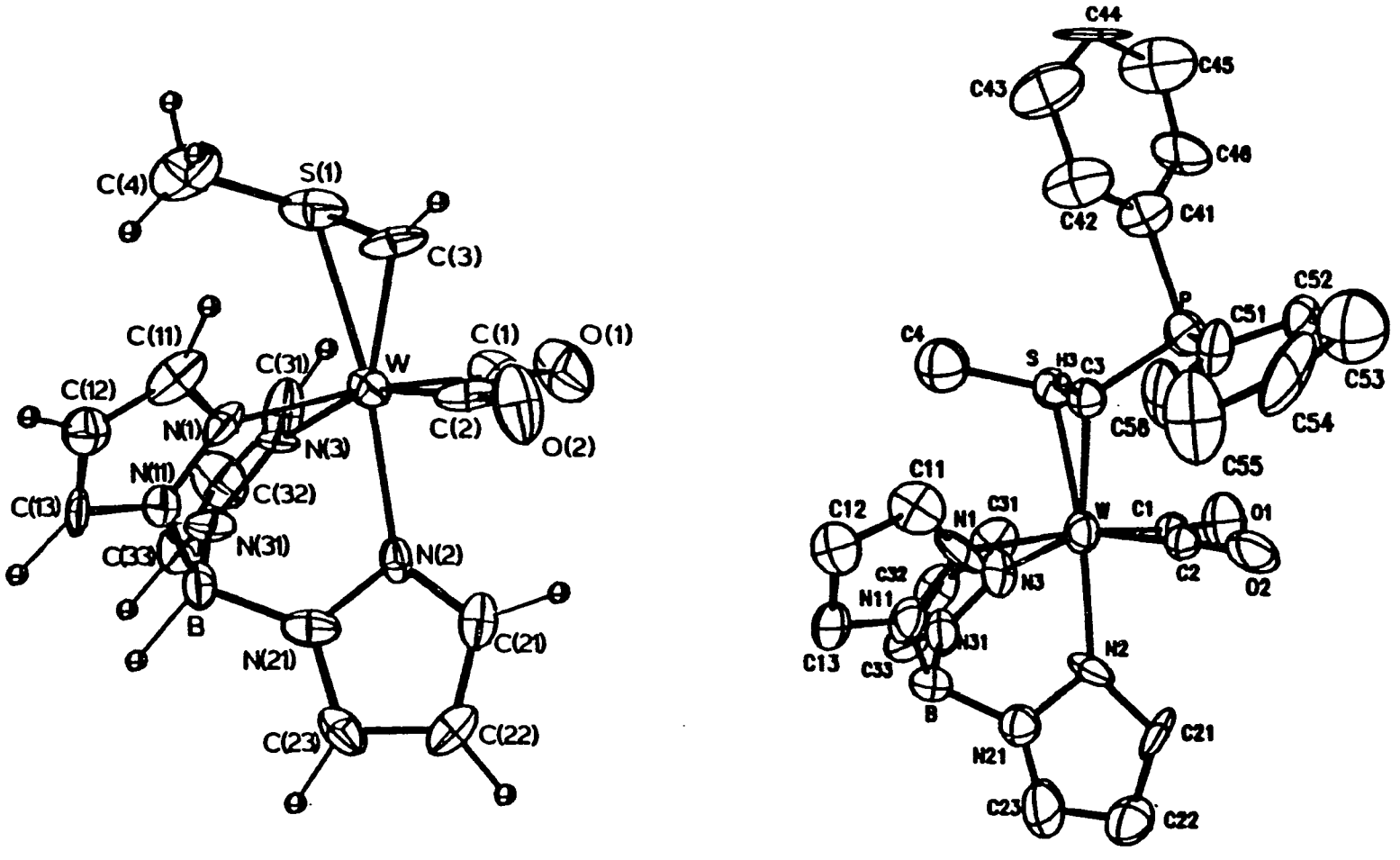

Figure 1. ORTEP drawings of $[HB(pz)_3](CO)_2W[\eta^2\text{-}CH(SMe)]^+$ (left) and $[HB(pz)_3](CO)_2W[\eta^2\text{-}CH(SMe)(PPh_2)]$ (right)

Table 10. Comparison of common bond distances[a] (A) in $[HB(pz)_3](CO)_2W[\eta^2\text{-}CH(SMe)]\cdot CF_3SO_3$, 1, and $[HB(pz)_3](CO)_2W[\eta^2\text{-}CH(SMe)(PPh_2)]$, 2

		1	2
W	- S(1)	2.481(6)	2.435(9)
W	- C(1)	2.036(22)	1.876(29)
W	- C(2)	2.074(21)	1.865(28)
W	- C(3)	1.934(20)	2.223(30)
W	- N(1)	2.210(16)	2.277(27)
W	- N(2)	2.205(14)	2.134(25)
W	- N(3)	2.202(13)	2.225(26)
S(1)	- C(3)	1.726(20)	1.798(31)
S(1)	- C(4)	1.841(23)	1.810(43)
N(11)	- B	1.567(27)	1.539(45)
N(21)	- B	1.565(27)	1.571(45)
N(31)	- B	1.549(27)	1.489(46)
C(1)	- O(1)	1.135(26)	1.181(39)
C(2)	- O(2)	1.101(25)	1.237(38)
N(1)	- C(11)	1.384(25)	1.339(42)
N(1)	- N(11)	1.347(22)	1.361(37)
C(11)	- C(12)	1.378(28)	1.334(47)
C(12)	- C(13)	1.350(27)	1.395(47)
C(13)	- N(11)	1.366(23)	1.412(41)
N(2)	- C(21)	1.339(24)	1.402(44)
N(2)	- N(21)	1.397(21)	1.408(36)
C(21)	- C(22)	1.397(29)	1.385(52)
C(22)	- C(23)	1.419(29)	1.358(58)
C(23)	- N(21)	1.358(25)	1.314(50)
N(3)	- C(31)	1.388(24)	1.322(45)
N(3)	- N(31)	1.391(20)	1.357(38)
C(31)	- C(32)	1.428(28)	1.447(54)
C(32)	- C(33)	1.355(28)	1.298(54)
C(33)	- N(31)	1.331(24)	1.332(45)
P	- C(3)		1.809(31)
P	- C(41)		1.855(33)
P	- C(51)		1.803(39)

[a]The estimated standard deviations in the parentheses are for the least significant digits.

Table 11. Other bond distances[a] (A) in $[HB(pz)_3](CO)_2W[\eta^2$-$CH(SMe)]\cdot CF_3SO_3$, **1**, and $[HB(pz)_3](CO)_2W[\eta^2$-$CH(SMe)(PPh_2)]$, **2**

1			**2**		
S(2)	- O(1A)	1.476(30)	C(41) - C(42)		1.389(51)
S(2)	- O(1B)	1.422(20)	C(41) - C(46)		1.320(52)
S(2)	- O(1C)	1.340(30)	C(42) - C(43)		1.398(63)
S(2)	- O(2C)	1.446(43)	C(43) - C(44)		1.453(65)
S(2)	- O(3C)	1.552(36)	C(44) - C(45)		1.315(65)
S(2)	- C(1S)	1.743(23)	C(45) - C(46)		1.390(63)
C(1S)	- F(1)	1.312(29)	C(51) - C(52)		1.343(54)
C(1S)	- F(2)	1.332(31)	C(51) - C(56)		1.344(55)
C(1S)	- F(3)	1.396(35)	C(52) - C(53)		1.381(67)
C(1S)	- F(4)	1.398(45)	C(53) - C(54)		1.489(74)
C(1S)	- F(5)	1.411(39)	C(54) - C(55)		1.395(67)
C(1S)	- F(6)	1.408(22)	C(55) - C(56)		1.416(60)

[a]The estimated standard deviations in the parentheses are for the least significant digits.

Table 12. Comparison of common bond angles[a] (°) in $[HB(pz)_3](CO)_2W[\eta^2\text{-}CH(SMe)]\cdot CF_3SO_3$, 1, and $[HB(pz)_3](CO)_2W[\eta^2\text{-}CH(SMe)(PPh_2)]$, 2

			1	2
S(1)	- W	- C(1)	89.8(6)	86.1(9)
S(1)	- W	- C(2)	116.2(6)	113.5(9)
S(1)	- W	- C(3)	43.9(6)	45.2(8)
S(1)	- W	- N(1)	95.8(4)	98.5(7)
S(1)	- W	- N(2)	165.1(4)	166.6(7)
S(1)	- W	- N(3)	84.2(4)	86.6(7)
C(1)	- W	- C(2)	89.5(8)	72.6(12)
C(1)	- W	- C(3)	88.7(8)	102.0(12)
C(1)	- W	- N(1)	171.3(7)	173.7(11)
C(1)	- W	- N(2)	89.8(7)	93.3(11)
C(1)	- W	- N(3)	90.4(7)	93.0(11)
C(2)	- W	- C(3)	72.3(8)	78.4(11)
C(2)	- W	- N(1)	93.9(7)	109.3(11)
C(2)	- W	- N(2)	78.7(7)	78.9(11)
C(2)	- W	- N(3)	159.6(7)	153.7(11)
C(3)	- W	- N(1)	99.8(7)	84.5(10)
C(3)	- W	- N(2)	151.1(7)	147.3(10)
C(3)	- W	- N(3)	128.1(7)	127.0(10)
N(1)	- W	- N(2)	83.1(6)	81.1(10)
N(1)	- W	- N(3)	83.6(5)	82.8(9)
N(2)	- W	- N(3)	80.8(5)	80.1(9)
W	- S(1)	- C(3)	50.9(7)	61.2(10)
W	- S(1)	- C(4)	110.9(7)	109.0(14)
C(3)	- S(1)	- C(4)	105.4(10)	102.1(17)
W	- C(1)	- O(1)	176.9(19)	175.4(26)
W	- C(2)	- O(2)	176.3(18)	177.6(25)
W	- C(3)	- S(1)	85.2(9)	73.7(11)
W	- N(1)	- C(11)	132.9(13)	136.2(22)
W	- N(1)	- N(11)	121.7(11)	117.7(19)
C(11)	- N(1)	- N(11)	105.4(15)	106.0(25)
N(1)	- C(11)	- C(12)	110.0(17)	113.0(30)
C(11)	- C(12)	- C(13)	105.8(17)	106.4(30)
C(12)	- C(13)	- N(11)	109.1(16)	105.6(27)
N(1)	- N(11)	- C(13)	109.7(14)	108.7(24)
W	- N(2)	- C(21)	134.6(12)	136.6(22)
W	- N(2)	- N(21)	118.6(11)	123.3(18)

[a]The estimated standard deviations in the parentheses are for the least significant digits.

Table 12 (Continued)

			1	2
C(21)	- N(2)	- N(21)	106.4(14)	100.2(24)
N(2)	- C(21)	- C(22)	112.0(17)	114.8(31)
C(21)	- C(22)	- C(23)	103.8(17)	101.1(34)
C(22)	- C(23)	- N(21)	108.8(17)	113.5(37)
N(2)	- N(21)	- C(23)	108.9(15)	110.4(28)
W	- N(3)	- C(31)	130.3(12)	127.8(23)
W	- N(3)	- N(31)	122.0(10)	122.3(19)
C(31)	- N(3)	- N(31)	107.1(13)	109.7(27)
N(3)	- C(31)	- C(32)	107.4(16)	102.6(31)
C(31)	- C(32)	- C(33)	105.6(18)	111.1(35)
C(32)	- C(33)	- N(31)	111.7(17)	106.1(33)
N(3)	- N(31)	- C(33)	108.3(14)	110.2(27)
N(1)	- N(11)	- B	120.4(15)	124.2(25)
C(13)	- N(11)	- B	129.2(15)	126.9(26)
N(2)	- N(21)	- B	122.0(15)	119.0(24)
C(23)	- N(21)	- B	128.7(16)	130.2(30)
N(3)	- N(31)	- B	119.1(14)	120.9(26)
C(33)	- N(31)	- B	131.7(16)	128.6(29)
N(11)	- B	- N(21)	106.6(15)	104.2(25)
N(11)	- B	- N(31)	107.8(15)	108.4(27)
N(21)	- B	- N(31)	108.5(15)	109.8(27)

Table 13. Other bond angles[a] (°) in $[HB(pz)_3](CO)_2W[\eta^2$-$CH(SMe)]\cdot CF_3SO_3$, 1, and $[HB(pz)_3](CO)_2W[\eta^2$-$CH(SMe)(PPh_2)]$, 2

1		2	
O(1A)-S(2) -O(1B)	95.0(14)	C(3) -P -C(41)	104.3(14)
O(1A)-S(2) -O(1C)	111.7(17)	C(3) -P -C(51)	103.1(16)
O(1A)-S(2) -O(2C)	63.0(21)	C(41)-P -C(51)	98.5(16)
O(1A)-S(2) -O(3C)	159.0(18)	W -C(3) -P	125.8(15)
O(1A)-S(2) -C(1S)	101.8(14)	S -C(3) -P	110.5(16)
O(1B)-S(2) -O(1C)	125.2(15)	P -C(41)-C(42)	119.9(26)
O(1B)-S(2) -O(2C)	145.4(19)	P -C(41)-C(46)	121.8(28)
O(1B)-S(2) -O(3C)	96.9(16)	C(42)-C(41)-C(46)	117.8(34)
O(1B)-S(2) -C(1S)	107.2(11)	C(41)-C(42)-C(43)	118.7(37)
O(1C)-S(2) -O(2C)	52.7(21)	C(42)-C(43)-C(44)	118.6(41)
O(1C)-S(2) -O(3C)	47.4(18)	C(43)-C(44)-C(45)	121.6(42)
O(1C)-S(2) -C(1S)	112.4(15)	C(44)-C(45)-C(46)	115.8(43)
O(2C)-S(2) -O(3C)	98.0(22)	C(41)-C(46)-C(45)	127.2(39)
O(2C)-S(2) -C(1S)	103.5(19)	P -C(51)-C(52)	119.2(30)
O(3C)-S(2) -C(1S)	91.2(15)	P -C(51)-C(56)	127.7(31)
S(2) -C(1S)-F(1)	120.9(17)	C(52)-C(51)-C(56)	112.9(36)
S(2) -C(1S)-F(2)	117.1(17)	C(51)-C(52)-C(53)	130.9(41)
S(2) -C(1S)-F(3)	115.8(18)	C(52)-C(53)-C(54)	112.1(44)
S(2) -C(1S)-F(4)	105.0(21)	C(53)-C(54)-C(55)	119.8(44)
S(2) -C(1S)-F(5)	112.0(19)	C(54)-C(55)-C(56)	116.3(41)
S(2) -C(1S)-F(6)	116.1(14)	C(51)-C(56)-C(55)	126.7(38)
F(1) -C(1S)-F(2)	115.8(21)		
F(1) -C(1S)-F(3)	114.2(21)		
F(1) -C(1S)-F(4)	83.2(22)		
F(1) -C(1S)-F(5)	87.9(20)		
F(1) -C(1S)-F(6)	33.5(10)		
F(2) -C(1S)-F(3)	56.3(17)		
F(2) -C(1S)-F(4)	106.5(24)		
F(2) -C(1S)-F(5)	45.4(18)		
F(2) -C(1S)-F(6)	96.6(17)		
F(3) -C(1S)-F(4)	51.5(21)		
F(3) -C(1S)-F(5)	99.8(22)		
F(3) -C(1S)-F(6)	128.0(20)		
F(4) -C(1S)-F(5)	141.1(27)		
F(4) -C(1S)-F(6)	115.5(22)		
F(5) -C(1S)-F(6)	57.4(16)		

[a]The estimated standard deviations in the parentheses are for the least significant digits.

other η^2-CH(SMe) complexes have been reported, the C-S distances in several η^2-CH_2SMe complexes are known; the examples closest to the present system are $Cp(CO)_2Mo(\eta^2$-$CH_2SMe)$[18] and $[Me_2Ga(N_2C_3H_3)(OCH_2CH_2NMe_2)]Mo(CO)_2(\eta^2$-$CH_2SMe)$[19] which have C-S distances of 1.78 and 1.744A, respectively. The dihedral angle between the C(3)-S(1)-C(4) and W-C(3)-S(1) planes is 103.8°.

Structure of $[HB(pz)_3](CO)_2W[\eta^2$-CH(SMe)$(PPh_2)]$

To ensure that the ligand $[CH(SMe)(PPh_2)]$ is bonded to the tungsten through both C and S atoms, and to establish the stereochemistry within the ligand, an X-ray structural determination was undertaken. The $[HB(pz)_3](CO)_2W[\eta^2$-CH(SMe)] portion of the molecule retains the atomic connectivity of the carbene cation, $[HB(pz)_3](CO)_2W[\eta^2$-$CH(SMe)]^+$, as shown in Figure 1 (right). Some structural changes, however, are noticeable. The W-S bond distance of 2.440(9)A is somewhat shorter than the 2.481(6)A distance found in the carbene cation. The W-C(3) distance (2.22(3)A) is substantially longer than the W=C(carbene) distance (1.93(2)A) in the cation and is comparable to W-C(sp^3) bond distances found in $W(\equiv CCMe_3)(=CHCMe_3)(CH_2CMe_3)$(dmpe) (2.258(9)A)[20] and in $[Cp_2W(CH_3)(CH_2CH_2$-$PMe_2Ph)]PF_6$ (avg. 2.26(3)A).[21] The S-C(3) distance (1.80(3)A) is similar to single bond S-C(sp^3)

distances obtained in microwave studies of MeSH (1.819A)[22] and Me_2S (1.802A).[23] Also, S-C(3) is comparable to S-C(4) (1.82(4)A), but is longer than the S-C(3) distance (1.72(2)A) in the carbene cation, $[HB(pz)_3](CO)_2W[\eta^2\text{-}CH(SMe)]\cdot CF_3SO_3$. Unfortunately, the large estimated standard deviations make more precise comparisons impossible. The single bond C(3)-P distance (1.81(3)A) is similar to P-C(sp^3) distances (avg. 1.829(3)A) found in $PPh_2CH_2CH_2PPh_2$ (dppe).[24] These changes in bond distances from the molecules $[HB(pz)_3](CO)_2W[\eta^2\text{-}CH(SMe)]\cdot CF_3SO_3$ to $[HB(pz)_3](CO)_2W[\eta^2\text{-}CH(SMe)(PPh_2)]$ involving C(3) can be easily rationalized by recognizing that the C(3) atom is approximately sp^2 hybridized in the former and sp^3 in the latter. All of the bonds around C(3) in the latter are those expected for single bond distances to an sp^3 C atom.

P and C(4) are <u>trans</u> to each other with respect to the WSC(3) plane[25] minimizing possible steric hindrance of the PPh_2 group with the methyl or pyrazolyl group. The groups around the C(3)-P bond have a staggered conformation, C(41) being <u>trans</u> to W and C(51) <u>trans</u> to S.[26] One may view the remaining lone pair on P as being <u>trans</u> to H(3). Thus, the orientation of the PPh_2 group minimizes steric repulsion with the remainder of the molecule.

W-CO distances (avg. 1.89(3)A) are significantly shorter than those of the carbene cation (avg. 2.07(2)A), suggesting enhanced π-backbonding to the carbonyls, which is supported by the substantially lower ν(CO) values for $[HB(pz)_3](CO)_2W[\eta^2\text{-}$

$CH(SMe)(PPh_2)]$ (1809, 1935 cm^{-1}) than for $[HB(pz)_3](CO)_2W[\eta^2$-$CH(SMe)]\cdot CF_3SO_3$ (1996, 2067 cm^{-1}). The bond angle C(1)-W-C(2), 73(1)°, is substantially smaller than that of the carbene cation (89.3(8)°); this change in the orientation of the C(2)O(2) group might be ascribed to the close proximity of one of the phenyl rings (O(2)···C(51) = 3.19(5)A, O(2)···C(56) = 3.34(5)A) and the phophorus atom (P···C(2) = 3.11(3)A, P···O(2) = 3.42(3)A) (Figure 2).

Structure of $[HB(pz)_3](CO)_2(CS)W$-$Au(PR_3)$, (R = Ph or Me)

Single crystal X-ray diffraction studies of $[HB(pz)_3](CO)_2(CS)W$-$Au(PPh_3)$ and $[HB(pz)_3](CO)_2(CS)W$-$Au(PMe_3)$ show these molecules to have essentially the same structures (Figures 3 and 4) with a W-Au bond bridged by semibridging CS and CO ligands; the major difference between the structures is the Au-C(1) distance, which is discussed later. Figure 5 contains bond distances and angles around the semibridging CS and CO and terminal CO ligands in the complex $[HB(pz)_3](CO)_2(CS)W$-$Au(PPh_3)$. Selected bond distances and bond angles for both compounds are given in Tables 14 and 15, respectively. Since the bond distances and angles are more precise for $[HB(pz)_3](CO)_2(CS)W$-$Au(PPh_3)$ (R = 3.1%) than $[HB(pz)_3](CO)_2(CS)W$-$Au(PMe_3)$ (R = 5.2%), the complex $[HB(pz)_3](CO)_2(CS)W$-$Au(PPh_3)$ will be discussed in greater

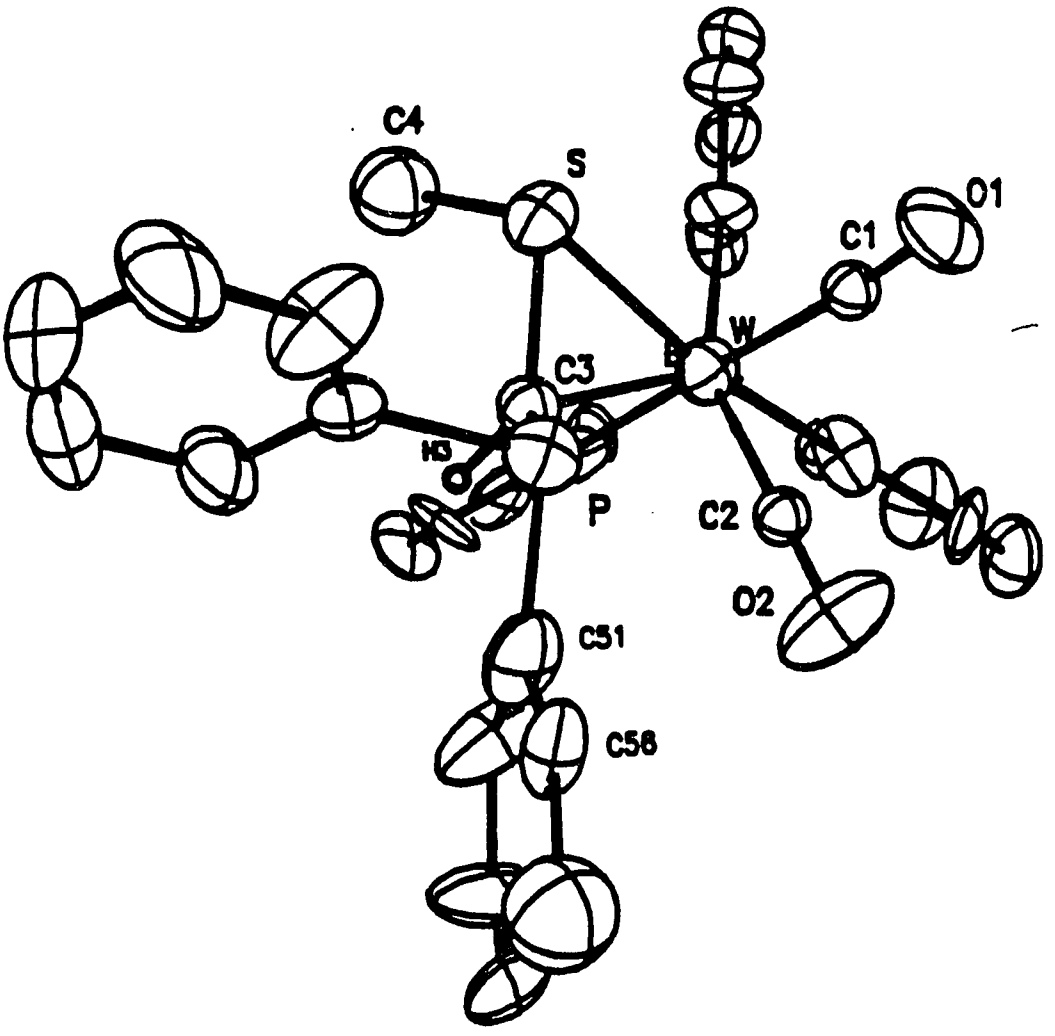

Figure 2. Perspective of $[HB(pz)_3](CO)_2W[\eta^2\text{-}CH(SMe)(PPh_2)]$, viewed down the W-B bond

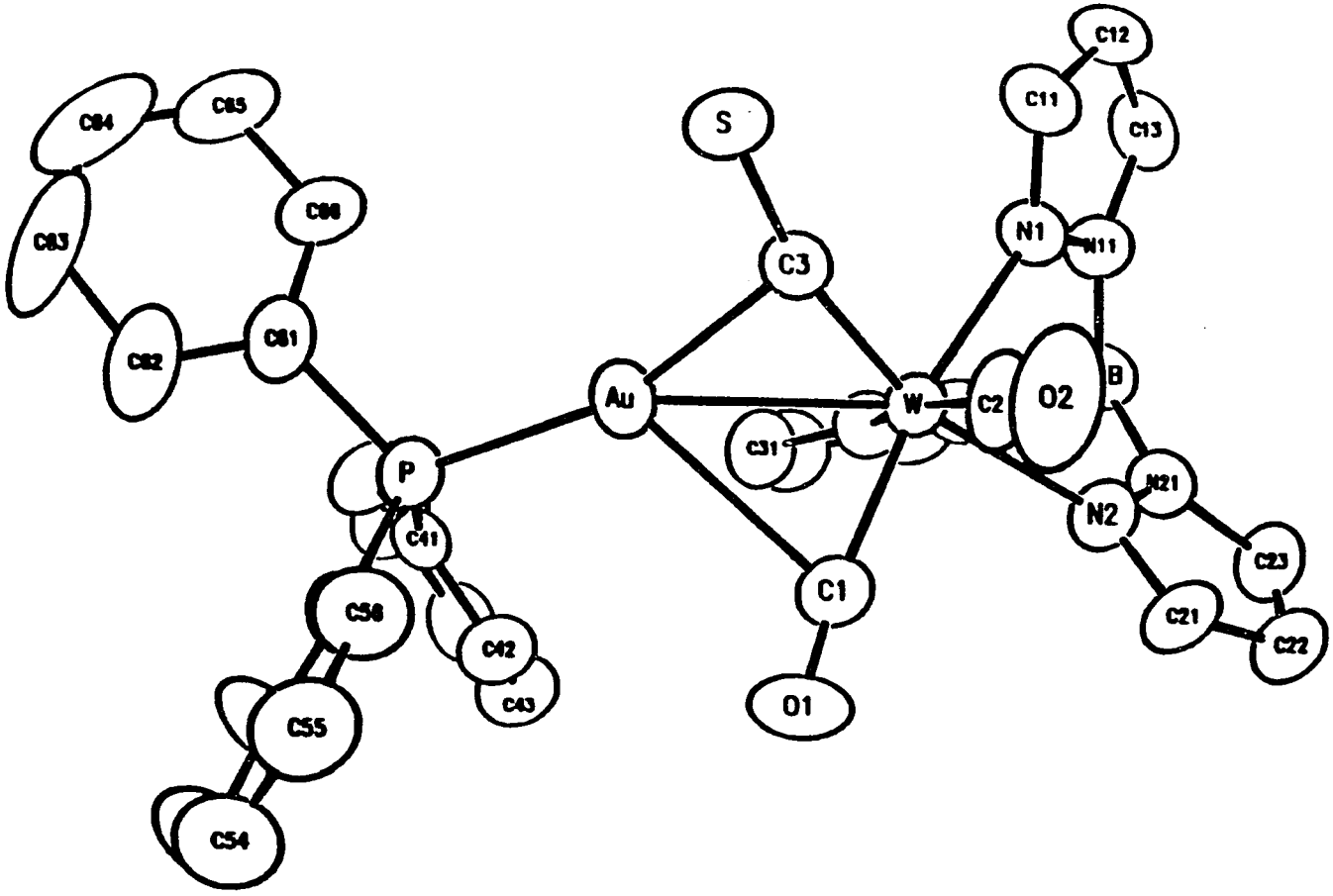

Figure 3. An ORTEP drawing of the molecule $[HB(pz)_3](CO)_2(CS)W\text{-}Au(PPh_3)$

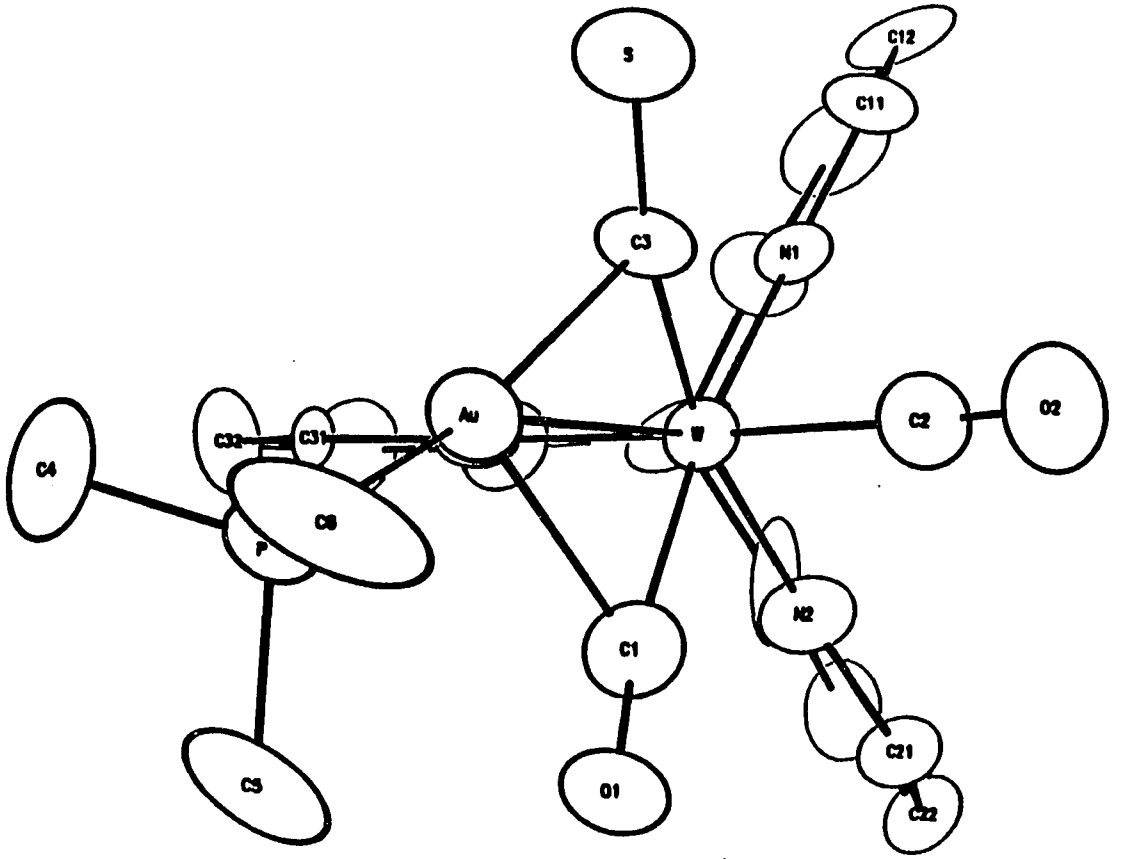

Figure 4. An ORTEP drawing of the molecule $[HB(pz)_3](CO)_2(CS)W\text{-}Au(PMe_3)$, viewed down the W-B bond

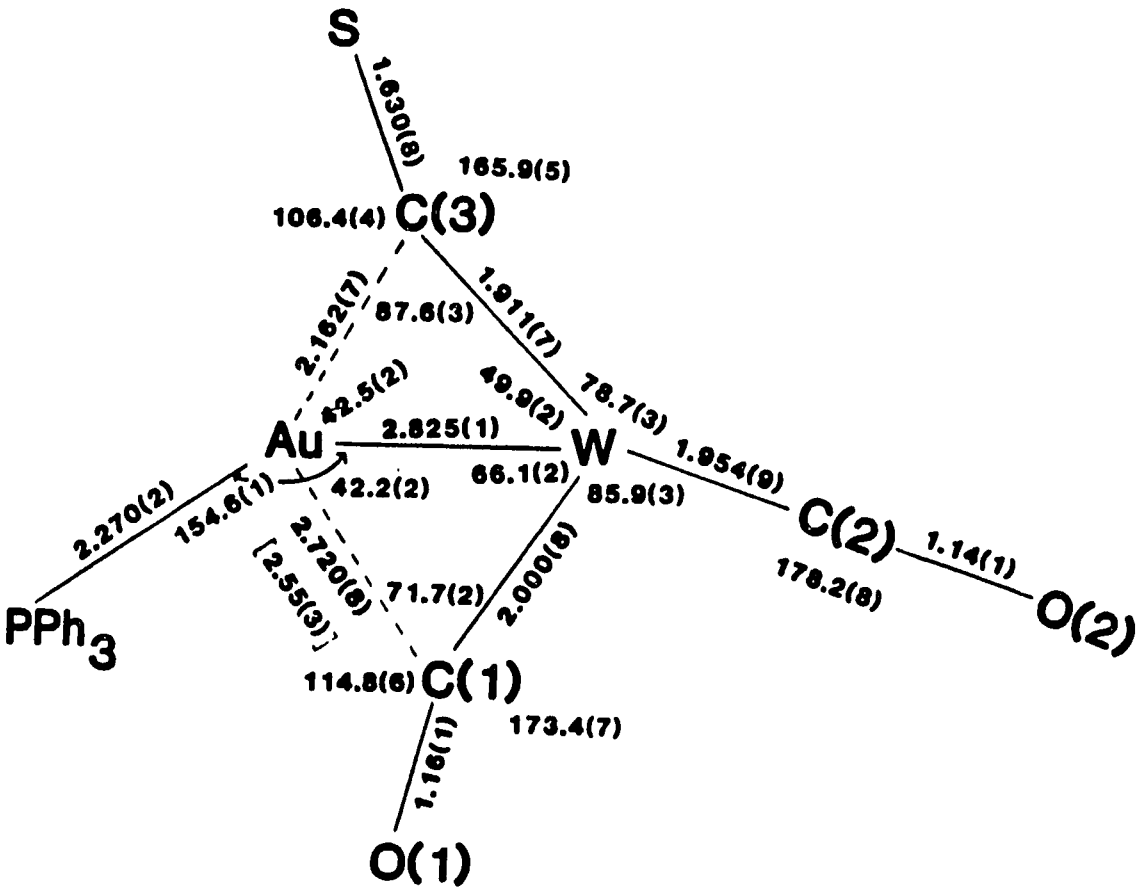

Figure 5. Bond distances and angles around the semibridging CS and CO and terminal CO ligands in the complex $[HB(pz)_3](CO)_2(CS)W\text{-}Au(PPh_3)$. The significant difference between the PPh_3 and PMe_3 complexes is in the Au-C(1) distance; this distance in the PMe_3 complex is shown in square brackets

Table 14. Comparison of common distances[a] (A)in $[HB(pz)_3](CO)_2(CS)W-Au(PPh_3)$, 3, and $[HB(pz)_3](CO)_2(CS)W-Au(PMe_3)$, 4

		3	4
W	- Au	2.825(0)	2.824(1)
W	- C(1)	2.000(8)	1.985(28)
W	- C(2)	1.954(9)	1.966(30)
W	- C(3)	1.911(7)	1.905(24)
W	- N(1)	2.223(6)	2.221(20)
W	- N(2)	2.212(6)	2.293(21)
W	- N(3)	2.243(6)	2.242(20)
Au	- S	3.054(2)	3.005(9)
Au	- P	2.270(2)	2.269(7)
Au	- C(1)	2.720(8)	2.546(28)
Au	- C(3)	2.162(7)	2.151(24)
Au	- O(1)	3.374(7)	3.212(20)
S	- C(3)	1.630(8)	1.631(25)
P	- C(41)	1.814(8)	1.773(43)
P	- C(51)	1.796(8)	1.850(37)
P	- C(61)	1.806(9)	1.766(43)
C(1)	- O(1)	1.159(11)	1.173(34)
C(2)	- O(2)	1.141(12)	1.136(39)
N(1)	- C(11)	1.335(11)	1.333(34)
N(1)	- N(11)	1.365(9)	1.352(29)
C(11)	- C(12)	1.391(12)	1.352(39)
C(12)	- C(13)	1.383(13)	1.363(42)
C(13)	- N(11)	1.345(11)	1.364(37)
N(11)	- B	1.511(12)	1.493(38)
N(2)	- C(21)	1.335(11)	1.316(36)
N(2)	- N(21)	1.340(9)	1.358(32)
C(21)	- C(22)	1.392(13)	1.340(43)
C(22)	- C(23)	1.347(14)	1.411(46)
C(23)	- N(21)	1.358(12)	1.397(40)
N(21)	- B	1.560(12)	1.505(39)
N(3)	- C(31)	1.324(11)	1.291(31)
N(3)	- N(31)	1.355(9)	1.397(29)
C(31)	- C(32)	1.365(13)	1.384(35)
C(32)	- C(33)	1.345(14)	1.363(38)
C(33)	- N(31)	1.336(11)	1.359(35)
N(31)	- B	1.533(12)	1.508(38)

[a]The estimated standard deviations in the parentheses are for the least significant digits.

Table 14 (Continued)

	3	4
C(41) - C(42)	1.386(12)	
C(41) - C(46)	1.375(12)	
C(42) - C(43)	1.409(13)	
C(43) - C(44)	1.390(13)	
C(44) - C(45)	1.391(14)	
C(45) - C(46)	1.364(14)	
C(51) - C(52)	1.394(13)	
C(51) - C(56)	1.398(13)	
C(52) - C(53)	1.373(16)	
C(53) - C(54)	1.377(17)	
C(54) - C(55)	1.345(16)	
C(55) - C(56)	1.366(15)	
C(61) - C(62)	1.369(14)	
C(61) - C(66)	1.394(15)	
C(62) - C(63)	1.454(18)	
C(63) - C(64)	1.325(22)	
C(64) - C(65)	1.348(23)	
C(65) - C(66)	1.386(20)	

Table 15. Comparison of common angle[a] (°) in $[HB(pz)_3](CO)_2(CS)W\text{-}Au(PPh_3)$, 3, and $[HB(pz)_3](CO)_2(CS)W\text{-}Au(PMe_3)$, 4

			3	4
Au	- W	- C(1)	66.1(2)	61.0(8)
Au	- W	- C(2)	105.6(3)	97.1(9)
Au	- W	- C(3)	49.9(2)	49.6(7)
Au	- W	- N(1)	124.0(2)	135.2(5)
Au	- W	- N(2)	150.1(2)	142.8(5)
Au	- W	- N(3)	85.3(2)	90.7(5)
C(1)	- W	- C(2)	85.9(3)	90.9(12)
C(1)	- W	- C(3)	105.0(3)	108.4(11)
C(1)	- W	- N(1)	167.9(3)	162.7(10)
C(1)	- W	- N(2)	88.7(3)	83.1(10)
C(1)	- W	- N(3)	95.5(3)	95.0(10)
C(2)	- W	- C(3)	78.7(3)	82.7(11)
C(2)	- W	- N(1)	96.7(3)	92.3(10)
C(2)	- W	- N(2)	87.3(3)	92.7(10)
C(2)	- W	- N(3)	168.6(3)	171.9(10)
C(3)	- W	- N(1)	87.2(3)	88.9(9)
C(3)	- W	- N(2)	159.5(3)	167.5(9)
C(3)	- W	- N(3)	111.8(3)	100.8(9)
N(1)	- W	- N(2)	79.6(2)	79.7(7)
N(1)	- W	- N(3)	79.6(2)	80.5(7)
N(2)	- W	- N(3)	81.4(2)	82.5(7)
W	- Au	- S	73.3(0)	74.1(2)
W	- Au	- P	154.6(1)	151.7(2)
W	- Au	- C(1)	42.2(2)	43.0(6)
W	- Au	- C(3)	42.5(2)	42.4(6)
S	- Au	- P	131.8(1)	134.3(3)
S	- Au	- C(1)	104.9(2)	114.4(7)
S	- Au	- C(3)	30.8(2)	31.7(7)
P	- Au	- C(1)	119.3(2)	109.9(7)
P	- Au	- C(3)	162.1(2)	166.0(7)
C(1)	- Au	- C(3)	78.0(3)	83.9(9)
Au	- S	- C(3)	42.8(3)	43.9(9)
Au	- P	- C(41)	109.1(3)	115.3(14)
Au	- P	- C(51)	114.1(3)	111.3(12)
Au	- P	- C(61)	114.1(3)	113.9(14)
C(41)	- P	- C(51)	106.5(4)	103.8(18)
C(41)	- P	- C(61)	106.8(4)	108.5(20)

[a]The estimated standard deviations in the parentheses are for the least significant digits.

Table 15 (Continued)

		3	4
C(51)- P	- C(61)	105.8(4)	102.8(18)
W	- C(1) - Au	71.7(2)	76.0(9)
W	- C(1) - O(1)	173.4(7)	169.6(24)
Au	- C(1) - O(1)	114.8(6)	114.3(20)
W	- C(2) - O(2)	178.2(8)	178.3(27)
W	- C(3) - Au	87.6(3)	88.0(9)
W	- C(3) - S	165.9(5)	167.3(16)
Au	- C(3) - S	106.4(4)	104.4(12)
W	- N(1) - C(11)	130.5(5)	129.8(17)
W	- N(1) - N(11)	122.7(5)	122.9(15)
C(11)- N(1)	- N(11)	106.5(6)	106.9(20)
N(1) - C(11)-	C(12)	110.8(7)	111.6(24)
C(11)- C(12)-	C(13)	104.6(8)	104.4(25)
C(12)- C(13)-	N(11)	108.6(8)	109.5(26)
N(1) - N(11)-	C(13)	109.6(6)	107.0(21)
N(1) - N(11)-	B	120.4(6)	118.2(21)
C(13)- N(11)-	B	129.8(7)	133.8(24)
W	- N(2) - C(21)	129.7(6)	130.8(18)
W	- N(2) - N(21)	123.0(5)	117.7(16)
C(21)- N(2)	- N(21)	107.2(7)	111.4(22)
N(2) - C(21)-	C(22)	109.3(8)	108.7(26)
C(21)- C(22)-	C(23)	106.0(9)	107.8(28)
C(22)- C(23)-	N(21)	108.1(8)	106.1(27)
N(2) - N(21)-	C(23)	109.5(7)	105.8(22)
N(2) - N(21)-	B	120.6(6)	122.3(22)
C(23)- N(21)-	B	130.0(7)	131.9(25)
W	- N(3) - C(31)	132.3(5)	132.3(17)
W	- N(3) - N(31)	121.2(5)	119.9(14)
C(31)- N(3)	- N(31)	106.5(6)	107.8(19)
N(3) - C(31)-	C(32)	109.7(8)	111.8(22)
C(31)- C(32)-	C(33)	106.6(9)	104.1(23)
C(32)- C(33)-	N(31)	107.9(8)	110.3(24)
N(3) - N(31)-	C(33)	109.3(7)	105.9(20)
N(3) - N(31)-	B	121.7(6)	119.3(20)
C(33)- N(31)-	B	129.0(7)	134.5(23)
N(11)- B	- N(21)	106.8(7)	112.5(23)
N(11)- B	- N(31)	107.7(7)	108.9(23)
N(21)- B	- N(31)	108.4(7)	108.8(23)
P	- C(41)- C(42)	117.7(6)	
P	- C(41)- C(46)	123.3(6)	
C(42)- C(41)-	C(46)	118.8(8)	

Table 15 (Continued)

	3	4
C(41)- C(42)- C(43)	121.0(8)	
C(42)- C(43)- C(44)	118.4(9)	
C(43)- C(44)- C(45)	120.1(9)	
C(44)- C(45)- C(46)	120.2(9)	
C(41)- C(46)- C(45)	121.6(9)	
P - C(51)- C(52)	123.1(7)	
P - C(51)- C(56)	118.7(7)	
C(52)- C(51)- C(56)	118.3(8)	
C(51)- C(52)- C(53)	120.3(10)	
C(52)- C(53)- C(54)	119.6(11)	
C(53)- C(54)- C(55)	120.9(11)	
C(54)- C(55)- C(56)	120.7(10)	
C(51)- C(56)- C(55)	120.2(9)	
P - C(61)- C(62)	122.0(7)	
P - C(61)- C(66)	117.0(8)	
C(62)- C(61)- C(66)	121.0(9)	
C(61)- C(62)- C(63)	116.9(10)	
C(62)- C(63)- C(64)	120.9(14)	
C(63)- C(64)- C(65)	121.2(16)	
C(64)- C(65)- C(66)	120.9(15)	
C(61)- C(66)- C(65)	119.0(12)	

detail. First we compare the structure of $[HB(pz)_3](CO)_2(CS)W\text{-}Au(PPh_3)$ with that of the closely-related $Cp(CO)_2W\text{-}Au(PPh_3)$,[5] in which two of the CO groups are semibridging. The W-Au bond distance (2.8248(4) A) in $[HB(pz)_3](CO)_2(CS)W\text{-}Au(PPh_3)$ is somewhat longer than those found in $Cp(CO)_3W\text{-}Au(PPh_3)$ (2.698(3) A) and $Cp(CO)_2W\text{-}Au(PPh_3)(\mu\text{-}CH(tolyl))$ (2.729(1) A).[27] Several features of the structure of $[HB(pz)_3](CO)_2(CS)W\text{-}Au(PPh_3)$ are consistent with the presence of a semibridging CO group. The W-C(2) bond distance (1.954(9) A) is shorter than W-C(1) (2.000(8) A), and the C(2)-O(2) bond distance (1.14(1) A) appears to be shorter than C(1)-O(1) (1.16(1) A). The W-C(2)-O(2) bond angle is 178.2(8)°, whereas the W-C(1)-O(1) bond angle (173.4(7)°) deviates more from 180°; the W-C(1)-O(1) bond angle is close to those (172(4), 168(4)°) of the semibridging carbonyls in $Cp(CO)_3W\text{-}Au(PPh_3)$. The Au-C(1)-O(1) bond angle, 114.8(6)°, is much smaller than that of W-C(1)-O(1) (173.4(7)°). The Au-C(1) bond distance is 2.720(8) A, which compares with the distances (2.51(5) A and 2.79(5) A) of the semibridging CO carbons to Au in $Cp(CO)_3W\text{-}Au(PPh_3)$. The bond distances of the semibridging CO carbons to Au in $(\eta^3\text{-}C_3H_5)(CO)_3Fe\text{-}Au(PPh_3)$ are 2.595(7) A and 2.569(7) A.[8] The Au-O(1) distance is 3.374(7) A, too long to be considered a side-on bonding CO.[28] Thus, C(1)-O(1) may be described as a semibridging CO group; the Au back-bonds to the semibridging CO ligand by donating electron density into the π^* orbitals

of CO, competing against π-back donation from the W atom. The geometry of the semibridging carbonyl ligand in $[HB(pz)_3](CO)_2(CS)W\text{-}Au(PPh_3)$ is similar to that in $(\eta^3\text{-}C_3H_5)(CO)_3Fe\text{-}Au(PPh_3)$,[8] $Cp(CO)_3W\text{-}Cu(PPh_3)_2$,[29] and $Cp(CO)_2W(\mu\text{-}C(tolyl)=CH_2)Pt(PMe_3)_2$.[30] Although the 14-electron gold(I) center has been considered a poor π-electron donor,[31] the much shorter Au-C(1) distance in the PMe_3 (2.55(3) A) compound, $[HB(pz)_3](CO)_2(CS)W\text{-}Au(PMe_3)$, as compared with the PPh_3 (2.720(8) A) complex, $[HB(pz)_3](CO)_2(CS)W\text{-}Au(PPh_3)$, strongly supports the idea that Au donates electron density into the CO π^* orbitals.

The CS ligand in $[HB(pz)_3](CO)_2(CS)W\text{-}Au(PPh_3)$ is also in a semibridging position; the Au-S distance is 3.054(2) A, long for a side-on bonding CS. As in terminal and C-bridging CS complexes, CS behaves as if it were a better σ-donor and π-acceptor ligand than CO. Thus, the W-C(3) bond distance (1.911(7) A) is shorter than both the W-C(1) (2.000(8) A) and W-C(2) (1.954(9) A) bond distances; it is also somewhat shorter than the W-C bond distance (1.94(2) A) to the terminal CS in $(CO)_4(CNC_6H_{11})W(CS)$,[32] although this is a much less electron-rich system. The W-C(3)-S bond angle (165.9(5)°) deviates significantly from 180° and is smaller than that of W-C(1)-O(1) (173.4(7)°) but is similar to those of the semibridging carbonyls in $Cp(CO)_3W\text{-}Au(PPh_3)$ (168(4)°, 172(4)°).[33] The M-C-O angles in other semibridging CO compounds[28-30,33-36] range from 154° (MnPt(μ-

$CS)(CS)_2(PMePh_2)_2Cp)$[37] to 177° $(\eta^3\text{-}C_3H_5)(CO)_3Fe\text{-}Au(PPh_3)$.[8] The Au-C(3) distance (2.162(7) A) is longer than the Au-C(sp) single bond distance (1.94(2) A) in (i-propyl)$NH_2AuC{\equiv}CC_6H_5$,[38] the Au-C(sp^2) single bond distance (2.07(2) A) in $Ph_3PAuC_6F_5$,[39] and the Au-C(sp^3) single bond distance (2.12(3) A) in Ph_3PAuMe.[40] The Au-C(3)-S bond angle, 106.4(4)°, is much smaller than W-C(3)-S (165.9(5)°), as expected for a semibridging CS group. The Au-C(3) bond distance (2.162(7) A) is substantially shorter than the Au-C(1) bond distance (2.720(8) A), which is consistent with the better π acceptor ability of CS over CO.[41] It is interesting that the Au-CS bond distance is essentially the same in $[HB(pz)_3](CO)_2(CS)W\text{-}Au(PPh_3)$ and $[HB(pz)_3](CO)_2(CS)W\text{-}Au(PMe_3)$, whereas the Au-CO distance is considerably shorter in the complex $[HB(pz)_3](CO)_2(CS)W\text{-}Au(PMe_3)$. This suggests that the semibridging CS ligand is less capable of accepting the additional electron density in $[HB(pz)_3](CO)_2(CS)W\text{-}Au(PMe_3)$, whereas the Au-CO bond is considerably strengthened by it.

The C(3)-S bond distance (1.630(8) A) is longer than those of other terminal CS ligands (1.50 - 1.59 A);[32,42] this lengthening presumably results from the donation of electron density from the Au to the π^* orbitals of CS. The C(3)-S bond distance is even longer than those of the C-bridged CS ligands in $[CpFe(CS)(CO)]_2$ (avg. 1.590(8) A)[43] and $Cp_2Fe_2(CO)_3CS$ (avg. 1.601(9) A).[44]

The W-Au-P bond angle (154.6(1)°) deviates noticeably from the 180° found in most Au(I) complexes,[37-39] and is substantially smaller than that found in $Cp(CO)_3W$-$AuPPh_3$ (173.8(3)°). If one assumes Au to prefer linear coordination and one of its ligands is the phosphine, the second ligand should lie on an extension of the P-Au vector. It is interesting that this extension intersects the W-C(3) bond at about its midpoint; however, it is not clear what significance this has for the bonding in the semibridging CS complexes. The Au atom adopts an approximately planar geometry; the W atom deviates (0.8 A) from the least-squares plane, defined by Au, P, C(1), and C(3). The interplanar angle between W-C(1)-Au and W-C(3)-Au is 138° and 161° in $[HB(pz)_3](CO)_2(CS)W$-$Au(PPh_3)$ and $[HB(pz)_3](CO)_2(CS)W$-$Au(PMe_3)$, respectively. The C(1)→O(1) bond vector lies in the W-C(1)-Au plane (within 0.03°) in $[HB(pz)_3](CO)_2(CS)W$-$Au(PPh_3)$, but is out of this plane slightly (2.04°) pointing toward the semibridging CS in $[HB(pz)_3](CO)_2(CS)W$-$Au(PMe_3)$. The C(3)→S bond vector points away from the W-C(3)-Au plane toward the semibridging CO in both $[HB(pz)_3](CO)_2(CS)W$-$Au(PPh_3)$ (2.29°) and $[HB(pz)_3](CO)_2(CS)W$-$Au(PMe_3)$ (2.76°).

The geometry around the W atom can be viewed as a distorted pentagonal bipyramid; C(2) and N(3) are in the axial positions, and Au, C(1), C(3), N(1), and N(2) are in the equatorial plane. The angle C(2)-W-N(3) is 168.6° and 171.9° in $[HB(pz)_3](CO)_2(CS)W$-$Au(PPh_3)$ and

$[HB(pz)_3](CO)_2(CS)W-Au(PMe_3)$, respectively. The angles L(axial)-W-L(equatorial) range from 79-112°, where L represents ligands including Au. This 7-coordination geometry, distinctly different from either capped octahedral or capped trigonal prismatic structure, has also been observed in other $[HB(pz)_3]$ complexes such as $[HB(pz)_3](CO)_2W[\eta^2\text{-}CH(SMe)]^+$, $[HB(pz)_3](CO)_2W[\eta^2\text{-}CH(SMe)(PPh_2)]$, and $[HB(pz)_3](CO)_2Mo[\eta^2\text{-}COR]$ (R = Ph, Me),[45] in which the L(ax)-M-L(ax) angles range from 171.4° to 176.7° and the L(ax)-M-L(eq) angles vary from 72.6° to 109.3°.

In conclusion, CS is a better semibridging ligand than CO as suggested by the fact that the CS instead of a second CO is involved in semibridging in $[HB(pz)_3](CO)_2(CS)W-Au(PPh_3)$ and $[HB(pz)_3](CO)_2(CS)W-Au(PMe_3)$. This conclusion is supported by the much shorter Au-C distance for Au-CS than Au-CO. The more favorable semibridging ability of the CS group appears to be due to its better π^*-acceptor ability as compared with CO, which allows it to interact more strongly with the π-donating Au atom.

REFERENCES

1. Kim, H. P. Ph.D. Dissertation, Iowa State University: Ames, Iowa, 1986.

2. Dombek, B. D.; Angelici, R. J. Inorg. Chem. 1976, 15, 2397.

3. (a) Dombek, B. D.; Angelici, R. J. J. Am. Chem. Soc. 1975, 97, 1261. (b) Greaves, W. W.; Angelici, R. J. Inorg. Chem. 1981, 20, 2983.

4. Greaves, W. W.; Angelici, R. J. J. Organometal. Chem. 1980, 191, 49.

5. Wilford, J. B.; Powell, H. M. J. Chem. Soc. A 1969, 8.

6. Mannan, Kh. A. I. F. M. Acta Crystallogr. 1967, 23 649.

7. Blundell, T. L.; Powell, H. M. J. Chem. Soc. A 1971, 1685.

8. Simon, F. E.; Lauher, J. W. Inorg. Chem. 1980, 19, 2338.

9. Indexings of the crystals were done using the program BLIND (Jacobson, R. A. J. Appl. Crystallogr. 1976, 9, 115). Structure factor calculations and least squares refinements were done using the program ALLS (Lapp, R. L.; Jacobson, R. A. U.S. Department of Energy Report IS-4708; Iowa State University: Ames, Iowa, 1979). Fourier series calculations were done using the program FOUR (Powell, D. R.; Jacobson, R. A. U.S. Department of Energy Report IS-4737; Iowa State University: Ames, Iowa, 1980). Patterson Harker analyses were done using the program ALCAMPS (Richardson, J. W. Jr.; Kim. S.; Jacobson, R. A. U.S. Department of Energy Report IS-4902; Iowa State University: Ames, Iowa, 1986), and for molecular drawing the program ORTEP (Johnson, C. K. U.S. Atomic Energy Commission Report ORNL-3794; Oak Ridge National Laboratory: Oak Ridge, Tenn., 1970) was used. An empirical absorption correction was carried out using diffractometer ψ-scan data.

10. Cromer, D. T.; Waber, J. T. In "International Tables for X-ray Crystallography"; Kynoch Press: Birmingham, England, 1974; Vol. IV, Table 2.2A, pp 71-79. Templeton, D. H. In "International Tables for X-ray Crystallography"; Kynoch Press: Birmingham, England, 1962; Vol. III, Table 3.3.2.c, pp 215-216.

11. Semion, V. A.; Struchkov, Y. T. Zh. Strukt. Khim. 1968, 9, 1046.

12. Fischer, E. O.; Lindner, T. L.; Huttner, G.; Friedrich, P.; Kreissl, F. R.; Besenhard, J. O. Chem. Ber. 1977, 110, 3397.

13. Fischer, E. O.; Hollfelder, H.; Friedrich, P.; Kreissl, F. R.; Huttner, G. Angew. Chem., Int. Ed. Engl. 1977, 16, 401.

14. Greaves, W. W.; Angelici, R. J.; Helland, B. J.; Klima, R.; Jacobson, R. A. J. Am. Chem. Soc. 1979, 101, 7618.

15. (a) Davidson, J. L.; Shiralian, M.; Manojlovic-Muir, L.; Muir, K. W. J. Chem. Soc., Chem. Commun. 1979, 30. (b) Marsela, J. A.; Folting, K.; Huffman, J. C.; Caulton, K. G. J. Am. Chem. Soc. 1981, 103, 5596.

16. Manojlovic-Muir, L.; Muir, K. W. J. Organometal. Chem. 1979, 168, 403.

17. Kato, K. Acta Crystallogr. 1972, B28, 606.

18. de Gil, E. R.; Dahl, L. F. J. Am. Chem. Soc. 1969, 91, 3751.

19. Chong, K. S.; Retting, S. J.; Storr, A.; Trotter, J. Can. J. Chem. 1980, 58, 1080.

20. Churchill, M. R.; Youngs, W. J. Inorg. Chem. 1979, 18, 2454.

21. Forder, R. A.; Gale, G. D.; Prout, K. Acta Crystallogr. 1975, B31, 307.

22. Kojima, T.; Nachikawa, T. J. J. Phys. Soc. Jpn. 1957, 12, 680.

23. (a) Pierce, L.; Hayashi, M. J. Chem. Phys. 1961, 35, 479. (b) Sijima, T.; Tsuchiya, S.; Kimura, M. Bull. Chem. Soc. Jpn. 1977, 50, 2564.

24. Pelizzi, C.; Pelizzi, G. Acta Crystallogr. 1979, B35, 1785.

25. Deviations from the least squares plane defined by W-S-C(3) are -1.436 and 1.722 A for the P and C(4) atoms, respectively.

26. Selected torsion angles (°) are: W-C(3)-P-C(41) -160.4; W-C(3)-P-C(51) 97.2; S-C(3)-P-C(41) -76.3; S-C(3)-P-C(51) -178.7; P-C(3)-S-W -122.6; P-C(3)-S-C(4) 132.4; W-C(3)-S-C(4) -105.0.

27. Carriedo, G. A.; Hodgson, D.; Howard, J. A. K.; Marsen, K.; Stone, F. G. A.; Went, M. J.; Woodward, P. J. Chem. Soc., Chem. Commun. **1982**, 1006.

28. Horwitz, C. P.; Shriver, D. F. Adv. Organomet. Chem. **1984**, 23, 219.

29. Carlton, L.; Lindsell, W. E.; McCullough, K. J.; Preston, P. N. J. Chem. Soc., Chem. Commun. **1983**, 216.

30. Barr, R. D.; Green, M.; Howard, J. A. K.; Marder, T. B.; Moore, I.; Stone, F. G. A. J. Chem. Soc., Chem. Commun. **1983**, 746.

31. (a) Graham, W. A. G. Inorg. Chem. **1968**, 7, 315. (b) Johnson, B. F. G.; Davis, R. In "Comprehensive Inorganic Chemistry"; Bailar, J. C., Ed.; Pergamon Press: Oxford, 1973; Vol. 3, Chapter 3. (c) Browning, J.; Goggin, P. L.; Goodfellow, R. J.; Norton, M. G.; Rattray, A. J. M.; Taylor, B. F.; Mink, J. J. Chem. Soc., Dalton Trans. **1977**, 2061.

32. Woodard, S. S.; Jacobson, R. A.; Angelici, R. J. J. Organomet. Chem. **1976**, 117, C75.

33. Morris-Sherwood, B. J.; Powell, C. B.; Hall, M. B. J. Am. Chem. Soc. **1984**, 106, 5079.

34. (a) Cotton, F. A. Prog. Inorg. Chem. **1976**, 21, 1. (b) Colton, R.; McCormick, M. J. Coord. Chem. Rev. **1980**, 31, 1.

35. Jeffery, J. C.; Sambale, C.; Schmidt, M. F.; Stone, F. G. A. Organometallics **1982**, 1, 1597.

36. Jeffery, J. C.; Moore, I.; Razay, H.; Stone, F. G. A. J. Chem. Soc., Chem. Commun. **1981**, 1255.

37. Jeffery, J. C.; Razay, H.; Stone, F. G. A. J. Chem. Soc., Dalton Trans. **1982**, 1733.

38. Corfield, P. W. R.; Shearer, H. M. M. Acta Crystallogr. **1967**, 23, 156.

39. Baker, R. W.; Pauling, P. Y. J. Chem. Soc., Dalton Trans. **1972**, 2264.

40. Gavens, P. D.; Guy, J. J.; Mays, M. J.; Sheldrick, G. M. Acta Crystallogr. 1977, B33, 137.

41. Butler, I. S. Acc. Chem. Res. 1977, 10, 359.

42. Bird, P. H.; Ismail, A. A.; Butler, I. S. Inorg. Chem. 1985, 24, 2911.

43. Dunker, J. W.; Finer, J. S.; Clardy, J.; Angelici, R. J. J. Organomet. Chem. 1976, 114, C49.

44. Beckman, D. E.; Jacobson, R. A. J. Organomet. Chem. 1979, 179, 187.

45. Curtis, M. D.; Shiu, K-B.; Butler, W. M. Organometallics 1983, 2, 1475.

SECTION IV

EXPLORATION OF PATTERSON SUPERPOSITON TO TWO INORGANIC CLUSTER COMPOUNDS WITH UNUSUALLY HIGH PSEUDO-SYMMETRY

INTRODUCTION

At present, the most commonly used methods of the X-ray crystal structure determination of small molecules are direct methods and Patterson methods. Direct methods[1] are based on the renowned probability relationships among reflection phases, such as the triple-phase and quartet relationships. There are various techniques and strategies involved in using these formulae to solve the phase problem. The general principle, however, is to determine the phases of the strongest reflections (e.g., $E \geq 1.2$) in terms of the phases of a few chosen reflections called the starting set. Once the phase propagation is complete, an iterative refinement of phases is applied and the validity of the solutions is then tested via a variety of measures before proceeding into Fourier syntheses. Various methods employ different algorithms to select the optimum starting set of reflections, and different strategy for phase propagation and for the testing of solutions. These algorithms have been computer-programmed and used in a reasonably automatic fashion with extensive employment of default parameters. The success of the methods on innumerable crystal structures brought scientific community-wide recognition of the achievement of the methods, as culminated in the winning of 1985 Nobel prize in chemistry by J. Karle and H. Hauptman. Direct methods, however, are very susceptible to false and catastrophic

starts. When the methods fail to a particular application, it is difficult to know what hinders the solution.

Patterson methods[2] have the advantage of easier and more physically meaningful approaches in the initial stages of phase determination. The use of Patterson or Patterson-derived functions offers potentially much greater flexibility than direct methods. In their initial stages, these methods require little or no knowledge of space group symmetry. However, as one proceeds one would like to incorporate space group or at least subspace group symmetry into the procedure to limit the number of independent atoms that must be sought, and to eliminate false atoms or images.

The Patterson superposition method, as such, requires only minimal a priori stereochemical information, and often provides correct stereochemical information as a result of the solution. Recent studies on Patterson superposition methods offer a systematic and automatic approach to the interpretation of the superposition functions.[3] One accomplishment was that multi-heavy atom structures can now be rather easily solved using these methods. When multiple heavy atoms exist in an asymmetric unit, interpreting the Patterson becomes either extremely difficult or at least cumbersome. Direct methods have been successfully applied in some of these cases, especially for of di- or tri-nuclear organometallic compounds and metal cluster compounds. The problem in these cases reduces to simple equal or near-equal

atom cases since one can ignore lighter atoms and concentrate on those heavy atoms. The remaining lighter atoms can then be easily located from the subsequent electron density maps just as ordinary heavy atom methods. However, solution of the structure via direct methods is often greatly hindered when pseudo-symmetry exists. Structures with pseudo-symmetry are difficult to solve via any type of method, but Patterson superposition methods uniquely reveal the nature of the pseudo-symmetry, and thus the solution via this method becomes manageable.

The research described herein involves structure determination of two inorganic compounds whose structural solutions were first attempted via direct methods without success, primarily due to pseudo-symmetry. The Patterson superposition methods were consistently applied successfully and revealed new insights into the phase problem. Details of these will be given in the following sections.

EXPERIMENTAL SECTION

Crystal data and relevent diffraction data are given in Table 1 for both compounds.

Data acquisition of $LiMo_8O_{10}$

As part of a quest for new types of molybdenum oxide strucutures, Kwang-Hwa Lii of Dr. McCarley's group at Iowa State University synthesized a highly reduced ternary molybdenum oxide and its Zn derivative.[4] Crystals of suitable size for diffraction work were discovered in a product mixture resulting from the reaction of Li_2MoO_4, MoO_3, and Mo in 3:8:13 mole ratio in a sealed Mo-tube at 1450°C for one and half days. The composition of the crystal was established through the subsequent X-ray structure determination. An essentially pure product was then prepared by heating a pressed pellet containing the required amounts of powdered Li_2MoO_4, MoO_3, and Mo (3:16:29 mole ratio) in a sealed Mo-tube at 1410°C for two days. This compound appears to be unreactive towards air and water over a periods of at least a few hours.

Oscillation and Weissenberg photographs revealed tetragonal crystal symmetry. Two conditions of systematic absences were noted from the photographs: $h+k+l = 2n+1$ and $2h+l = 4n$ for hkl and hhl reflections, respectively. There are two tetragonal space groups consistent with these

Table 1. Crystal data and relevant diffraction data for $LiMo_8O_{10}$, LIMO, and $4PPh_4 \cdot [O_2MoS_2FeS]_2 \cdot 3H_2O$, FEMO

	LIMO	FEMO
Formula unit	$LiMo_8O_{10}$	$Fe_2Mo_2S_6P_4C_{96}H_{92}O_{10}$
Crystal system	tetragonal	monoclinic
Space group	$I4_1md$	$P2_1/a$
a, A	5.8515(6)	15.808(6)
b, A	5.8515(6)	19.996(8)
c, A	24.783(3)	14.796(5)
β, °	90	101.75(9)
V, A^3	848.6(2)	4579.0(15)
Z	4	2
ρ_{calc}, g/cm^3	7.317	1.46
Crystal size, mm	0.2×0.14×0.08	0.2×0.2×0.03
μ, cm^{-1}	112.1	8.27
Ratio of T_{min}/T_{max}	0.49	0.80
λ, A	0.70926	0.70966
Diffractometer	AL	DATEX
ω-step scan mode	0.5 sec per 0.01° step	
Scan width, °	automatically	1.2
Background	5 sec at each side of scan	
$2\theta_{max}$, °	60	45
Octants measured	4	2
Reflections measured	2356	4254
Reflections observed	2156	2188
Cut off (I/σ_I)	3	2
Unique reflections	374	1816
R, Rw,[a] %	4.2, 5.2	7.0, 8.0%

[a] $R \equiv \Sigma||F_o|-|F_c||/\Sigma|F_o|$.
$Rw \equiv [\Sigma\omega(|F_o|-|F_c|)^2/\Sigma\omega|F_o|^2]^{1/2}$, $\omega = 1/\sigma_F{}^2$.

conditions, namely, $I4_1md$ (# 109) and $I\bar{4}2d$ (# 122), both being noncentrosymmetric. The exact unit cell contents were not known until completion of the structure determination and refinement. Estimating the number of molybdenum atoms in the unit cell prior to the structure determination was not plausible since the density of the crystal was rather high.

Data acquisition of $4PPh_4 \cdot [O_2MoS_2FeS]_2 \cdot 6H_2O$

The tetranuclear compound was synthesized by Bob Anglin of Dr. Kurtz's group at Iowa State University during the course of explorations of aqueous and enzyme-mediated assembly of biologically relevant Fe-S and Mo-Fe-S clusters.[5] The compound showed a novel absorption spectrum in aqueous solution and was isolated in ~40% yield as its hydrated Ph_4As^+ or Ph_4P^+ salt from high pH mixtures of $Fe^{2+}(aq)$ and $MoO_xS_{4-x}^{2-}$ (x = 0, 1, or 2). The Mossbauer spectrum is consistent with an oxidation state between Fe(II) and Fe(III) and with antiferromagnetic coupling between the two iron atoms in the anion. Isolation of this compound using MoS_4^{2-} demonstrates a phenomenon of obvious biological significance: Fe(II) greatly accelerates the hydrolysis of MoS_4^{2-}.

Crytals could only be obtained directly from the reaction mixtures without any recrystallizations and were of very poor quality and weakly diffracting. After exhaustive trial and error, a small plate-like crystal was chosen and

sealed inside of a glass capillary. The monoclinic cell noted in Table 1 was confirmed by the inspection of the symmetry in the axial oscillation photographs. However, it was not trivial to determine the space group based on systematic extinction conditions due to some ambiguities in 0k0 and h0l zones. The possible candidates for the space group were P2, Pm, $P2_1$, Pa, P2/m, P2/a, $P2_1/m$, and $P2_1/a$. Prior to this structural determination, no information on either elemental composition or density of the crystal was known. It was not possible to postulate a structural model except that the metal atoms were tetrahedrally coordinated by oxygen and/or sulfur bridges.

RESULTS

Structural solution of $LiMo_8O_{10}$

Representative sections of the Patterson map are shown in Figures 1, 2, and 3. Sections with W = 11, 21, 32, 43, and 54 in 32x32x64 UVW grids are very similar to the section 0, and sections 16, 27, 37, 48, and 59 to the section 5. The strongest peaks in the Patterson are labelled A through H in Figures 1 and 3. One can easily recognize that these peaks form octahedral patterns. The peaks at W = 0 such as A, B, C, and D in Figure 1 can form a waist of an octahedron, while the peaks at W = $\pm$5 (E, F, G, and H in Figure 3) form the apexes. It is also possible to form the waist using the peaks E, F, G, and H, and the apexes using the peaks A, B, C, D, and the similar ones at W = 11. The distances between the peaks A and B, between A and C, and between A and E, being about 2.93A, 2.93A, and 2.83A, respectively, are within the range of an Mo-Mo single bond distance. This suggests that the structure may have chains of edge-shared octahedra. If all the positions A through H and their equivalents were those of molybdenum atoms, there would have been a total of 48 of these and each oxygen atom would have been surrounded by six molybdenum atoms! This pattern is more likely then the results of superposition of several images of the structure.

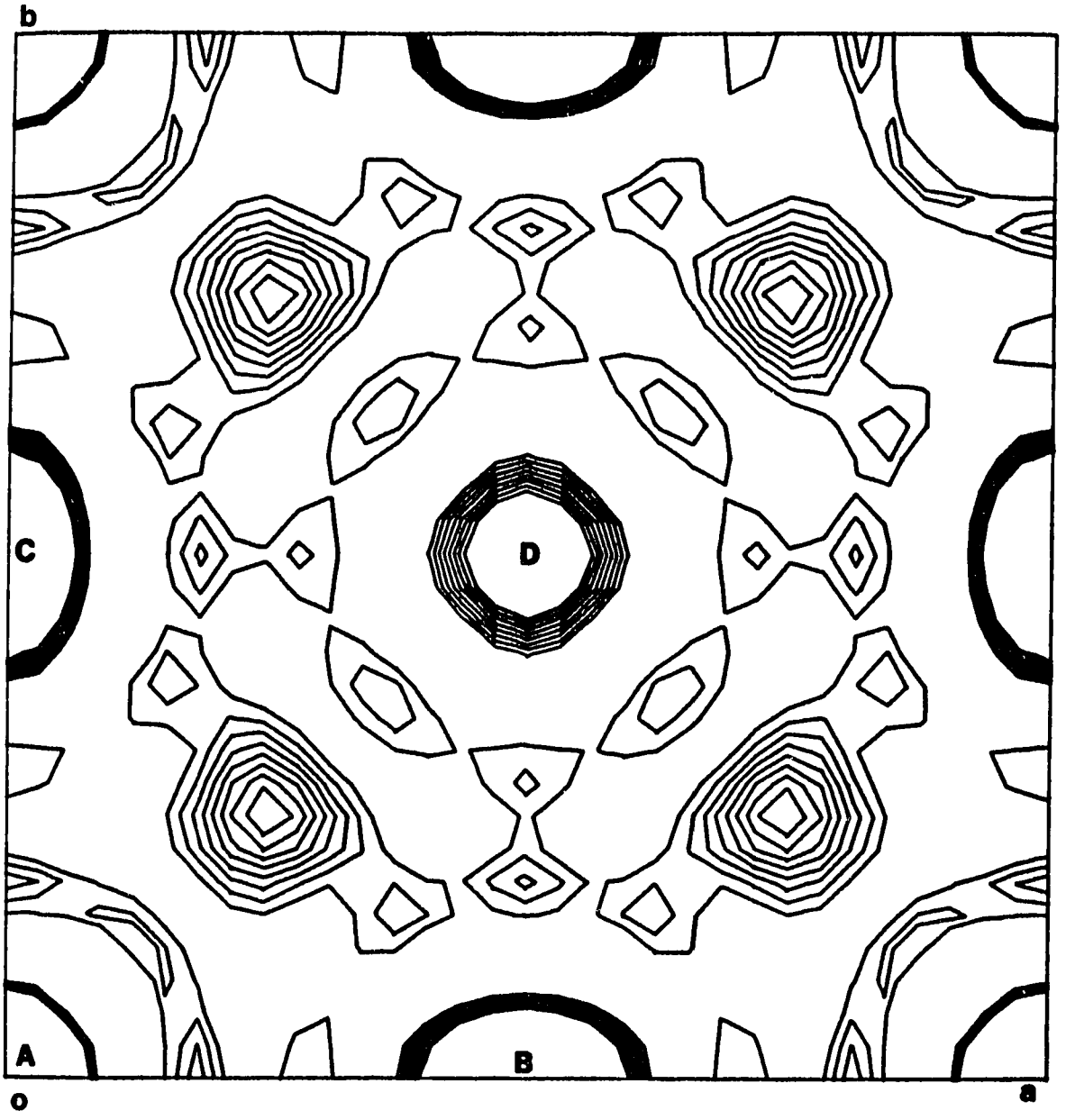

Figure 1. The section W = 0 of the Patterson map of LIMO. Contour levels start from 0 by steps of 10; lines beyond 80 are not drawn

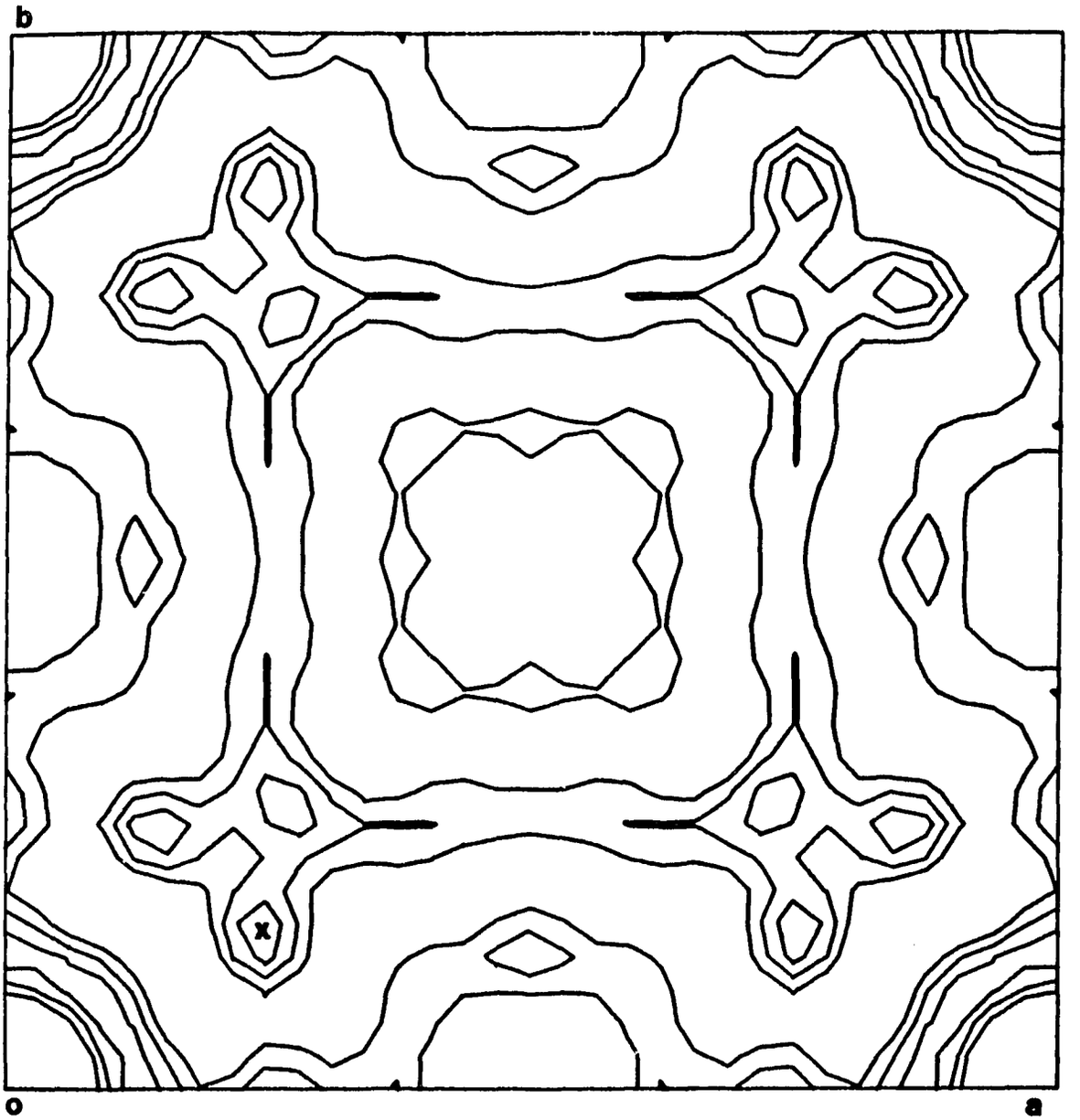

Figure 2. The section W = 2 of the Patterson map of LIMO. Contour levels are from 0 to 80 by steps of 10. The shift vector, (8, 4, 2) in 32×32×64 grids, used in the superposition analysis is marked by "X"

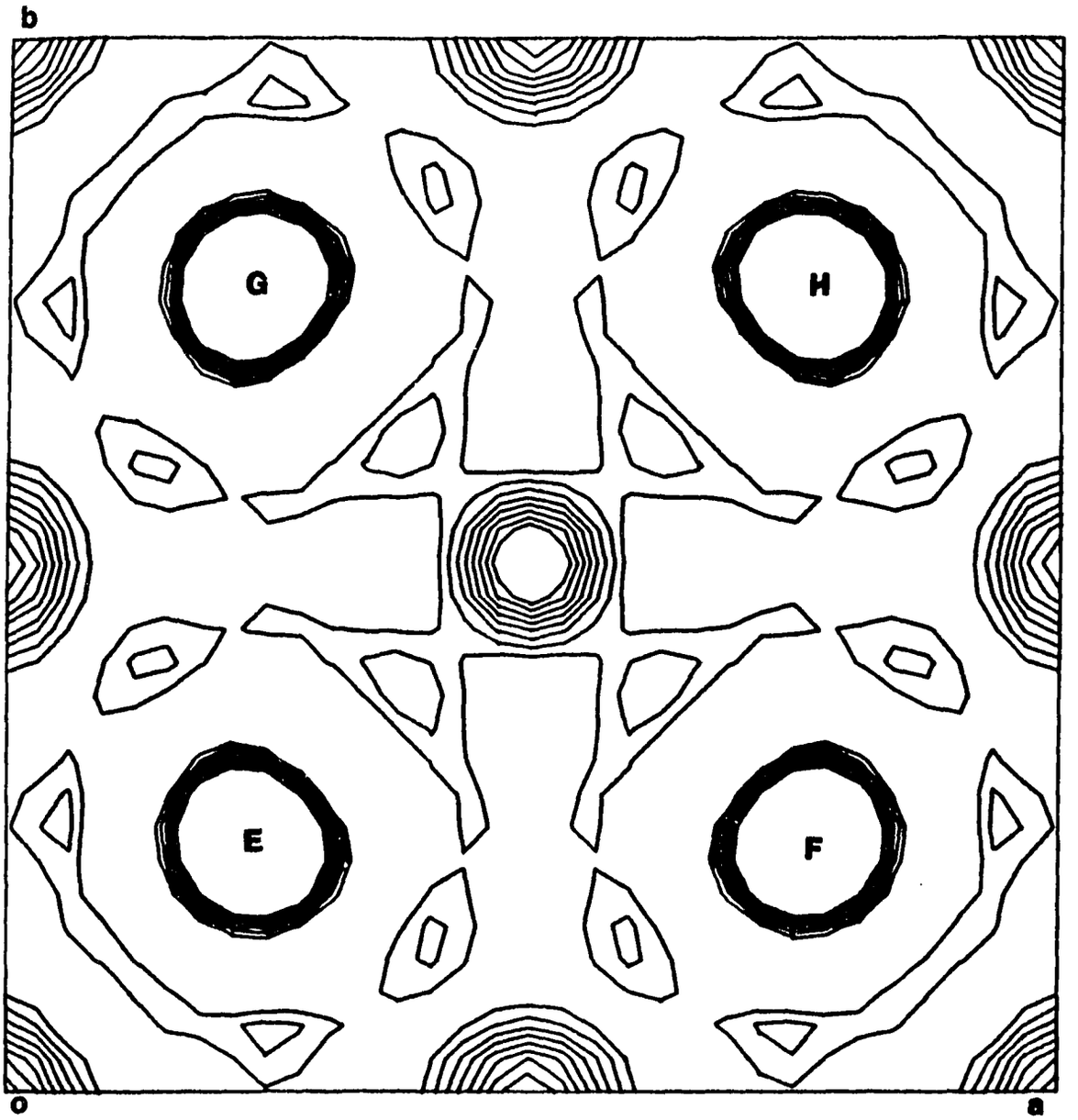

Figure 3. The section W = 5 of the Patterson map of LIMO. Contour levels are from 0 to 80 by steps of 10

One of the fundamental problems associated with this structure analysis is that based only on any conventional Patterson method such as vector verification,[6] one cannot tell the difference among the structural models: one with all 48 positions occupied by molybdenum atoms and others with only parts of them occupied. All these models give rise to the same sorts of Patterson peaks; thus, the Patterson peak height must also be considered along with the peak positions in interpreting the Patterson or Patterson-derived functions. Since there is no principal 4-fold axis in the space group $I4_1md$ or $I\bar{4}2d$, the waists of the octahedra do not have to be exact squares. In other words, the distance between A and B could be different from that between A and C in electron density space, while the small difference, if any, might not be detected in the Patterson map due to severe overlapping after the Patterson symmetry operations. This causes the problems connected with multiply-weighted Patterson vectors in the Patterson superposition analyses. For example, the AC vector is an overlap of 12 Mo-Mo vectors even excluding ones related by the body-centering operation, as it turned out. Also most of the peaks in the Patterson map are at, either exactly or accidentally, special positions known as Harker positions such as (1) U = V, (2) U and/or V = 0 or 1/2, and (3) W = 0 or 1/2 in fractional cell coordinates. In fact as found later, all the atoms, not only the molybdenum atoms but also oxygen and lithium atoms, in the structure are at

special positions.

Since all efforts failed to solve the structure with these special peaks as the shift vectors in Patterson superpositions, peaks at general positions in the Patterson function were sought. The highest of these were at U ≈ 8, V ≈ 4, W ≈ 2 in 32×32×64 grids and its symmetry-related positions, as marked by "X" in Figure 2. A total of 316 peaks out of 1216 Patterson peaks survived the superposition process with this peak. There were 40 peaks distinct enough in height to warrant special attention. Most of them formed octahedral chains. Some of them, such as peak numbers 16, 27, 31, and 35, were ignored because they did not form a complete octahedral chain. Symmetry elements relating one chain to another, and the origin of the unit cell were sought. Two of the results are shown in Table 2 for the space groups $I4_1md$ and $I\bar{4}2d$. The former yielded four symmetry-unique molybdenum atoms, while the latter yielded two. Separate structure factor calculations and isotropic refinement of the Mo atoms converged to R = 19.2%, Rw = 24.9% for the former, and R = 16.9%, Rw = 25.0% for the latter. Subsequent difference electron density calculations yielded positions of the remaining oxygen and lithium atoms. Anisotropic refinements of the former were converged to R = 4.2%, Rw = 5.2% after including an isotropic secondary extinction parameter, while those of the latter failed to yield positive definite temperature factors - the lowest

Table 2. Patterson superposition analysis for LIMO in space groups $I4_1md$ and $I\bar{4}2d$

#[a]	superposition			$I4_1md$	$I\bar{4}2d$
	U[b]	V	W	x,y,z	x,y,z
1	16.0	0.0	0.0	$1/2,y_1,0$	x_1,y_1,z_1
4	0.0	0.0	0.0	$0,y_2,z_2$	$1/2-x_1,y_1,3/4-z_1$
5	8.0	24.0	16.0	$y_1,0,1/4$	$y_1,1/2+x_1,1/4+z_1$
8	0.0	0.0	20.6	$0,y_3,z_3$	x_2,y_2,z_2
9	23.5	8.5	27.2	$-y_4,1/2,1/4+z_4$	$1/2+y_2,1/2-x_2,1/2-z_2$
12	8.0	8.0	16.0	$y_1,1/2,1/4+z_2$	$y_1,-x_1,-z_1$
13	8.5	8.5	27.2	$y_4,1/2,1/4+z_4$	$1/2-y_2,1/2+x_2,1/2-z_2$
16	16.0	16.0	11.4		
17	0.0	16.0	11.1	$0,-y_4,z_4$	$-x_2,1/2+y_2,1/4-z_2$
19	24.0	8.0	16.0	$-y_2,1/2,1/4+z_2$	$-y_1,x_1,-z_1$
21	16.0	16.0	0.0	$1/2,-y_1,0$	$-x_1,-y_1,z_1$
22	0.0	16.0	0.0	$0,-y_2,z_2$	$1/2+x_1,-y_1,3/4-z_1$
25	24.0	24.0	16.0	$-y_1,0,1/4$	$-y_1,1/2-y_2,1/4+z_1$
27	16.0	0.0	11.0		
30	0.0	0.0	10.5	$0,y_4,z_4$	$x_2,1/2-y_2,1/4-z_2$
31	16.0	16.0	21.5		
32	0.0	16.0	20.9	$0,-y_3,z_3$	$-x_2,-y_2,z_2$
35	23.6	23.5	27.2		
37	23.5	8.5	36.8	$-y_3,1/2,1/4+z_3$	$-y_2,1/2+x_2,1/4+z_2$
39	8.5	8.5	36.8	$y_3,1/2,1/4+z_3$	$y_2,1/2+x_2,1/4+z_2$

[a]Peaks are in the order of appearance in the superposition function. Body centering-related peaks are not included.

[b]U, V, and W are in the grid system of 32×32×64.

agreement was R = 15.4%, Rw = 20.2% with all atoms isotropic. Thus, the former was chosen as the correct structure. There was no significant difference between the two solutions since they were obtained from the same superposition peaks, and oxygen and lithium atoms also occupied the very same positions. Occupancy refinements indicated that all the atomic positions were fully occupied, establishing the stoichiometry as $LiMo_8O_{10}$.

The final atomic parameters are given in Tables 3 and 4. An ORTEP drawing of the structure is shown in Figure 4.

Structural solution of $4PPh_4 \cdot [O_2MoS_2FeS]_2 \cdot 3H_2O$

Initial attempts to solve the structure using either MULTAN80[7] or Patterson Harker analyses failed due primarily to pseudo-symmetry caused by repeating metal-metal vectors, as it turned out later. These vectors were also overlapped by sulfur-sulfur vectors. Although these vectors are not exactly equivalent, the differences were small enough to give rise to overlapped large Patterson peaks such as at (33.5, 32, 12), (32, 32, 0), (1.5, 0, 12), (3, 0, 24), and (35.5, 32, 24) in 64x64x64 grids, and at their monoclinic symmetry partners. The length of (1.5, 0, 12), 2.73A, is within the range of Fe-Fe, Fe-Mo, and Mo-Mo distances in sulfur bridged metal clusters. Notice that such a chain would be perpendicular to b axis. The existence of (3, 0, 24) in the

Table 3. The final positional parameters[a] ($\times 10^4$) for LIMO

atom[b]	x	y	z	U_{iso}[c]
Mo(1)	5000	2263(2)	0	7(0)
Mo(2)	0	2353(3)	43(1)	8(0)
Mo(3)	0	2480(3)	3281(1)	12(0)
Mo(4)	0	2760(3)	1755(1)	8(0)
O(1)	2540(23)	5000	0(11)	7(2)
O(2)	5000	2387(20)	811(7)	6(4)
O(3)	2695(23)	5000	1724(9)	13(4)
O(4)	0	2424(30)	855(11)	17(5)
O(5)	2372(22)	0	1644(9)	3(3)
Li	5000	5000	1306(16)	17(6)

[a]The estimated standard deviations in the parentheses are for the last significant digits.

[b]All the atoms have 1/2 site occupancy except Li which has 1/4.

[c]For anisotropically refined atoms, $U_{iso} \equiv 1/3 \Sigma U_{ij} \vec{a}_i^* \cdot \vec{a}_j^* a_i a_j$, where the temperature factors are defined as $\exp(-2\pi^2 \Sigma h_i h_j a_i^* a_j^* U_{ij})$ ($\times 10^3$).

Table 4. The final anisotropic thermal parameters[a] ($\times 10^3$) of the molybdenum atoms in LIMO

atom	U_{11}	U_{22}	U_{33}	U_{23}	U_{13}	U_{12}
Mo(1)	9(1)	9(1)	3(1)	2(1)	0	0
Mo(2)	8(1)	10(1)	6(1)	1(1)	0	0
Mo(3)	8(1)	25(1)	3(1)	0(0)	0	0
Mo(4)	9(1)	9(1)	5(1)	0(1)	0	0

[a]The estimated standard deviations in the parentheses are for the last significant digits.

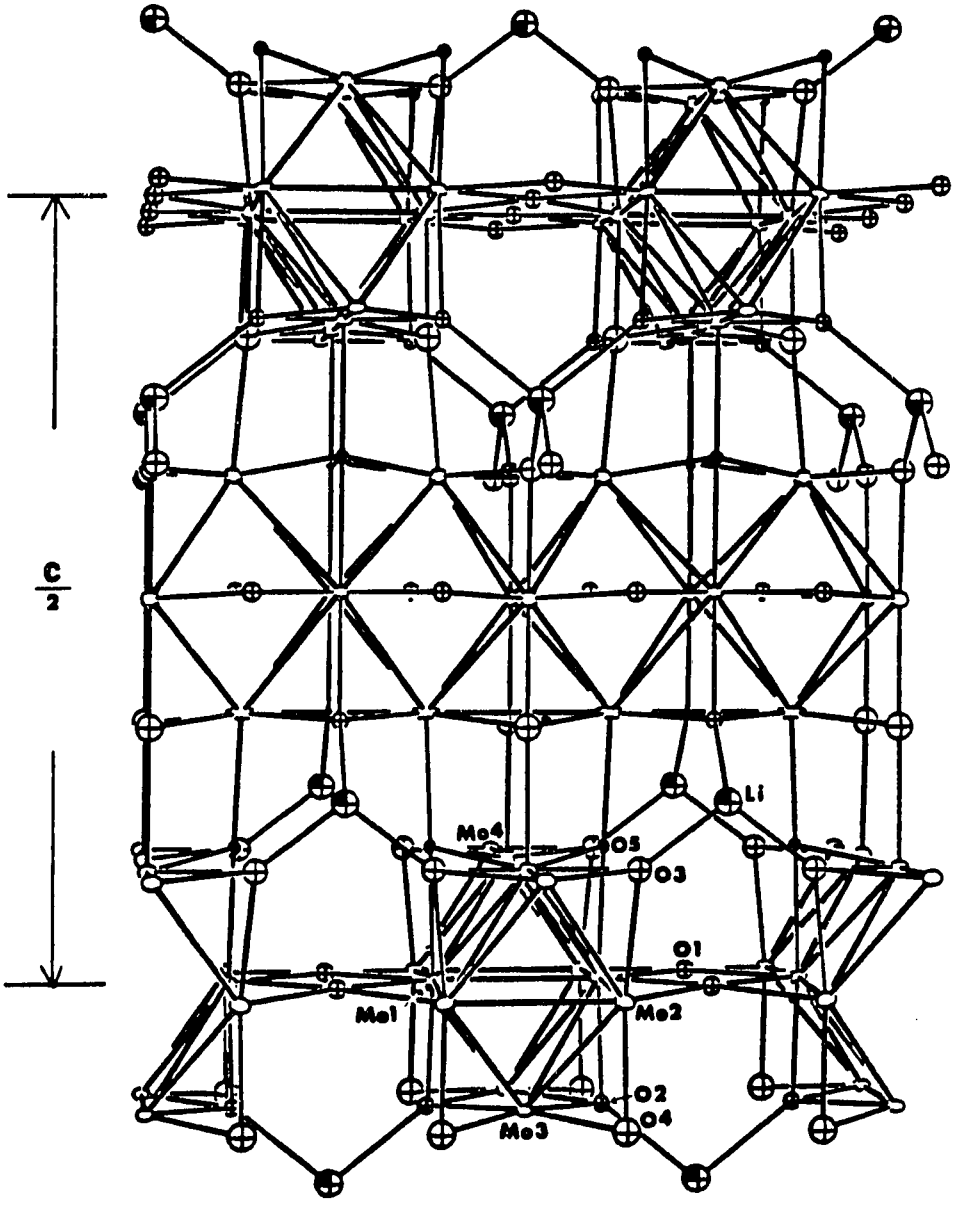

Figure 4. An ORTEP drawing of LIMO as viewed down the tetragonal a axis. Open ellipsoids are Mo, crossed spheres O, and shaded spheres Li

Patterson supports the possibility of linear chain of at least three metal atoms. Whether it can also be a tetranuclear linear chain depends on the existence of a peak at (4.5, 0, 36) if one assumes near linearity of the chain. The closest peak in the Patterson was at (5.3, 0, 36.6) with 27% of the peak height of (1.5, 0, 12)! This greatly hindered the choice of a tetramer model from initial considerations. However, Patterson superposition analysis (ALCAMPS) using a Mo-P interaction of 8.6A length as shift vector, readily gave rise to the seven strongest atomic positions - three metals in one chain and four metals in the other; the two chains are seperated by x = y = 1/2, resulting in the Patterson peak (32, 32, 0). They were compatible with both space groups Pa and $P2_1$; however, among these seven peaks, a different peak had to be considered as false in each case. Instead of excluding one peak, if a lower cutoff value for the symmetry checking in the ALCAMPS procedure was used, one can get a tetranuclear chain structure in the space group $P2_1/a$. In fact, the difference electron density maps obtained by assuming either of the other space groups contained a strong peak at the terminal of the trinuclear chain, forming the tetranuclear structure. The reason we missed the eighth peak in the superposition was that the chain deviated slightly from being linear as also seen in (5.3, 0, 36.6) $\neq$ 3x(1.5, 0, 12). Other lower peaks in the ALCAMPS result were interpreted as sulfur atoms. Positions

of these metal and sulfur atoms then served as the model structure; occupancy refinement established chemical identities of molybdenum and irons. Subsequent structure factor and electron density calculation revealed the remaining atoms of the compound. Three relatively strong residual densities isolated outside the molecular boundaries were assigned as oxygen atoms of the water molecules of crystallization, as based on the peak heights and occupancy factors refinement. Hydrogen atoms were included at the calculated fixed positions with C-H distances set to 1.0A. The least-squares refinement was carried out using a blocked full matrix method, minimizing $\Sigma\omega(|F_o|-|F_c|)^2$. After every three cycles of refinement, ω's were adjusted to reduce the variation of $\langle\omega(|F_o|-|F_c|)^2\rangle$ over divisions of both $|F_o|$ and $\sin\theta/\lambda$. The final residual indices were $R = \Sigma||F_o|-|F_c||/\Sigma|F_o| = 7.00$ % and $Rw = [\Sigma\omega(|F_o|-|F_c|)^2/\Sigma\omega|F_o|^2]^{1/2} = 8.01$ %. The final positional and thermal parameters are given in Tables 5 and 6, respectively, while ORTEP drawings of the tetranuclear chain and the countercation are shown in Figure 5.

Table 5. The positional parameters[a] ($\times 10^4$) and U_{iso}[b] ($\times 10^3$) of FEMO

Atom	x	y	z	U_{iso}
MO	4598(1)	-91(1)	2138(2)	75(0)
FE	4892(2)	-5(1)	4070(2)	60(1)
S1	5558(4)	-685(3)	3170(5)	74(2)
S2	3996(4)	637(3)	3005(5)	87(2)
S3	4185(4)	-612(2)	4933(5)	64(2)
P1	366(3)	1850(2)	8591(4)	38(1)
P2	4534(3)	6826(2)	6506(4)	38(1)
O1	3789(9)	-630(7)	1444(11)	81(5)
O2	5160(11)	359(8)	1446(12)	96(5)
O3	2296(9)	5238(7)	2215(11)	89(5)
O4	1480(11)	4586(8)	10469(13)	111(6)
O5	2112(13)	3341(10)	9595(15)	131(7)
C111	-89(14)	2544(9)	9117(16)	57(6)
C112	239(13)	2742(10)	10007(17)	64(7)
C113	-67(14)	3301(10)	10323(16)	66(7)
C114	-744(14)	3673(10)	9797(17)	66(6)
C115	-1079(15)	3450(12)	8935(18)	78(7)
C116	-796(13)	2895(10)	8554(16)	60(6)
C121	-525(12)	1376(9)	7913(14)	45(5)
C122	-1223(14)	1230(10)	8313(16)	62(6)
C123	-1903(14)	841(11)	7777(18)	73(7)
C124	-1882(14)	664(10)	6878(16)	64(6)
C125	-1203(18)	817(13)	6498(20)	97(9)
C126	-478(14)	1162(11)	7053(18)	73(7)
C131	1041(13)	2155(10)	7886(16)	61(6)
C132	964(12)	2842(9)	7542(14)	47(5)
C133	1461(13)	3042(10)	6926(16)	59(6)
C134	2044(15)	2655(11)	6660(17)	77(7)
C135	2130(14)	1974(11)	6961(17)	73(7)
C136	1638(14)	1745(10)	7561(17)	67(6)
C141	1025(13)	1341(10)	9543(15)	55(6)
C142	633(12)	863(9)	9929(14)	46(5)

[a]The estimated standard deviations in the parentheses are for the last significant digits.

[b]For anisotropically refined atoms, $U_{iso} \equiv 1/3\ \Sigma U_{ij}\vec{a}_i^*\cdot\vec{a}_j^* a_i a_j$, where the temperature factors are defined as $\exp(-2\pi^2 \Sigma h_i h_j a_i^* a_j^* U_{ij})$.

Table 5 (Continued)

Atom	x	y	z	U_{iso}
C143	1125(14)	555(10)	10721(16)	66(6)
C144	1967(15)	734(12)	11033(17)	80(7)
C145	2340(14)	1240(11)	10634(18)	74(7)
C146	1879(15)	1544(11)	9858(19)	77(7)
C211	3946(13)	7469(10)	6987(15)	59(6)
C212	4051(13)	8152(10)	6751(16)	63(6)
C213	3555(13)	8606(9)	7151(15)	55(6)
C214	3046(15)	8427(11)	7743(18)	74(7)
C215	2957(13)	7754(10)	7967(15)	65(6)
C216	3446(15)	7294(11)	7580(17)	73(7)
C221	3823(13)	6272(10)	5722(15)	52(6)
C222	4120(14)	5914(11)	5087(17)	68(7)
C223	3605(17)	5467(12)	4445(19)	88(8)
C224	2795(16)	5372(12)	4619(18)	80(7)
C225	2493(14)	5700(11)	5238(17)	69(7)
C226	2988(14)	6139(10)	5870(16)	69(7)
C231	5292(13)	7166(10)	5870(16)	61(6)
C232	4968(14)	7631(10)	5127(16)	59(6)
C233	5496(16)	7889(12)	4622(18)	84(8)
C234	6397(16)	7696(12)	4808(18)	88(8)
C235	6682(16)	7251(12)	5548(20)	86(8)
C236	6146(15)	6958(11)	6089(18)	76(7)
C241	5170(15)	6381(11)	7510(17)	73(7)
C242	5291(16)	5683(12)	7450(19)	89(8)
C243	5820(18)	5377(13)	8195(20)	93(8)
C244	6253(17)	5737(13)	8868(20)	92(8)
C245	6128(15)	6407(11)	8967(18)	75(7)
C246	5576(15)	6763(11)	8274(18)	76(7)

Table 6. The anisotropic thermal parameters[a] ($\times 10^3$) of FEMO

Atom	U_{11}	U_{22}	U_{33}	U_{23}	U_{13}	U_{12}
MO	59(1)	55(1)	97(2)	7(1)	-14(1)	-8(1)
FE	48(2)	46(1)	77(2)	5(2)	-9(2)	1(1)
S1	64(4)	44(3)	107(6)	3(3)	1(4)	-5(3)
S2	74(4)	66(4)	107(6)	0(4)	-15(4)	25(3)
S3	55(3)	46(3)	81(5)	-3(3)	-9(3)	-3(3)
P1	25(3)	24(2)	59(4)	0(3)	-6(3)	-4(2)
P2	21(3)	24(2)	62(4)	5(3)	-9(3)	-7(2)

[a]The estimated standard deviations in the parentheses are for the last significant digits.

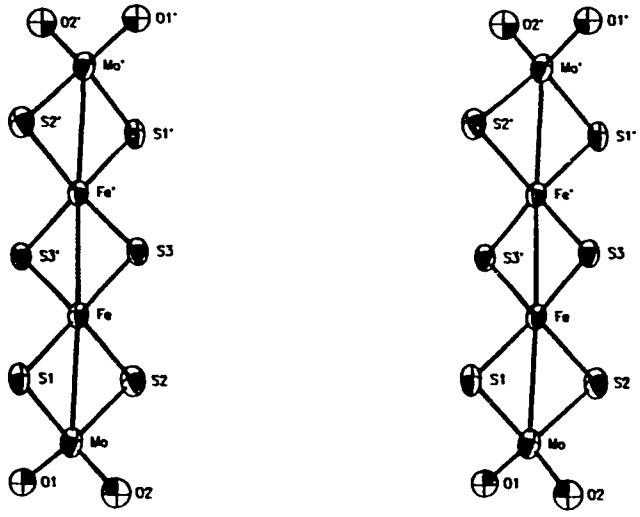

Figure 5. An ORTEP drawing of FEMO: (a) the anion with an inversion point in the middle of Fe-Fe bond, and (b) stereoview showing a best molecular fit between two independent PPh_4^+ cations. Ring 1 involves atoms C(111)-C(116) and C(241)-C(246), ring 2 C(121)-C(126) and C(211)-C(216), ring 3 C(131)-C(136) and C(231)-C(236), and ring 4 C(141)-C(146) and C(221)-C(226)

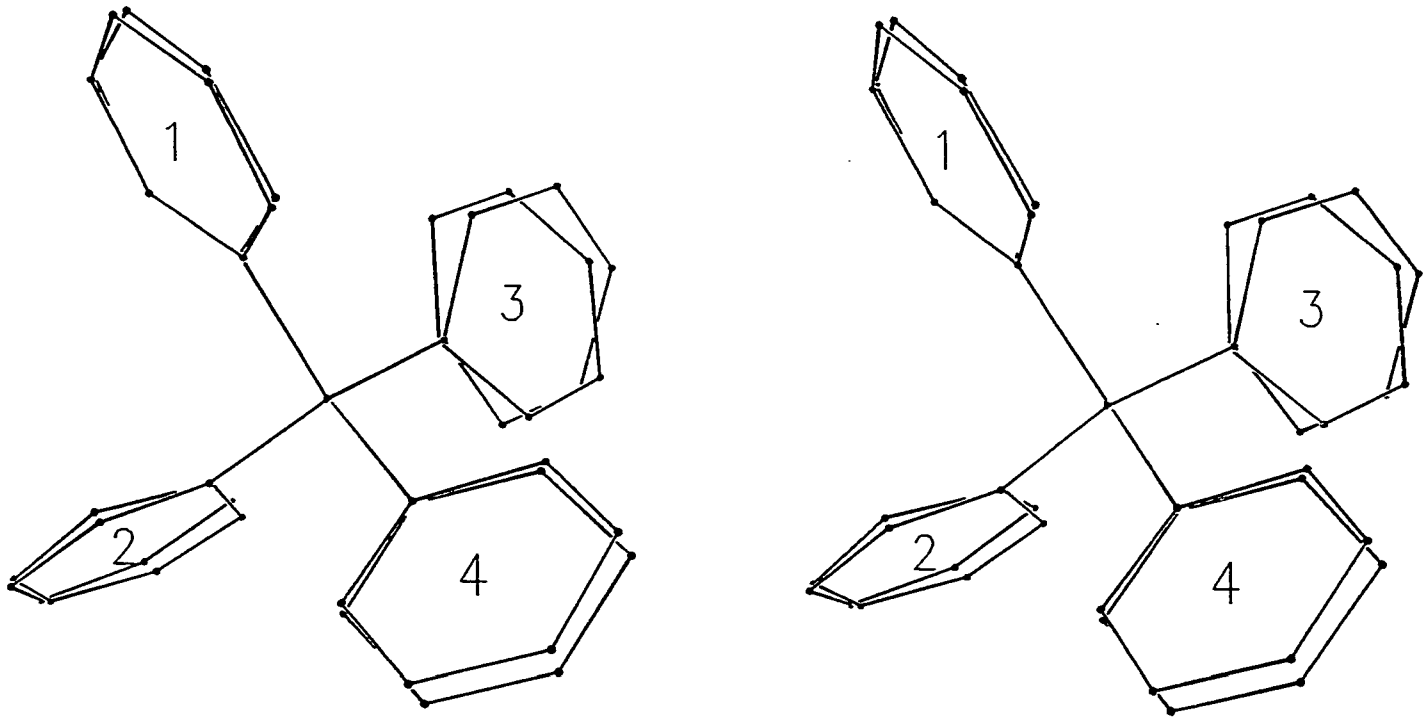

Figure 5 (Continued)

DISCUSSION

Once a structure has been determined, it is always informative, especially for difficult structures such as these two, to go back to the Patterson and superposition map and to examine why the structural solution had been hindered and exactly what helped the solution. In both sturucture solutions, we started out with the strongest Patterson peak as the shift vector, and the resultant map still contained multiple images of the structures. One way to deconvolute these is, at least in principle, by performing multiple superpositions. An alternative to this is by calculating weighted superpositions using relatively less overlapped peaks. The latter were chosen and were successful in both cases. Ordinarily, low-overlap peaks are found in general positions away from Harker sections. Even if not a Harker, a peak parallel or perpendicular to a symmetry axis or plane must be avoided in analyses relying on symmetry checking such as the ALCAMPS procedure. This can be easily rationalized by considering a hypothetical two-dimensional structure containing a two-fold axis as shown in Figure 6. Ideally, a superposition result contains two images of the structure related by an inversion point located in the middle of the shift vector. Figure 6 shows the superposition results arising with various shift vectors. To sort out the single image of the structure, the ALCAMPS procedure utilizes

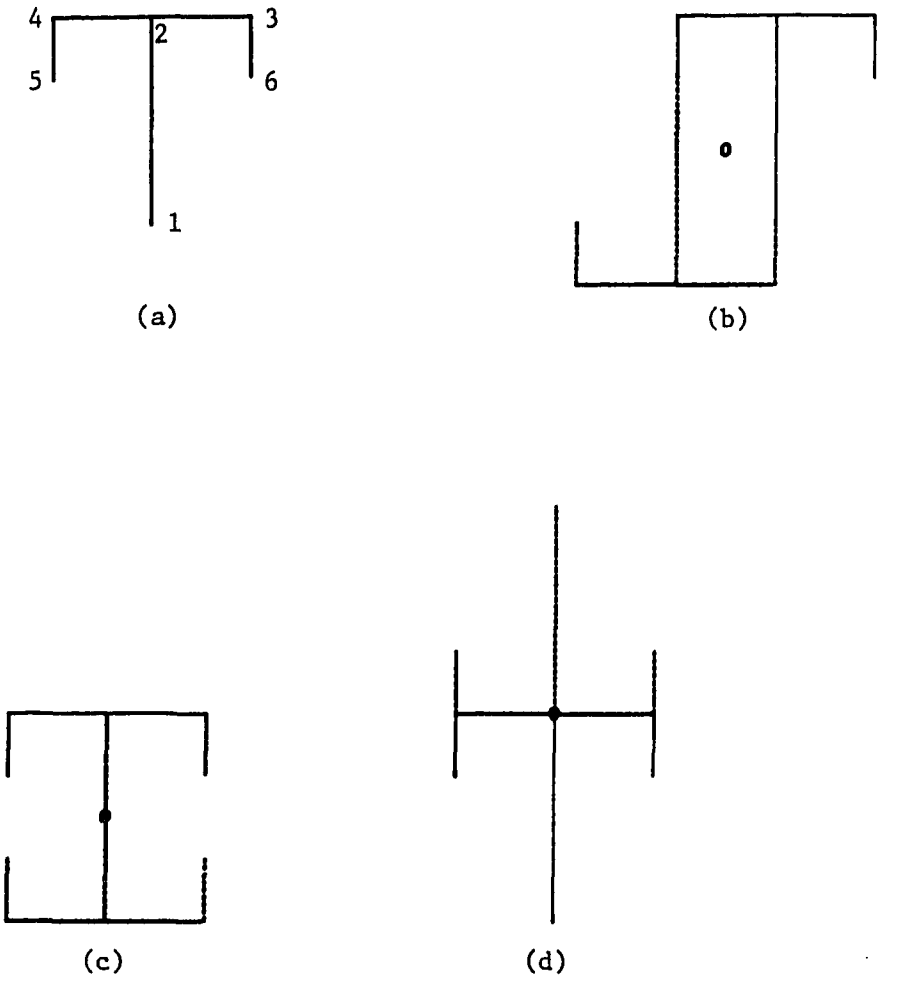

Figure 6. A hypothetical Patterson superposition results: (a) the original structure, superposition results showing double images via shift vectors (b) 1→5, (c) 1→2, (d) 3→4, (e) 3→6, (f) 4→5, (g) 2→3, (h) 2→4, and quadruple images (i) as sum of (e) and (f), and (j) as sum of (g) and (h)

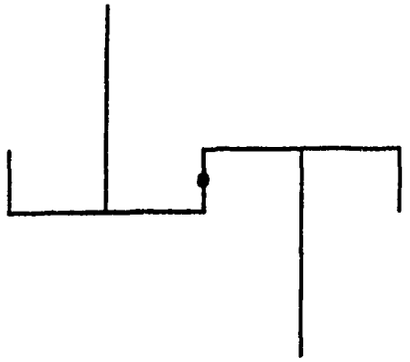

(e)

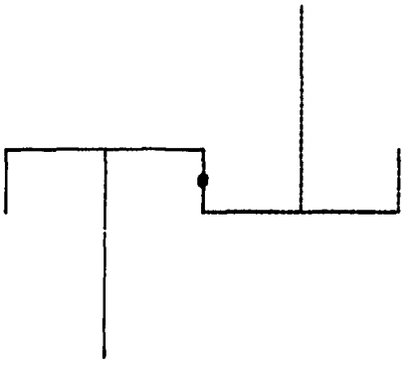

(f)

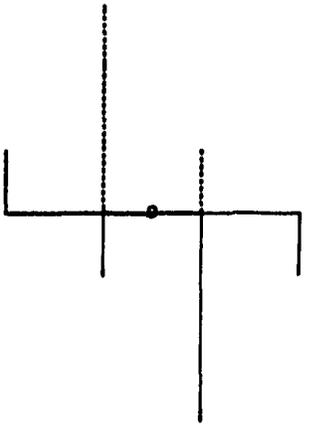

(g)

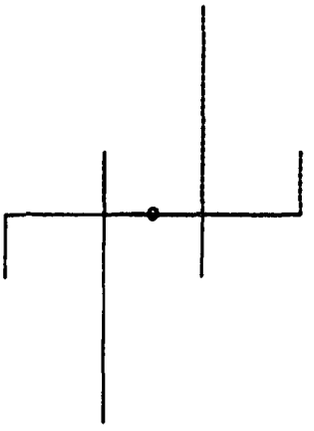

(h)

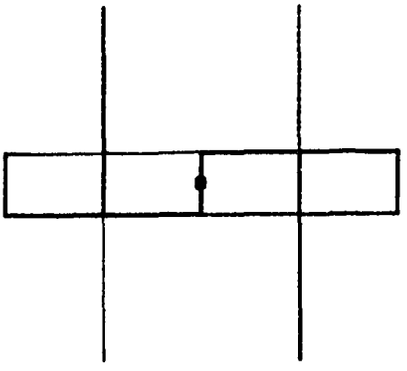

(i)

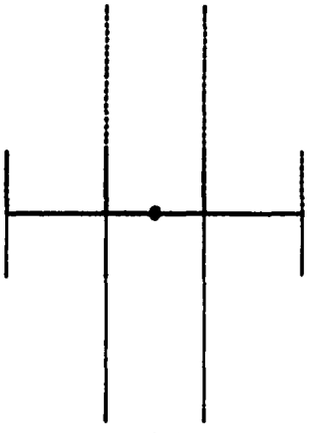

(j)

Figure 6 (Continued)

symmetry information: by locating the symmetry element in the superposition, false atoms which do not have necessary symmetry partners can be eliminated from the list. This process can eventually produce a single image and a few extra peaks. However, this method obviously does not work for the cases shown in Figure 6(c)-(h), where the shift vectors are either parallel or perpendicular to the two-fold axis. The only case it works for is shown in Figure 6(b), where the shift vector is neither parallel nor perpendicular to the two-fold axis. Similar demonstrations can be worked out with both higher fold axis and mirror plane symmetry.

For the $LiMo_8O_{10}$ strucuture, the origin of the electron density space was at (0, -8, 0) in the superposition space, one only needs to subtract (0, -8, 0) from the shift vector to get the electron density positions of the tail and head of the shift vector. At tail of the vector, (0, -8, 0), there was a molybdenum atom whereas there was no atom at the head of the vector, (8, 12, 2), and the distance to a nearby molybdenum atom at (16, 8, 0) was too short for it to be a real atom. In fact none of the interatomic vectors were consistent with it. Hence both the regular and difference electron density maps were examined, and they are shown in Figure 7. In the regular map, one can see a small peak at (8, 12, 2), in contrast to the difference map which shows only very slight residual density there. What this means is that the small peak was a mere 'ripple'. If it was real

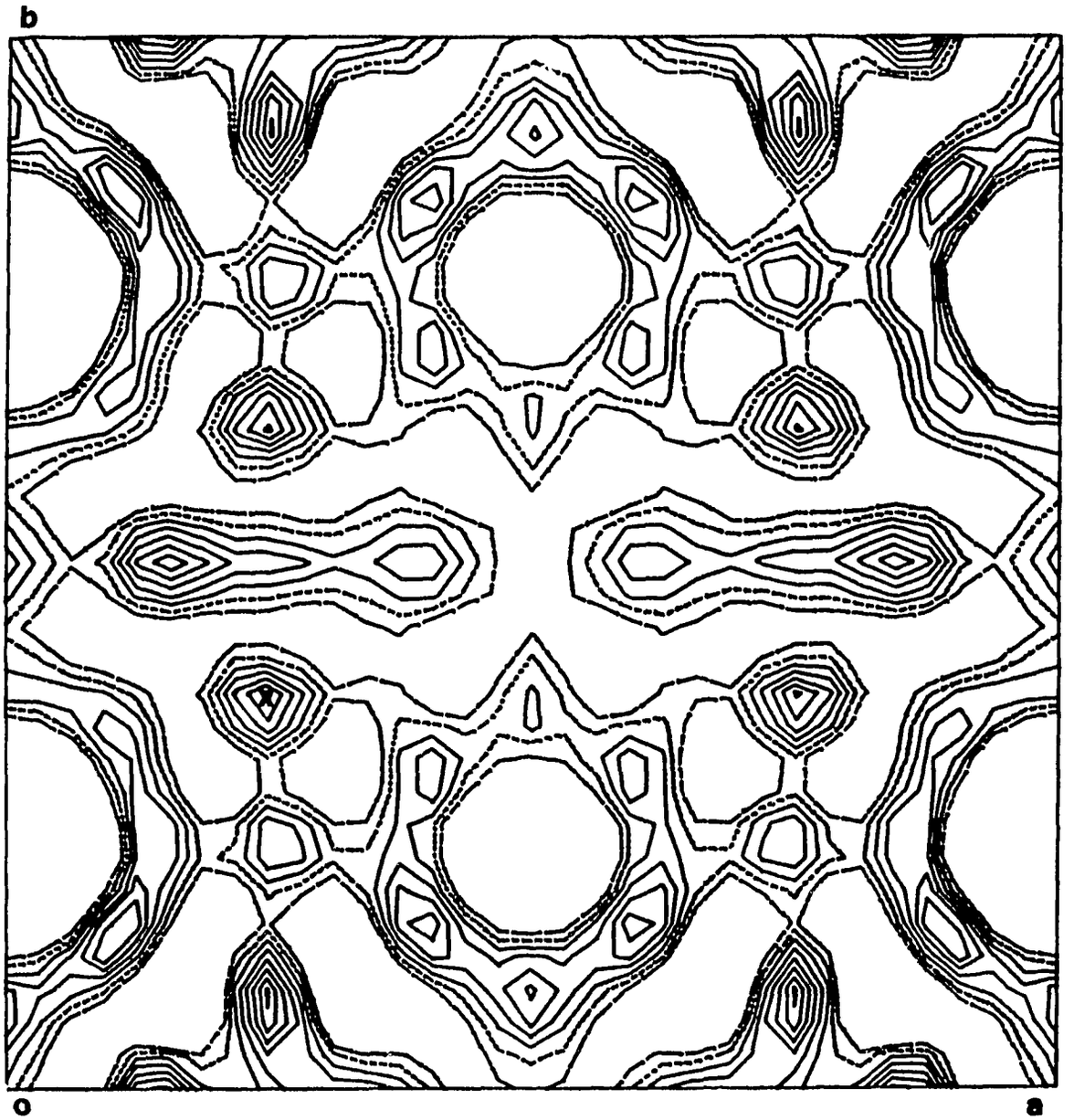

Figure 7. The section z = 2/64 of (a) the regular and (b) difference electron density maps of LIMO. Contour levels are from 0 to 80 by 10

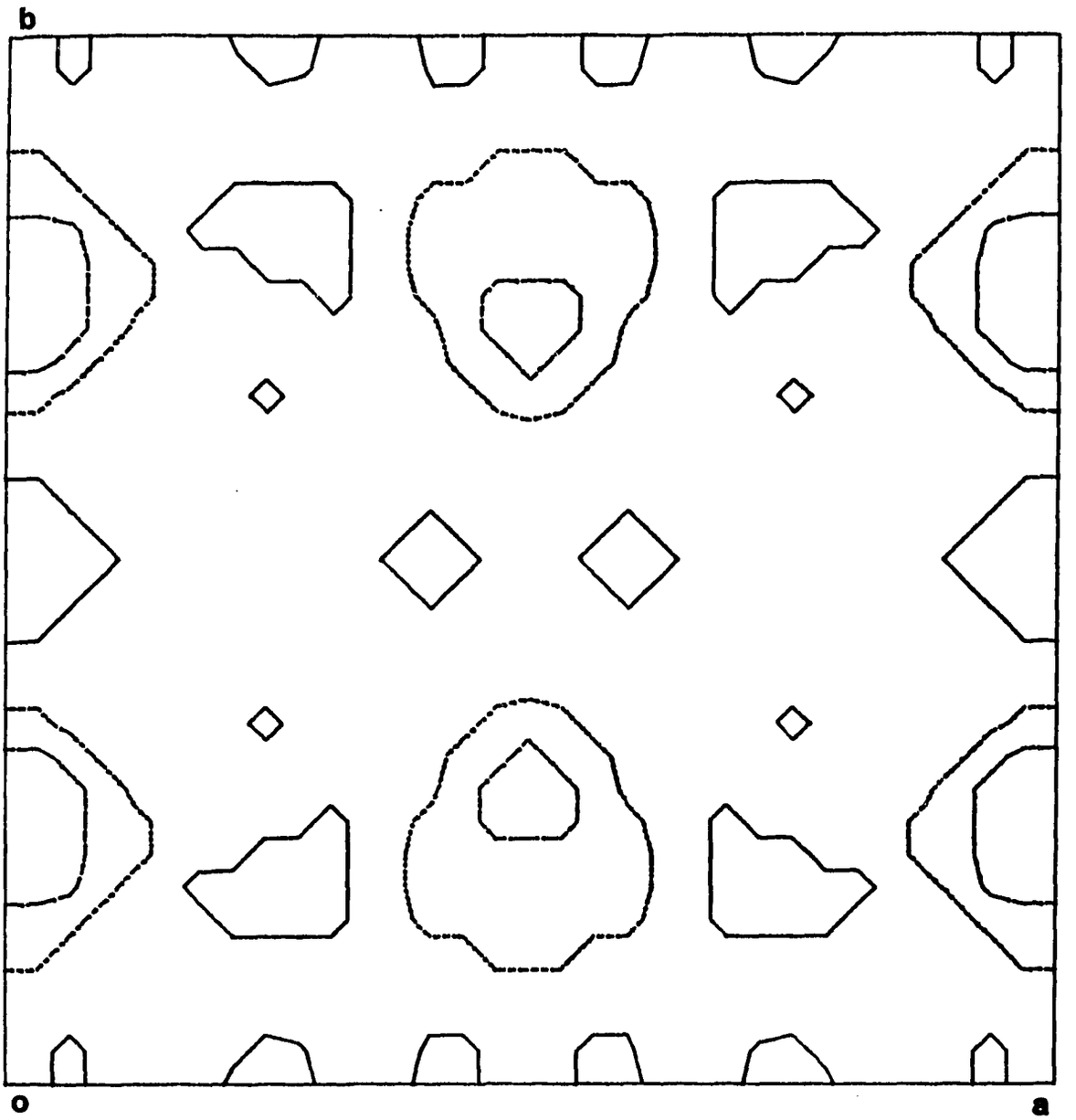

Figure 7 (Continued)

electron density which had contributed to the X-ray diffraction intensities, one should be able to see it also in the difference map since the atomic model of the structure did not include such localized electron density corresponding to such an atom. There still remains the intellectual problem: how can a ripple which is not real but arises due to termination error possibly produce a correct structure? This is indeed possible in a Patterson superposition analysis. Remember a Patterson function is a self-convolution of an electron density function. It can be written in a mathematical form as follows:

$$P(\vec{U}) = \frac{1}{V} \int \rho(\vec{r}+\vec{U})\rho(\vec{r})d\tau \qquad (1)$$

where the integration is over the unit cell volume. One can derive Eq. (1) from following equations. ρ and P can be written as Fourier series:

$$\rho(\vec{r}) = \frac{1}{V} \Sigma\ F(\vec{h})e^{-2\pi i\vec{h}\cdot\vec{r}} \qquad (2)$$

$$P(\vec{r}) = \frac{1}{V} \Sigma\ I(\vec{h})e^{-2\pi i\vec{h}\cdot\vec{r}} \qquad (3)$$

where the summations are over all the possible reflections $\vec{h}$, and F and I are given as:

$$F(\vec{h}) = \int \rho(\vec{r})e^{2\pi i\vec{h}\cdot\vec{r}}d\tau \qquad (4)$$

$$I(\vec{h}) = \int P(\vec{r})e^{2\pi i\vec{h}\cdot\vec{r}}d\tau \qquad (5)$$

Using $I(\vec{H}) = |F(\vec{H})|^2$, one can derive Eq. (1) from Eqs. (3) and (4). Since I and F are obtainable through experiments and subsequent analyses, one can get ρ and P using Eqs. (2) and (3), respectively. In practice, only a limited set of data is available and we carry out an approximation to these equations. Inevitably errors will accompany them, known as series termination or Gibbs' oscillation. An interesting feature in this case is that Eq. (1) still holds regardless of errors involved in steps (2) and (3). If spurious peaks are included in the electron density function, its convolution will also be seen in the Patterson function. One can utilize such vectors in a Patterson superposition analysis as with any other vectors and can obtain the structure in favorable situations. Note that the spurious peaks will remain in the result and they are recognizable through comparison of regular and difference electron density maps.

The theory presented here raises the possibility that ripples can be used to determine crystal structures via superposition-related techniques. A further application of the theory should be done with other crystal structures. The question arises: could one arbitrarily adjust the reflection data to enhance the Patterson image due to the ripple without appreciably disturbing the original structure?

REFERENCES

1. "Theory and practice of direct methods in crystallography". Ladd, M. F. C.; Palmer, R. A., Eds.; Plenum Press: New York, NY, 1980.

2. (a) Patterson, A. L. Z. Kristallogr. **1935**, 90, 517. (b) Jacobson, R. A. Trans. Am. Crystallogr. Assoc. **1966**, 2, 39. (c) Jacobson, R. A.; Beckman, D. E. Acta Crystallogr. **1979**, A35, 339. Egert, E. Acta Crystallogr. **1983**, A39, 936.

3. (a) Richardson, J. W., Jr. Ph.D. Dissertation, Iowa State University: Ames, Iowa 1984. (b) Richardson, J. W., Jr.; Kim, S.; Jacobson, R. A. "A program for computer-aided analysis of multisolution Patterson superposition - ALCAMPS"; U.S. Department of Energy Report IS-4902; Iowa State University: Ames, Iowa 1986.

4. Lii, K-H. Ph.D. Dissertation, Iowa State Univerisity: Ames, Iowa 1985.

5. Anglin R. J.; Kurtz, D. M., Jr. 192nd National Meeting of the American Chemical Society, Anaheim, Calif., Sep 1986; American Chemical Society: Washington, D.C.; Abstr. INOR 255.

6. Mighell, A. D.; Jacobson, R. A. Acta Crystallogr. **1963**, 16, 443.

7. Main, P.; Fiske, S. J.; Hull, S. E.; Lessinger, L.; Germain, G.; Declercq, J-P.; Woolfson, M. M. "MULTAN80 - A system of computer programs for the automatic solution of crystal structures from X-ray diffraction data"; University of York: York, England, 1980.

SUMMARY

In SECTION I, we discussed an application of X-ray powder diffraction to the lead dioxide electrode materials doped with elements such as Bi, As, and Tl. These X-ray diffraction patterns agree with the structural model that the dopants (Bi, As, or Tl) substitute Pb in the metal position of the β-PbO_2 structure. Both electrochemical and X-ray diffraction data seem to indicate that most of bismuth ions in the electrode materials are in the pentavalent state and only small fraction are in the trivalent state. The electrodeposited electrodes show strong preferred orientation along several lattice directions. At low or no Bi-concentration in the electrodes, the preferred orientation is dominantly along (121) direction. As Bi-concentration increases, the preferred orientation along (020) increases, reaching a maximum at the deposition condition of [Bi]/[Pb] = 0.7. Particle sizes also shows similar Bi-concentration dependence. These physical properties of the doped β-PbO_2 electrodes seem to be closely correlated to their electrochemical catalytic activities with regards to oxidation. Applications of other techniques such as EXAFS and neutron diffraction may complement our understanding of the structures of the material. Extensive measurements of pole figures of the electrode samples may provide detailed information about the preferred orientation.

In SECTION II, we focused our attention on the variation of crystallographic parameters due to X-ray radiation damage, as functions of the irradiation dosage. The effects of X-ray radiation damage on a single crystal of benzene chromium tricarbonly are an anisotropic lattice expansion, decrease in scale factor and secondary extinction coefficient, slight systematic variation of the positional parameters, and systematic increases in the temperature factors. Apparently, the large radiation dose caused lattice expansion and thus gradual loss of crystalline character, probably by weakening intermolecular packing forces. Results from a rigid-body thermal motion analysis of the anisotropic thermal parameters support this conclusion. Little changes in intramolecular geometry have been noticed. In order to complete this project, further studies using different radiations or at different temperature need to be done.

In SECTION III, we discussed crystal structures of several related organometallic compounds. The crystal structure determination of $[HB(pz)_3](CO)_2W[\eta^2$-$CH(SMe)]\cdot CF_3SO_3$, **1**, confirmed the presence of the η^2-thiocarbene ligand, bonded to the tungsten through both the C and S atoms. In the phosphine adducts of **1**, the phosphine adds to the carbene C preserving the same atomic connectivity as the carbene cation in the $[HB(pz)_3](CO)_2W[\eta^2$-$CH(SMe)]$ portion of the molecule. The PPh_2 group adopts an orientation minimizing a steric repulsion with the remainder

of the molecule. The reaction product of $[HB(pz)_3](CO)_2W(CS)^-$ and $Au(PR_3)^+$ (R = Ph or Me) has a structure with a W-Au bond bridged by semibridging CS and CO ligands. The much shorter Au-CO bond distance in the PMe_3 compound than in the PPh_3, strongly supports the idea that Au donates electron density into the CO π^* orbitals. The much shorter Au-C distance for Au-CS than Au-CO is consistent with the better π^* acceptor ability of CS over CO, which allows it to interact more strongly with the π-donating Au atom.

In the last section, we examined the application of the Patterson superposition method to structures with high pseudo-symmetry. The successful applications of Patterson superposition method to the structure determinations of $LiMo_8O_{10}$ and $4PPh_4 \cdot [O_2MoS_2FeS\frac{1}{2}_2 \cdot 6H_2O$ demonstrated the applicability of the method to the structures whose solutions were greatly hindered by the existence of pseudo-symmetry. It is also demonstrated that ripples in Fourier maps due to series termination errors can aid structural solutions via the Patterson superposition method. We believe the method has the potential to deal with more complex structures such as light atom structures where the constituent atoms are either C, H, or O. In order to accomplish this goal, more extensive studies of the theory of the phase problem should be done. Comparative studies of the direct method and the Patterson-related method would be helpful.

ACKNOWLEDGMENTS

It is my great pleasure to thank all those I have been greatly indebted to during my academic pursuit here in Ames. Dr. Jacobson has always been a good supervisor to me and taught me a lot in various respects. His careful reading and correction of this thesis is also greatly appreciated. Special thanks go to the former group members Jim Benson, Jim Richardson, and Suelein Wang, and to the current members Brenda, Raman, Lance, and Dave. I'd like to thank In-Hyeong Yeo and Dr. D. C. Johnson for the preparation of the PbO_2 electrode samples and for stimulating discussions, Dr. R. J. Angelici for providing the crystals of the organometallic compounds and for discussion of the structures. I thank Dr. Angelici, Dr. K. Ruedenberg, Dr. P. A. Thiel, and Dr. K-M. Ho for their service on my Ph.D. committee. This research has been funded by U.S. Department of Energy through Ames Laboratory.

The pastors and friends in the E. Free church and ICF have always encouraged me and made Ames a special place to me. Their fellowship and prayers are greatly appreciated. I thank our parents and family back home for their love and support, and especially for allowing me to come to Ames. Finally, I thank my wife, Heesook. Without her support and love, this work would have not been possible at all.